Formation of retinal direction-selective circuitry initiated by starburst amacrine cell homotypic contact

Thomas A. Ray[1,2], Suva Roy[1], Christopher Kozlowski[1,2], Jingjing Wang[1,2], Jon Cafaro[1], Samuel W. Hulbert[1], Christopher V. Wright[3], Greg D. Field[1], and Jeremy N. Kay[1,2]

1) Department of Neurobiology; 2) Department of Ophthalmology, Duke University School of Medicine, Durham, NC 27710 USA

3) Department of Cell and Developmental Biology, Vanderbilt University School of Medicine, Nashville, TN 37232 USA

Correspondence to: Jeremy Kay (jeremy.kay@duke.edu)

Keywords: Neural development; retinal ganglion cell; bipolar cell; mouse; radial migration; Ptf1a; IPL.

Impact statement: Selective synapse formation in a retinal motion-sensitive circuit is orchestrated by starburst amacrine cells, which use homotypic interactions to initiate formation of a dendritic scaffold that recruits projections from circuit partners.

SUMMARY

A common strategy by which developing neurons locate their synaptic partners is through projections to circuit-specific neuropil sublayers. Once established, sublayers serve as a substrate for selective synapse formation, but how sublayers arise during neurodevelopment remains unknown. Here we identify the earliest events that initiate formation of the direction-selective circuit in the inner plexiform layer of mouse retina. We demonstrate that radially-migrating newborn starburst amacrine cells establish homotypic contacts on arrival at the inner retina. These contacts, mediated by the cell-surface protein MEGF10, trigger neuropil innervation resulting in generation of two sublayers comprising starburst-cell dendrites. This dendritic scaffold then recruits projections from circuit partners. Abolishing MEGF10-mediated contacts profoundly delays and ultimately disrupts sublayer formation, leading to broader direction tuning and weaker direction-selectivity in retinal ganglion cells. Our findings reveal a mechanism by which differentiating neurons transition from migratory to mature morphology, and highlight this mechanism's importance in forming circuit-specific sublayers.

35 **INTRODUCTION**

36 In the developing nervous system, neurons form selective synapses to generate circuits
37 comprised of cell-type-specific connections. This selectivity is important for circuit function
38 because it ensures connectivity between neurons specialized for particular information-
39 processing tasks. Despite its importance, basic questions about selective synapse formation
40 remain unanswered. For example, we do not know how cell types fated to form synapses
41 coordinate their growth to establish contact with each other. This is a significant cell biological
42 challenge, because the neurons that comprise a single circuit are often born at disparate times and
43 physical locations.

44 In many tissues, notably the insect and vertebrate visual systems, synaptic specificity is
45 facilitated by laminar specificity, the phenomenon whereby circuit partners project their axons
46 and dendrites to narrow strata within a laminated neuropil (Sanes and Zipursky, 2010). The inner
47 plexiform layer (IPL) of the vertebrate retina comprises at least 10 distinct sublayers built from
48 the axons and dendrites of different amacrine, bipolar, and retinal ganglion cell (RGC) types
49 (Baier, 2013). By projecting to the same IPL sublayer, circuit partners can be assured of
50 encountering each other. The developmental events that create sublayers and guide circuit
51 partners to converge upon them are therefore essential for establishment of retinal circuitry. At
52 later developmental stages, when rudimentary IPL sublayers have already formed, neurons rely
53 on molecular cues localized to those sublayers for guidance to the appropriate IPL strata (Duan
54 et al., 2014; Matsuoka et al., 2011; Sun et al., 2013; Yamagata and Sanes, 2008; Visser et al.,
55 2015). However, a crucial question remains unresolved: How do sublayers form in the first
56 place? Understanding the mechanisms that initiate creation of sublayers will provide significant
57 insight into the earliest step in circuit formation.

58 To learn how members of a single circuit create layers and converge upon them to
59 achieve synapse specificity, we studied the direction-selective (DS) circuit of mouse retina (Fig.
60 1A). This circuit reports the direction of image motion to the brain through the spiking activity of
61 distinct DS ganglion cell (DSGC) types that are tuned to prefer stimuli moving in particular
62 directions (Demb, 2007; Vaney et al., 2012). The DS circuit comprises a limited number of well-
63 described cell types amenable to genetic marking and manipulation (Kay et al., 2011; Huberman
64 et al., 2009; Duan et al., 2014): 1)DSGCs; 2) GABAergic/cholinergic interneurons called
65 starburst amacrine cells (SACs); and 3) four subtypes of glutamatergic bipolar cells (Chen et al.,
66 2014; Duan et al., 2014; Greene et al., 2016; Kim et al., 2014). These DS-circuit cell types
67 project to two IPL sublayers, ON and OFF, named for the light response profiles of the neurons
68 that project to them. ON-OFF DSGCs (ooDSGCs) send dendrites to both sublayers, while SACs
69 and bipolar cells project to one or the other, depending on their subtype (Fig. 1A). Several
70 molecular perturbations have been described that influence ON vs. OFF laminar targeting in the
71 mouse DS circuit (Sun et al., 2013; Duan et al., 2014), but in these cases IPL sublayers still form
72 in the right place; errors are limited to choosing the wrong DS sublayer. Thus, neither the
73 establishment of the DS circuit sublayers nor their positioning in the appropriate IPL region
74 depends on molecules that have been studied to date.

75 Here we seek to understand the earliest events leading to formation of the DS circuit IPL
76 sublayers. Two lines of evidence suggest that SACs may take the lead in assembling this circuit.
77 First, SACs are among the first cells to stratify the IPL: Even though other neurons innervate it
78 contemporaneously, SACs are precocious in restricting their arbors into sublayers (Stacy and
79 Wong, 2003; Kay and Sanes, 2013). Second, in mutant mice that entirely lack RGCs or bipolar
80 cells, SAC IPL projections are largely normal, indicating SACs can form sublayers in the

absence of their circuit partners (Moshiri et al., 2008; Green et al., 2003). Thus, we set out to test the hypothesis that SACs orchestrate assembly of the DS circuit sublayers. We find evidence supporting this hypothesis, and we identify a surprising cellular mechanism initiating SAC lamination: Rather than immediately innervating the IPL, newborn SACs first produce a transient homotypic arbor network outside the IPL. These early homotypic contacts serve as a cue promoting SAC dendrite development and circuit integration upon conclusion of their radial migration to the inner retina. When deprived of homotypic contacts, SAC IPL innervation – and consequent sublayer formation – is impaired. We identify the SAC cell-surface protein MEGF10 as the molecular mediator of IPL innervation upon homotypic contact. In the absence of MEGF10, SACs persist in growing arbors outside the IPL, delaying IPL innervation. This in turn delays formation of the DS circuit sublayers and leads to SAC sublaminar targeting errors that persist to adulthood. We further show that impaired SAC sublayer formation has consequences for laminar targeting of their circuit partners: While partnering remains intact, lamination is disrupted, leading to spatial inhomogeneity in the DS circuit network. Finally, we show that these MEGF10-dependent anatomical changes both broaden and weaken direction tuning across the population of ooDSGCs. These results demonstrate that SACs orchestrate DS circuit assembly, first by initiating sublayer formation via homotypic contact, and then by using their laminated dendrites as a scaffold that guides projections of their circuit partners.

RESULTS

Timing of DS circuit IPL sublayer formation

To explore how the DS circuit creates its IPL sublayers, we began by determining when the sublayers first emerge in mouse. This analysis focused on SACs and ooDSGCs because

104 bipolar cells develop later (Morgan et al., 2006). Previous estimates of layer emergence vary
105 widely (Stacy and Wong, 2003; Sun et al., 2013) due to the lack of adequate markers to study
106 dendrite development in neonatal SACs. We therefore assembled a suite of mouse lines and
107 antibody markers for this purpose, enabling anatomical studies of the full SAC population as
108 well as individual cells (Fig. 1B-C; Fig. 1-Supplement 1; Fig. 2-Supplement 1). These markers
109 revealed that SAC dendrites form two continuous well-defined laminae by P1 (Fig. 1B,E). Some
110 dendrites were stratified already at P0, even though the P0 IPL neuropil is less than one cell
111 diameter wide (Fig. 1B; Fig. 1-Supplement 1). Further supporting this timeline, individual P1
112 SACs made lamina-specific projections (Fig. 1C): 96% of OFF SACs in the inner nuclear layer
113 (INL), and 99% of ON SACs in the ganglion cell layer (GCL), stratified within the expected IPL
114 sublayer (*n* = 49/51 OFF; 78/79 ON; 4 mice). By contrast, ooDSGCs projected rudimentary and
115 unstratified dendrites at P1 (*n* = 18 cells, 3 mice, none were stratified; Fig. 1E; Fig. 1-
116 Supplement 2; also see Peng et al., 2017). Even at P2, only 30% of ooDSGCs co-fasciculated
117 with SAC arbors; the rest projected diffusely within the IPL (*n* = 23 cells, 2 mice; Fig. 1D,E; Fig.
118 1-Supplement 2). These results indicate that SACs form IPL sublayers at P0-P1, and are joined
119 later by their synaptic partners.

120 **Early SAC projections target neighboring SAC somata**

121 To gain insight into how SACs form their sublayers, we next investigated the cell-cell
122 interactions that immediately precede SAC dendrite stratification. Because SACs stratify early –
123 before any other cell type investigated to date (Fig. 1; Kay and Sanes, 2013; Stacy and Wong,
124 2003) – they are unlikely to form strata by following pre-existing laminar cues. Instead, we
125 hypothesized that SACs create their sublayers by engaging in homotypic interactions. To test this
126 idea, we examined embryonic retina to determine if and when SACs establish homotypic contact.

127 SACs exit the cell cycle at the apical retinal surface and migrate radially through the outer
128 neuroblast layer (ONBL). They next arrive at the inner neuroblast layer (INBL), where
129 postmitotic neurons reside (Hinds and Hinds, 1978; Fig. 2A,B). Then they begin to innervate the
130 nascent IPL, which begins to appear in some retinal regions at E16 (Fig. 2A). To reveal SAC
131 morphology throughout these steps, the early SAC marker *Isl1* (Galli-Resta et al., 1997) was
132 used to drive Cre-dependent expression a membrane-targeted GFP (mGFP) reporter (*Isl1*^{mG}
133 mice). We also examined the orientation of SAC dendrite projections using antibodies to
134 internexin, a marker of SAC primary dendrites (Fig. 2-Supplement 1). Staining was performed at
135 E16, when SACs at all stages of their early development could be discerned (Fig. 2A-D).

136 Since mature SACs contact each other in the IPL, we expected that the onset of SAC
137 homotypic contact would occur around the time of their earliest IPL projections. Surprisingly,
138 however, this analysis revealed that SACs begin to contact each other within the INBL cell body
139 layer upon the conclusion of their radial migration. Migrating SACs rarely interacted, but on
140 arrival at the INBL, SAC arbors were observed touching the soma or primary dendrite of
141 neighboring SACs (Fig. 2A-D). The majority of INBL SACs engaged in these soma-layer
142 contacts, such that a GFP^{+} arbor network connected them (Fig. 2G). Analysis of primary dendrite
143 orientation indicated that soma-layer contacts likely arose due to projections targeted within this
144 layer: Unlike mature SACs, which exclusively project their primary dendrites towards the IPL,
145 many E16 SACs projected tangentially through the INBL – i.e., towards neighboring somata
146 (Fig. 2E,F). We even noted cases where SACs appeared to project directly towards each other
147 (Fig. 2E). These observations suggest that post-migratory SACs initiate contact with each other
148 by generating an arbor network in the INBL cell body layer.

149 Many E16 SACs also innervate the nascent IPL, raising the question of whether the
150 soma- or IPL-layer projection establishes the first homotypic contact. We concluded that soma-
151 layer SAC contact precedes IPL innervation, for three reasons. First, soma contacts were found
152 in retinal regions where the IPL had not yet emerged (Fig. 2-Supplement 2). Second, soma
153 contacts were observed among cells that still showed migratory morphological features, such as
154 apical and/or basal processes (Deans et al., 2011; Hinds and Hinds, 1978), and did not yet project
155 into the IPL (Fig. 2D; Fig. 2-Supplement 2). Third, SAC dendrite polarization in the tangential
156 plane was highly transient: By P1, the vast majority of SAC primary dendrites were oriented
157 towards the IPL (Fig. 2E,F). These three observations suggest that INBL SACs transiently seek
158 out homotypic soma contact before shifting to target the IPL.

159 We next sought to determine how long the soma-layer SAC arbor network persists. To
160 this end we examined SAC anatomy at early postnatal ages using *Isl1*^{mG} and *Chat*^{mG} (Fig. 1-
161 Supplement 1) mice. At P0-1, although SAC arbors within the soma layers no longer express
162 internexin (Fig. 2-Supplement 1), the arbor network remained remarkably prominent (Fig. 2G).
163 Most OFF SACs assumed a bi-laminar morphology, with one set of arbors in the IPL and
164 another set targeting neighboring SACs in the INL (Fig. 2H-J,L; Fig. 2-Supplements 2-3). INL
165 contacts were highly SAC-selective: 88.8% of branches terminated homotypically (n = 122 arbor
166 tips from 22 cells), significantly greater than the contact rate expected by chance (Fig. 2-
167 Supplement 3). By P2-3, however, this dense INL network was mostly gone (Fig. 2G,L; Fig. 2-
168 Supplement 2). ON SACs also made soma layer projections between P0-P3 that contacted
169 neighboring SAC somata (Fig. 2K,L; Fig. 2-Supplement 3). Together, these observations
170 demonstrate that both ON and OFF SACs make transient soma-layer homotypic contacts that

171 arise prior to IPL dendrite elaboration, and are disassembled at P2-3 after SAC sublayers have
172 formed (Fig. 2M).

173 **Homotypic contact is required for SAC IPL innervation and dendrite lamination**

174 SAC homotypic contacts arise at a time when they could serve as a cue for IPL
175 innervation and sublayer formation. To test this idea, we developed a genetic strategy to prevent
176 SACs from contacting each other in vivo. *Ptf1a* encodes a transcription factor required for
177 progenitor cells to assume an amacrine fate (Fujitani et al., 2006; Nakhai et al., 2007; Fig. 3-
178 Supplement 1). We crossed conditional *Ptf1a*^{flox} mutant mice (Krah et al., 2015) to a Cre line
179 (*Six3:Cre*; Furuta et al., 2000), that drives widespread recombination in central retina but spares
180 some progenitors from Cre activity in peripheral retina (Fig. 3A; Fig. 3-Supplement 1). In
181 *Six3:Cre; Ptf1a*$^{flox/flox}$ mice (abbreviated *Ptf1a*^{cKO}), only these spared Cre^{-} progenitors were
182 capable of giving rise to SACs, indicating that any SACs produced in these mutants are wild-
183 type at the *Ptf1a* locus (Fig. 3C). Therefore, the *Ptf1a*^{cKO} mutant creates a situation where
184 otherwise-normal SACs are present at significantly lower density than in wild-type retina (Fig.
185 3B,C). In P1-2 mutants, some SACs were effectively segregated from their neighbors – these
186 were termed "solitary" SACs – while others had neighbors sufficiently nearby that they touched
187 (Fig. 3B-F; Fig. 3-Supplement 2).

188 Comparing solitary to touching SACs in *Ptf1a*^{cKO} retinas revealed a role for homotypic
189 contacts in promoting IPL innervation and sublayer formation. At P1-2, touching SACs projected
190 normally to the IPL, similar to SACs from *Ptf1a*$^{+}$ littermates (Fig. 3D,E,G). This suggests that
191 any changes in retinal cell type composition caused by loss of *Ptf1a* (Fig. 3-Supplement 1) are
192 not by themselves sufficient to perturb SAC sublayer formation. By contrast, solitary SACs
193 largely failed to innervate the IPL (Fig. 3F,G). This was not caused by abnormal migration:

194 Solitary SACs were properly positioned at the IPL border, but sent only rudimentary arbors into
195 it (Fig. 3F; Fig. 3-Supplement 2). Solitary SACs were also more likely to project processes into
196 the soma layers (Fig. 3G), and when they did so, the projections were typically more elaborate
197 than those observed in wild-type retina (Fig. 3D,F; Fig. 3-Supplement 2). Thus, solitary SACs
198 overgrew arbors directed towards neighboring somata instead of growing IPL dendrites. Both
199 types of projection errors were also seen at P15, indicating that early errors persist to retinal
200 maturity (Fig. 3-Supplement 2). Misprojecting SACs were still closely apposed to numerous
201 other amacrine cells, and their arbors were intermingled in the IPL, strongly suggesting that
202 generic amacrine interactions are not sufficient to ensure normal dendrite targeting (Fig. 3-
203 Supplement 2). Instead, homotypic interactions are specifically required for IPL innervation and
204 sublayer formation.

205 **Requirement for MEGF10 in SAC IPL innervation and sublayer formation**

206 To understand how SACs initiate IPL innervation upon homotypic contact, we next
207 sought to identify the molecular cues that SACs use to recognize that contact has occurred. The
208 cell-surface protein MEGF10 (Fig. 4A) is a strong candidate to mediate homotypic recognition in
209 this context, for four reasons. First, it is selectively expressed by SACs during the perinatal
210 period (Fig. 1B; Fig. 1-Supplement 1). Second, the onset of its expression coincides with onset
211 of SAC homotypic contact at the conclusion of radial migration (Fig. 4B). Third, MEGF10
212 protein is present on soma-layer SAC arbors, making it available to transduce signals arising on
213 these arbors (Fig. 4C). Finally, MEGF10 mediates SAC-SAC interactions in a separate context –
214 during formation of the orderly "mosaic" among SAC cell bodies across the retina (Kay et al.,
215 2012). Thus, we tested whether MEGF10 also mediates SAC-SAC recognition to initiate IPL
216 innervation. If so, SACs from mice lacking *Megf10* gene function should have phenotypes

217 similar to solitary *Ptf1a*^{cKO} SACs – i.e., reduced IPL innervation and increased arborization in
218 cell body layers.

219 To test this prediction, we examined SAC anatomy in *Megf10* null mutants (Kay et al.,
220 2012) and littermate controls at P0-1, when sublayers are first forming. We found a striking
221 effect on sublayer formation: Both ON and OFF strata were absent or severely disrupted in
222 mutants (Fig. 5A). The cause of sublayer absence was investigated using pan-SAC labeling (Fig.
223 5A,B) and single-cell analysis (Fig. 5C; Fig. 6D). These studies revealed a severe deficit in IPL
224 dendrite arborization: Most *Megf10*$^{-/-}$ SACs made only rudimentary, unstratified IPL projections
225 at P0-1 (n = 1/15 OFF SACs were stratified). Other amacrine cell types showed normal dendritic
226 morphology in *Megf10* mutants (Fig. 5-Supplement 1), indicating that the phenotype was
227 specific to SACs. Loss of IPL innervation was not due to aberrant SAC radial migration, because,
228 at P0, mutant SACs had reached the inner retina in normal numbers (wild-type, 2600 ± 287
229 SACs/mm^2; mutant, 3153 ± 145 SACs/mm^2; p = 0.144, 2-tailed t-test; n = 3 each group), and
230 were positioned adjacent to the IPL, similar to littermate controls (Fig. 5A). Furthermore, most
231 mutant SACs sent at least some arbors into the IPL at P0-1 (Fig 5A,C; Fig. 6D), suggesting that
232 they migrated to a location from which IPL innervation was feasible. However, the mutant SAC
233 arbors that reached the IPL appeared undifferentiated, with a lack of space-filling branches (Fig.
234 5A,C). As a result, not only did their arbors enclose a significantly smaller IPL territory, but they
235 also failed to sample as much of their enclosed territory as control SACs (Fig. 5C; also compare
236 to control cell in Fig. 2H). By P3 some ON SAC IPL innervation was evident, but OFF SAC
237 arbors remained largely confined to the soma layer; those that did reach the IPL remained
238 undifferentiated (Fig. 5B; Fig. 6A,D). These observations indicate that deletion of MEGF10
239 causes an IPL innervation phenotype strongly reminiscent of *Ptf1a*^{cKO} solitary SACs: Both

240 manipulations profoundly impair SAC dendrite arborization within the IPL, preventing timely
241 sublayer formation.

242 In contrast to their underinnervation of the IPL, *Megf10* mutant SACs arborized
243 exuberantly in the soma layers (Fig. 6A). Both ON and OFF SACs were affected (Fig. 6D,E; Fig.
244 6-Supplement 1), but the OFF SAC phenotype was particularly striking: Starting at P1, the
245 mutant INL network became much more elaborate than the control network of any age (Fig.
246 6A,C). INL arbor density increased in mutants from P0 to P1 and remained high at P3; by
247 contrast, control SACs largely eliminated their INL projections over the same period (Fig 5A,B;
248 Fig. 6A,E). To understand how mutant SACs generate a denser and more persistent soma-layer
249 network, we assessed single SAC morphology (Fig. 6A,D). From this analysis we determined
250 that one reason for the denser mutant network, particularly at P2-3, was that a larger number of
251 mutant cells projected to the soma layers (Fig. 6E). However, this reason was not sufficient to
252 explain the denser mutant INL network at P1 (Fig. 6C), because at that age the number of cells
253 projecting to the INL was similar in mutants and littermate controls (Fig. 6E). Therefore, to
254 account for this increase in INL arbor density, we surmised that individual mutant SAC must, on
255 average, overinnervate INL. Supporting this conclusion, we found that mutant SACs frequently
256 had more extensive INL arbors than littermate control SACs (Fig. 6B). Further, mutant SACs
257 continued to grow primary dendrites tangentially within soma layers at P1, when the vast
258 majority of control SACs only targeted the IPL (Fig. 6F; also see Fig. 2F). These observations
259 indicate that mutant SACs continue to expand their soma layer arbor network at P1. Thus, as
260 with solitary *Ptf1a*^{cKO} SACs, soma layer projections were both more frequent and more
261 exuberant for *Megf10*$^{-/-}$ SACs.

262 Together, these data suggest that MEGF10 governs a developmental transition from
263 soma-layer to IPL-layer dendrite growth (Fig. 6G): Whereas control SACs have only a brief
264 period of soma-layer growth, switching to IPL ramification around P0, *Megf10* mutant SACs do
265 not make this transition and instead persist in soma-layer innervation. As a result of this failed
266 transition, many individual mutant SACs ramify extensively in the INL but underinnervate the
267 IPL, causing the dendrite targeting phenotypes that were observed at the population level (Fig
268 6A-C). We conclude that, because MEGF10 regulates IPL innervation in this way, MEGF10 is
269 required for initial formation of SAC IPL sublayers.

270 **SAC dendrite targeting requires transcellular MEGF10 signaling**

271 Given the similar phenotypes of *Megf10* mutant and solitary *Ptf1a*^{cKO} SACs, we
272 hypothesized that MEGF10 is the molecular cue that triggers IPL innervation upon SAC-SAC
273 contact. A key prediction of this model is that SACs should require MEGF10 signals from their
274 neighbors to target their dendrites properly. To test this prediction, we generated a conditional
275 *Megf10*^{flox} allele and used it to create a situation where *Megf10*$^{+}$ SACs were surrounded by
276 *Megf10*$^{-}$ mutant cells. This was accomplished via the same *Six3:Cre* strategy that we employed
277 in our *Ptf1a*^{cKO} studies (Fig. 3A-C). In central retina of *Six3:Cre; Megf10*$^{flox/lacZ}$ (*Six3-Megf10*^{cKO})
278 animals, the vast majority of cells expressed a Cre-dependent GFP reporter, indicating that they
279 lacked *Megf10* function (Fig. 6A). Accordingly, SACs projected exuberantly to the INL and
280 sublayer formation was disrupted, as in null mutants (Fig. 7B; Fig. 7-Supplement 1).

281 In peripheral retina, some SACs escaped Cre activity, leading to absence of the GFP
282 reporter and continued MEGF10 protein expression (Fig. 7A,B; Fig. 7-Supplement 1). Our
283 model predicts that these cells should have mutant dendrite phenotypes despite retaining
284 MEGF10. To test this prediction, we imaged βgal-stained OFF SACs from *Six3-Megf10*^{cKO} and

285 littermate control mice at P2. This age was chosen because wild-type and null mutant mice
286 showed a large difference in SAC INL projection frequency (Fig. 6E). In littermate controls, we
287 found that βgal^{+} SACs rarely projected to the INL (Fig. 7C,D); therefore, they behaved like
288 control SACs from earlier experiments (Fig. 6E). By contrast, *Megf10*$^{+}$ SACs surrounded by
289 mutant SACs in *Six3-Megf10*^{cKO} retina showed a high rate of INL projections, nearly identical to
290 their *Megf10*$^{-}$ neighbors (Fig. 7B,D; Fig. 7-Supplement 1). Thus, when *Megf10*$^{+}$ SACs are
291 deprived of MEGF10 signal from adjacent SACs, they make exuberant soma-layer projections.
292 This finding implicates MEGF10 as a transcellular signal that controls SAC dendrite targeting
293 (Fig. 7K).

294 Next we investigated how SACs receive this MEGF10 signal from their neighbors. Given
295 that MEGF10 can function as a receptor in other contexts (Chung et al., 2013; Kay et al., 2012),
296 we speculated that MEGF10 might act as its own receptor. In support of this idea, co-
297 immunoprecipitation experiments using intracellularly truncated *Megf10* constructs showed that
298 MEGF10 can interact with itself through its extracellular domain (Fig. 7I,J; Fig. 7-Supplement 2).
299 Thus, MEGF10 appears biochemically capable of acting as both ligand and receptor.

300 If MEGF10 is indeed a receptor in this context, SACs should require it to detect contact
301 with MEGF10-expressing homotypic neighbors. To test this prediction, we asked whether
302 removal of *Megf10* from a single SAC, during the period of soma-layer homotypic contact,
303 would impair its IPL innervation despite normal MEGF10 expression by surrounding cells. We
304 used *Chat*^{Cre} to achieve sparse recombination in SACs of neonatal mice, as in the anatomy
305 experiments described above (Fig. 2H-K; Fig. 6D). In *Chat-Megf10*^{cKO} animals, MEGF10
306 immunostaining was used to identify SACs that lost MEGF10 protein prior to P3 – i.e., during
307 the period when soma-layer arbors are present (Fig. 7F,G). MEGF10^{-} cells constituted a small

308 minority of SACs at P3, meaning that they were generally surrounded by MEGF10^{+} neighbors
309 (Fig. 7-Supplement 1). In this context, MEGF10^{-} SACs produced more exuberant soma-layer
310 arbors than neighboring MEGF10^{+} cells, while sending only minimal arbors into the IPL (Fig.
311 7E-H). Thus, single MEGF10^{-} SACs had phenotypes similar to SACs from mice entirely lacking
312 *Megf10* (Fig. 7G,H; compare to Fig. 6D). By contrast, adjacent MEGF10^{+} cells in the same
313 *Chat-Megf10^{cKO}* retinas were indistinguishable from littermate control SACs (Fig. 7E,F,H).
314 Therefore, when *Megf10* is lost during dendro-somatic contact (but not after; see below), SACs
315 make projection errors typical of neurons deprived of homotypic interactions, and they do so
316 even if their neighbors express MEGF10 and are developing normally. Together, these
317 experiments support the conclusion that MEGF10 is a receptor through which SACs detect each
318 other to terminate soma-layer growth and initiate IPL innervation (Fig. 7K).

319 **SAC errors persist to adulthood in *Megf10* mutants**

320 We next asked whether neonatal MEGF10-mediated interactions influence the anatomy
321 of SAC IPL sublayers at maturity. We found that SAC sublayers eventually formed (by P5; Fig.
322 8H), and were present in the mature *Megf10$^{-/-}$* retina, but they were marred by numerous errors.
323 Sporadically, and at apparently arbitrary retinal locations, two kinds of local laminar disruptions
324 were apparent. First, there were discontinuities in the ON and OFF strata, such that mutant SACs
325 did not completely innervate their sublaminae (Fig. 8A-C). These discontinuities diminished
326 retinal coverage within each mutant sublayer by ~15% (OFF decrease, 15.0 ± 0.9%; ON decrease,
327 13.7 ± 4.0%; mean ± SD; n = 9 fields of view/2 mice per genotype). Innervation gaps were not
328 observed for other amacrine cells, indicating that SACs were selectively affected (Fig. 8-
329 Supplement 1). Examination of single SACs revealed that while dendritic patterning
330 substantially recovered between P1 and adulthood, SAC arbor territories remained significantly

331 smaller in mutants (Fig. 8D). These phenotypes suggest that mutant SACs never fully made up
332 for their initial IPL innervation deficit, thereby contributing to gaps in the dendritic plexus.

333 The second type of SAC error in mature *Megf10*$^{-/-}$ IPL was dendrite mistargeting to
334 ectopic IPL strata (Fig. 8A,B,E). Both ON and OFF SACs were affected; in each case ectopic
335 arbors were mostly found in IPL regions inappropriately close to the soma layers (Fig. 8A,B).
336 *En-face* images of mutant IPL revealed that ectopic OFF arbors formed a patchy but extensive
337 fascicle network connecting many of the cells (Fig. 8E,F; 78.5 ± 3.5% of SACs participated in
338 the network, mean ± 95% CI). This IPL network was morphologically similar to the ectopic INL
339 network observed in mutants at earlier ages (Fig. 6C), raising the possibility that the early
340 network gives rise to the adult network by shifting location from the INL to the IPL. Supporting
341 this view, we found that a soma layer-to-IPL transition occurs at P5, when mutant SACs began
342 projecting to ectopic IPL locations in addition to the soma layers (Fig. 8G,H; Fig. 8-Supplement
343 1). This transition occurred without a significant change in the number of mutant SACs
344 projecting into the ectopic network (Fig. 8F; Fig. 8-Supplement 1), suggesting that the same cells
345 continued to participate in the network but simply altered their anatomy to target the IPL. Thus,
346 early exuberant soma-layer projections appear to give rise to adult IPL ectopias, starting between
347 P3 and P5.

348 Together, these two adult mutant phenotypes demonstrate that DS circuit sublayer
349 formation is delayed and imperfect in the absence of MEGF10. While other mechanisms appear
350 to partially compensate for MEGF10 in generating the sublayers, such mechanisms are not
351 sufficient to prevent persistence of innervation gaps and laminar targeting errors. Thus, MEGF10
352 is essential for normal formation of the mature SAC IPL projection.

353 Next we sought to directly test the idea that MEGF10 is required early – at the time of
354 initial SAC homotypic contact – to ensure normal SAC IPL lamination at maturity. To this end,
355 we used *Megf10*^{flox} mice to delete MEGF10 at different times. Deletion prior to the onset of
356 homotypic contact, using the *Six3:Cre* line, fully phenocopied *Megf10*$^{-/-}$ adult IPL errors (Fig.
357 8A), suggesting a requirement for MEGF10 at the time of contact. To remove MEGF10 from
358 SACs that had already established homotypic contact, we used *Chat*^{Cre}. In this line, the number
359 of SACs expressing Cre gradually increases over the first postnatal days to encompass the full
360 SAC population (Xu et al., 2016). Therefore, *Chat-Megf10*^{cKO} mice can be used both for early,
361 sparse MEGF10 deletion (Fig. 7F-H) and for later, broad MEGF10 deletion. MEGF10
362 immunostaining revealed that this late, broad deletion occurs between P3 and P5 (Fig. 7-
363 Supplement 1), such that MEGF10 expression is largely preserved during the period when
364 homotypic soma-layer contacts exist (Fig. 2L), but is eliminated shortly thereafter. In this
365 *Chat*^{Cre}-mediated deletion regime, SAC laminar targeting and gap errors were exceedingly rare
366 (Fig. 9A). These experiments therefore define a time window for MEGF10 function (Fig. 9C):
367 Adult IPL targeting phenotypes require absence of MEGF10 during the soma-layer projection
368 phase of SAC development – i.e. prior to P3. Any additional activity of MEGF10 after P3 is
369 dispensable for the adult IPL phenotype. These findings strongly support a model whereby the
370 functions of MEGF10 during early homotypic contact – i.e. promoting IPL innervation and
371 terminating soma-layer arbor growth – are necessary for development of normal SAC IPL
372 innervation at maturity.

373 **Mosaic spacing errors do not account for SAC IPL phenotype in *Megf10* mutants**

374 In addition to laminar targeting errors, *Megf10* mutants also show disruptions in the
375 mosaic spacing of SAC cell bodies across the retina: Instead of a regular, uniform distribution,

376 mutant SAC positioning is random (Kay et al., 2012). We considered the possibility that SAC
377 IPL errors might arise due to MEGF10 effects on soma spacing. Two lines of evidence suggest
378 that this is not the case. First, the two phenotypes were not well correlated at the individual SAC
379 level: Regardless of the severity of their mosaic spacing defects, SACs made IPL targeting errors
380 at a constant rate (Fig. 9-Supplement 1). This finding suggests that disturbed cell positioning
381 does not influence the probability of making an IPL error. Second, using our *Megf10*^{flox} allele, we
382 were able to dissociate the IPL and mosaic phenotypes: Deletion of MEGF10 after P3 in *Chat-*
383 *Megf10*^{cKO} mice caused mosaic patterning deficits, but IPL projections were largely normal (Fig.
384 9A,B). This finding demonstrates that IPL laminar perturbations are not an inevitable
385 consequence of altered soma positioning. Altogether, these experiments support the notion that
386 altered SAC position makes at best a minor contribution to IPL phenotypes; instead, delayed IPL
387 innervation and exuberant soma-layer arborization are likely the major sources of perturbed SAC
388 projections at maturity.

389 **SAC IPL errors induce laminar targeting errors by their DS circuit partners**

390 Next we asked whether MEGF10, and its effects on SAC sublayer formation, are
391 important for assembly of the broader DS circuit. To this end we tested the impact of SAC IPL
392 stratification errors on laminar targeting by their circuit partners. First, we examined ooDSGC
393 IPL projections using the *Hb9:GFP* (Fig. 10) and *Drd4:GFP* (Fig. 10-Supplement 1) transgenic
394 lines, which label ooDSGC subtypes with different preferred directions (Trenholm et al., 2011;
395 Huberman et al., 2009). In littermate control mice (n = 9), ooDSGC dendrites were tightly and
396 selectively associated with SAC arbors, as shown previously (Vaney and Pow, 2000). This
397 association was maintained in *Megf10* mutants: Both normal and ectopic SAC IPL arbors
398 reliably recruited ectopic ooDSGC projections (Fig. 10A-C; Fig. 10-Supplement 1; n = 240

399 ectopias from 5 mutants, >97% contained ooDSGC arbors). Further, when SAC gaps were
400 present in the mutant IPL, ooDSGC dendrites typically grew around the gap edges and failed to
401 enter them (Fig. 10D; Fig. 10-Supplement 1; n = 325 gaps from 5 mutants, >95% devoid of
402 ooDSGC arbors). Thus, SACs provide both permissive cues required for ooDSGC IPL
403 innervation, and also attractive cues sufficient to recruit ooDSGCs to the wrong IPL sublayer.

404 Next we determined the impact of altered SAC lamination on the axons of bipolar cells
405 that participate in the DS circuit (Fig. 11A). We examined the four cell types (BC2, BC3a, BC5,
406 and BC7) that make extensive monosynaptic connections with SACs and ooDSGCs (Duan et al.,
407 2014; Ding et al., 2016; Greene et al., 2016; Kim et al., 2014; Chen et al., 2014). Bipolar axons
408 were marked with type-specific antibodies and mouse lines reported previously (Wässle et al.,
409 2009; Duan et al., 2014), as well as a novel transgenic marker of BC5 (*Gjd2:GFP*; Fig. 11-
410 Supplement 1). In wild-type retina, DS-circuit bipolar cells arborized in close contact with SAC
411 dendrites; however, unlike ooDSGCs, they remained adjacent to SACs rather than overlapping
412 them (Fig. 11A-D; Fig. 11-Supplement 1). This arrangement was preserved in *Megf10* mutants:
413 Axons of all four bipolar cell types were recruited to ectopic IPL locations by mistargeted SAC
414 arbors, where they stratified adjacent to SACs (Fig. 11B-D,F; Fig. 11-Supplement 1). For
415 example, BC5 and BC7 terminals always sandwiched SAC arbors, regardless of their IPL
416 location – even when doing so required formation of a supernumerary BC axon field between the
417 normal and ectopic SAC sublayers (Fig. 11C,D). To quantify the mistargeting effect we
418 measured the position of BC5 and BC7 terminals adjacent to ON SAC ectopias. Their arbors
419 were pushed farther apart by SAC arbor clumps (Fig. 11C-E), which shifted BC7 terminals
420 significantly towards the GCL by ~4 μm (69 ± 0.8% of IPL depth in control regions to 74 ±
421 1.9% in affected regions; mean ± S.E.M.; n = 21 control, 6 affected; 2-tailed t-test, p = 0.0024).

422 These observations indicate that DS-circuit bipolar cells, like ooDSGCs, respond to SAC
423 attractive cues. However, in contrast to ooDSGCs, bipolar cell projections were minimally
424 affected by SAC IPL gaps. While BC5 and BC7 terminals were slightly mispositioned in the
425 absence of SAC arbors – they were closer together – innervation of gap regions was otherwise
426 normal (Fig. 11C-F). Thus, DS-circuit bipolar axons either do not require SAC-derived signals
427 for IPL innervation, or the relevant signals are capable of acting over larger distances than the
428 typical SAC IPL gap size (35-45 µm maximum diameter). Altogether, these analyses of DS
429 circuit anatomy in *Megf10* mutants support the notion that early-stratifying SACs form a scaffold
430 that directs IPL laminar targeting of their circuit partners using multiple guidance strategies.

431 **Early SAC homotypic interactions impact DS circuit function**

432 Finally, we investigated the extent to which developmental events controlled by MEGF10
433 affect DS circuit function. We sought to determine whether the anatomical perturbations caused
434 by loss of MEGF10 – SAC laminar targeting and mosaic spacing errors – alter direction coding
435 by ooDSGCs. To do this we recorded from wild-type and *Megf10*$^{-/-}$ retinas on a large-scale
436 multielectrode array (Field et al., 2007; Yu et al., 2017). ooDSGCs were identified based on their
437 responses to drifting gratings and moving bars (see Methods), which unambiguously
438 distinguished them from other recorded RGCs (Fig. 12A). Because MEGF10 is not expressed in
439 the adult DS circuit (Kay et al., 2012), we could be confident that any mutant physiological
440 phenotypes reflect anatomical changes that arose during development.

441 These experiments revealed that ooDSGCs with robust direction selectivity were present
442 in both wild-type and *Megf10*$^{-/-}$ retinas (Fig. 12A,B), and constituted a similar fraction of the
443 RGC population in both strains (wild-type: 80/609, 13.1%; mutant: 74/551, 13.4%).
444 Furthermore, loss of *Megf10* did not alter the organization of ooDSGC preferred directions along

445 cardinal axes (Oyster and Barlow, 1967), or the fraction of ooDSGCs preferring each direction
446 (Fig. 12-Supplement 1). These results are consistent with the observation that mutant SACs
447 remain paired with ooDSGC dendrites and bipolar cell axons even when normal lamination and
448 arbor spacing are disrupted. They indicate that the qualitative functional properties of the circuit
449 are still present.

450 However, a more careful examination of DS tuning properties in *Megf10*$^{-/-}$ retinas
451 revealed clear quantitative differences in ooDSGC responses. Moving bars were used to measure
452 the width and strength of direction tuning for each identified ooDSGC across the populations
453 recorded on the electrode array (Fig. 12C). Tuning width was measured as the circular standard
454 deviation of the tuning curve, while tuning strength was measured as the normalized response
455 difference to motion in the preferred and null directions (see Methods). These experiments
456 revealed systematic shifts toward broader (Fig. 12D) and weaker (Fig. 12E) direction tuning
457 across the population of ooDSGCs in *Megf10* mutant retinas. This was mainly due to higher null
458 direction spiking among ooDSGCs in mutants (Fig. 12B,C,E). Furthermore, these effects on
459 tuning width and strength persisted across a broad range of stimulus contrasts (Fig. 12-
460 Supplement 1). These results demonstrate that disruption of MEGF10-dependent developmental
461 patterning degrades the precision and strength of ooDSGC direction tuning. They further suggest
462 that perturbations to the anatomical regularly of the circuit across space (e.g. laminar uniformity
463 and SAC spacing) may effectively introduce noise in the DS circuit that broadens and weakens
464 direction tuning (see Discussion).

465 This idea led us to consider additional functional properties of ooDSGCs that might
466 depend on the spatial regularity of the DS circuit, and therefore might be perturbed in *Megf10*
467 mutants. One such property is the generation of symmetric DS responses to stimuli that are

468 darker or brighter than the background (Fig. 12F,G). This ON-OFF symmetry allows the DS
469 response to be largely insensitive to contrast reversals (Amthor and Grzywacz, 1993); it arises
470 because ooDSGCs receive highly symmetric SAC inputs in both ON and OFF sublayers (Fig.
471 1A). In *Megf10* mutants, ON-OFF anatomical symmetry is disturbed, because ON and OFF SAC
472 errors are not spatially correlated (Fig. 8A-C). We hypothesized that this might lead to disparities
473 in the direction tuning of individual cells' ON and OFF responses. Indeed, *Megf10*$^{-/-}$ ooDSGCs
474 exhibited greater separation (i.e. less coherence) between their ON and OFF preferred directions
475 than wild-type ooDSGCs, across a broad range of contrasts (Fig. 12H; Fig. 12-Supplement 1).
476 These results support the idea that MEGF10 serves to establish a highly uniform and regular
477 network of SAC dendrites (via controlling both the precise timing of INL lamination and through
478 regularizing inter-SAC spacing), the net effect of which is to allow greater precision and
479 coherence in the direction tuning of ooDSGCs.

480 **DISCUSSION**

481 Neural circuits typically consist of multiple cell types born at different places and times,
482 raising the question of how circuit partners manage to converge at a common site for selective
483 synapse formation. Here we describe a developmental strategy that the retinal DS circuit uses to
484 solve this problem. We show that SACs coordinate amongst themselves to assemble a dendritic
485 scaffold that subsequently recruits projections from their DS circuit partners. By identifying for
486 the first time a genetic manipulation – loss of *Megf10* – that causes SACs to misproject outside
487 their two typical IPL layers, we uncover mechanisms by which SACs assemble this dendritic
488 scaffold. Further, we use *Megf10* mutants to examine the effects on DS circuit anatomy and
489 function when the SAC scaffold is disrupted. We find that MEGF10 establishes DS circuit
490 spatial homogeneity across the retina, both by controlling IPL innervation patterns and by
491 positioning SAC cell bodies. In *Megf10* mutants, disruptions in circuit homogeneity occur with
492 minimal effects on radial SAC dendrite anatomy or synaptic partnering, making the phenotype
493 unique among DS circuit developmental mutants. Finally, we find that this abnormal spatial
494 pattern degrades DS circuit function by broadening the range of directions to which ooDSGCs
495 will respond, and by weakening overall direction selectivity. These results provide new insight
496 into general strategies for circuit development, as well as the specific mechanisms that ensure
497 functional assembly of the DS circuit.

498 **Homotypic recognition as a mechanism regulating dendrite differentiation**

499 During radial migration, newborn central nervous system neurons have a multipolar
500 morphology, but on arrival at their final position within the tissue they become highly polarized
501 (Nadarajah et al., 2001; Tabata and Nakajima, 2003; Cooper, 2014; Chow et al., 2015; Krol et al.,
502 2016; Hinds and Hinds, 1978). This morphological change enables elaboration of dendrites and

503 integration into local circuitry. If dendrite differentiation begins early, migration is impaired
504 (Hoshiba et al., 2016), suggesting that the transition from migratory to mature morphology must
505 be highly regulated to ensure that neurons only differentiate once they arrive at their final
506 position. The extracellular cues that signal arrival are poorly understood in most nervous system
507 regions.

508 Here we show that SACs use homotypic recognition, mediated by MEGF10, to initiate
509 IPL-directed dendrite morphogenesis. When deprived of homotypic neighbors or MEGF10,
510 SACs at the IPL retain a multipolar morphology (compare Fig. 2C to Figs. 3F, 6A) instead of
511 polarizing arbors towards the IPL. This indicates that the transition from migratory to mature
512 morphology is impaired in the absence of SAC homotypic recognition. We show that migrating
513 SACs first establish homotypic contact upon arrival at the inner retina. At this stage they are still
514 multipolar (Fig. 2D), but they orient primary dendrites tangentially within the INBL to ultimately
515 contact their SAC neighbors. These contacts occur prior to IPL innervation, and are required for
516 it to occur in a timely manner. SACs lacking neighbors or the molecular means to detect them
517 (i.e., MEGF10) appear to persist in this multipolar soma-layer-targeting phase, causing over-
518 innervation of the INL/GCL and delaying IPL innervation (Fig. 6G). Thus, establishment of
519 homotypic contact is a key checkpoint for the progression of SAC dendrite differentiation and
520 IPL sublayer morphogenesis.

521 We propose that the function of this checkpoint is to ensure that SACs elaborate dendrites
522 only when they have arrived adjacent to the IPL. The presence of other SACs that have already
523 completed their migration is a reliable indicator of arrival in the proper location. Because soma-
524 layer SAC contacts appear earliest, and because MEGF10 selectively influences IPL innervation
525 during the period when they exist, we favor the notion that the key homotypic interactions occur

526 through these arbors. However, we cannot exclude that IPL-based interactions also play a role.
527 INL-directed arbors resembling those we describe can be discerned in many developing
528 zebrafish amacrine cells (Godinho et al., 2005; Chow et al., 2015), raising the possibility that this
529 mechanism applies across species and across other amacrine cell types. Because most neurons
530 require a way to control when and where they differentiate, we anticipate that this homotypic
531 contact strategy, or variations upon it, may have important roles in the differentiation of other
532 CNS neurons at the completion of their radial migration.

533 **MEGF10 as the signal mediating SAC homotypic recognition**

534 We conclude that MEGF10 is the molecule responsible for homotypic recognition during
535 SAC IPL innervation. Four key results support this conclusion. First, MEGF10 is expressed at
536 the right time and place to assume this role: It is expressed selectively in SACs (Fig. 1), upon
537 conclusion of their radial migration, and in the soma-layer arbors that we propose mediate
538 recognition (Fig. 4). Second, *Megf10* null mutant SACs phenocopy the dendrite polarization
539 errors seen in solitary *Ptf1a*^{cKO} SACs, suggesting that homotypic recognition requires *Megf10*.
540 Third, co-immunoprecipitation experiments indicate that MEGF10 interacts with itself via its
541 extracellular domain, suggesting it could act as both ligand and receptor. While this biochemical
542 interaction may take place in the *cis* configuration, the fourth line of evidence indicates that
543 MEGF10 interacts in *trans* as well: Using a conditional-null *Megf10* allele in vivo, we show that
544 MEGF10 is required on the cell that sends homotypic signals as well as the cell receiving those
545 signals. Loss of MEGF10 on either side leads to dendritic phenotypes resembling solitary SACs
546 and *Megf10* null mutants. Together, these data are consistent with a model whereby SAC-SAC
547 contact initiates a transcellular MEGF10 homophilic interaction, in which MEGF10 serves as

548 both receptor and ligand to trigger the switch from migratory to mature morphology (see model,
549 Fig. 7K).

550 This homophilic model of MEGF10 function is consistent with its role during
551 establishment of mosaic cell body patterning (Kay et al. 2012). In that context, MEGF10 acts as
552 ligand and receptor to mediate cell-cell repulsion, thereby spacing SAC somata evenly across the
553 retina. Here we discover a second MEGF10 function in SAC IPL innervation. Because the two
554 SAC phenotypes have different underlying cell biology (soma movement vs. dendrite dynamics),
555 and separable temporal requirements for MEGF10 function (Fig. 9), it seems unlikely that they
556 reflect disruption of a single biological event. Instead, MEGF10 appears to act at distinct, albeit
557 partially overlapping times, to control different aspects of SAC development, each of which are
558 regulated by contact with homotypic neighbors (see model, Fig. 9C).

559 **Formation of SAC IPL sublayers**

560 Our results shed light on the mechanisms controlling SAC dendrite lamination. While
561 repulsion mediated by Sema6a and PlexinA2 prevents OFF SACs from straying to the ON
562 sublayer (Sun et al., 2013), molecules required for formation of the SAC sublayers have not been
563 identified. We show that SACs deprived of homotypic neighbors or MEGF10 initially fail to
564 form IPL sublayers, and when they eventually do so, their strata are riddled with errors. Both the
565 lack of sublayers at early stages and the dendritic mistargeting to inappropriate sublayers at
566 maturity are novel SAC phenotypes; they implicate MEGF10 as a key player in forming SAC
567 IPL sublayer-specific projections.

568 It is generally assumed that sublayer formation has two basic molecular requirements: 1)
569 Attractive/adhesive molecules that mediate co-fasciculation of stratified arbors; and 2) repulsive
570 cues that prevent straying of arbors into other sublayers (Lefebvre et al., 2015; Sanes and

571 Yamagata, 2009). Our MEGF10 studies suggest an additional, earlier requirement for cell-cell
572 interactions that occur prior to neuropil innervation. The purpose of this surprisingly early SAC-
573 SAC interaction, we propose, is to ensure that SACs grow dendrites at the right time and place to
574 co-fasciculate with their SAC neighbors. The molecular basis of this homotypic co-fasciculation
575 – clearly another essential player in sublayer formation – remains to be determined. MEGF10 is
576 probably not involved; the co-fasciculation system appears intact in *Megf10* mutants given that
577 sublayers do eventually form. Perhaps this system is part of the mechanism that compensates for
578 loss of MEGF10 to ultimately generate the sublayers.

579 When IPL arborization is delayed by loss of *Megf10*, two SAC errors ensue. First, SACs
580 generate mistargeted dendritic material that appears to persist as ectopic IPL sublayers. Second,
581 SACs never completely innervate their sublayers, resulting in fragmented IPL strata. These two
582 errors are caused by delays rather than an ongoing requirement for MEGF10 during later stages
583 of arbor growth, as shown by conditional mutant experiments (Fig. 9). Thus, our findings support
584 the idea that timing is critical to the sequential lamination of the IPL: When SAC dendrites arrive
585 in the IPL too late, they encounter a different cellular and molecular milieu that may not support
586 the proper development of their arbors. In this view, the normal role of MEGF10 in DS circuit
587 assembly is to instigate SAC dendrite outgrowth at the crucial time when laminar self-assembly
588 can occur.

589 SACs may face an additional obstacle to overcoming their delayed IPL innervation in
590 *Megf10* mutants: abnormal soma positioning. While mosaic spacing errors do not account for the
591 *Megf10* mutant ectopic IPL phenotype, we cannot exclude the possibility that the placement of
592 IPL arbor gaps might be at least partly explained by soma position. If SACs are struggling to
593 make up for their delayed IPL innervation, it is plausible that increasing the distance between

594 SACs (as happens sporadically due to random positioning) might further hinder the development
595 of complete retinal coverage.

596 **SACs as a scaffold for DS circuit assembly**

597 Because of their early stratification, SAC dendrites have been proposed to act as a
598 scaffold that guides assembly of the DS circuit (Stacy and Wong, 2003). A key prediction of this
599 model is that laminar targeting of later-stratifying cell types should depend on the existence of
600 this scaffold. We show using a SAC-specific manipulation – removal of *Megf10* – that disruption
601 of SAC stratification causes their bipolar and ooDSGC circuit partners to make corresponding
602 projection errors. Based on the kinds of errors we observed, SACs appear to provide attractive,
603 permissive, and possibly even repulsive arbor sorting cues to influence the laminar positioning of
604 their circuit partners. This work thus constitutes the first critical test of the scaffolding model,
605 and provides strong support for it. We find that SACs use homotypic interactions to initiate
606 formation of their circuit sublayers, and then heterotypic interactions to recruit circuit partners to
607 join them. SACs might achieve their scaffolding functions directly, by providing guidance cues
608 to their partners; or they may do so indirectly, by patterning the IPL projections of an
609 intermediary cell type that in turn guides later-arriving projections. Direct scaffolding may be
610 mediated in part by Cadherins 8 and 9, which regulate interactions between SAC dendrites and
611 DS circuit bipolar cell axons (Duan et al., 2014). Molecular mediators of ooDSGC-SAC dendrite
612 interactions remain to be identified.

613 Evidence that the SAC scaffold can be repulsive – or at least can exclude bipolar arbors
614 from certain IPL regions – came from our observations of BC axon anatomy. In wild-type retina,
615 we were surprised to note how completely the BC3a, BC5, and BC7 axon terminals were
616 excluded from the SAC territory – they contacted it but did not enter (Fig. 11B-D; Fig. 11-

617 Supplement 1). This behavior stands in stark contrast to the behavior of ooDSGC dendrites,
618 which completely overlapped SACs (Fig. 10A-B; Vaney and Pow, 2000). Moreover, in *Megf10*
619 mutants, the laminar distance between BC5 and BC7 terminals was reduced in the absence of
620 SAC arbors, and increased in the presence of SAC ectopias, further suggesting the existence of
621 local SAC-BC repulsion. The finding that SACs exclude bipolar circuit partners from their
622 sublayers appears at first counterintuitive. But given that no bipolar cell type is exclusively
623 devoted to the DS circuit (Wässle et al., 2009; Greene et al., 2016; Kim et al., 2014), a
624 mechanism must exist to ensure that they can also contact non-DS partners. We speculate that
625 SACs initially recruit their bipolar partners using long-range attractive cues, and then use
626 contact-repulsion (or an equivalent arbor sorting mechanism) to displace bipolar arbors such that
627 they remain in contact with the SAC layers but also innervate adjacent layers. This model is
628 consistent with bipolar arbor phenotypes in *Megf10* mutants, but will require further study.

629 **Role of MEGF10 in the functional assembly of DS circuitry**

630 We found that impairment of SAC interactions in the perinatal retina causes permanent
631 functional DS circuit deficits. In *Megf10* mutants, direction tuning of ooDSGCs becomes broader
632 and weaker, and their ON/OFF preferred directions are less aligned. Direction tuning is degraded
633 in large part because mutant ooDSGCs have aberrant spiking responses to null-direction stimuli.
634 This suggests that impaired null-direction inhibition – which arises from SACs – is a key
635 contributor to the phenotype. Broader ooDSGC tuning curves have been shown, in modeling
636 studies, to degrade population-level coding of directional information, and the ability of
637 downstream neurons to extract such information (Fiscella et al., 2015). Thus, the physiological
638 phenotypes we identified are likely sufficient to impair the ability of mutant retina to
639 appropriately relay visual information.

640 Dysfunctional DS circuit physiology in *Megf10* mutants is almost certainly a
641 consequence of its effects on development, because neurons do not express MEGF10 beyond the
642 second postnatal week (Kay et al., 2012). Further, even though MEGF10 is expressed by Müller
643 glia in adulthood, we have been unable to detect any changes in Müller glia anatomy or
644 interactions with DS circuit synapses upon loss of *Megf10* function (Wang et al., 2017; J.W. and
645 J.N.K., unpublished observations). We therefore conclude that anatomical changes to the DS
646 circuit arising during development are responsible for circuit dysfunction.

647 The fundamental change to DS circuit anatomy in *Megf10* mutants is altered distribution
648 of arbors and synapses, unlike other manipulations which simply serve to destroy SAC radial
649 morphology or disrupt synaptic partnering among DS circuit cells (Sun et al., 2013; Duan et al.,
650 2014; Kostadinov and Sanes, 2015; Peng et al., 2017). In *Megf10* mutants, the combined effect
651 of mosaic spacing defects and IPL laminar targeting errors is to disturb the regularity of SAC
652 IPL innervation. As a result, some parts of the visual map become over-innervated (e.g. Fig. 9A)
653 while others are uninnervated (Fig. 9C). In turn, ooDSGCs are recruited to the over-innervated
654 regions and excluded from uninnervated gaps, likely causing sporadic local inhomogeneity in
655 synapse density across visual space. According to some models of DS, which posit that the total
656 amount of SAC inhibition is the key factor underlying DS responsiveness, these relatively small-
657 scale changes would be considered unlikely to change circuit function (Taylor and Vaney, 2002;
658 Demb, 2007). A more recent alternate view is that the fine spatial arrangement of glutamatergic
659 inputs to SACs, and the synaptic balance of SAC and bipolar input onto ooDSGC dendrites, are
660 both important for DS responses (Ding et al., 2016; Vlasits et al., 2016; Poleg-Polsky and
661 Diamond, 2016; Sethuramanujam et al., 2016, 2017). The finding that *Megf10* mutants have DS
662 tuning phenotypes suggests that local synaptic arrangements are indeed important for the DS

663 computation. More broadly, this finding shows that the developmental mechanisms we describe
664 here are important for enabling circuit function, raising the possibility that other circuits
665 throughout the retina and CNS may use similar developmental mechanisms to establish their
666 functional connectivity.

667

668 **ACKNOWLEDGEMENTS**

669 For financial support we thank the National Eye Institute (EY024694 to JNK; EY026344
670 to TAR; EY024567 to GDF; EY5722 to Duke University); Pew Charitable Trusts, E. Matilda
671 Ziegler Foundation, McKnight Endowment Fund for Neuroscience, Alfred P. Sloan foundation
672 (JNK); the Whitehall Foundation (GDF); and Research to Prevent Blindness Unrestricted Grant
673 (Duke University). We thank Sidney Kuo and Greg Schwartz for suggesting use of the
674 *Gjd2:GFP* mouse line; members of the Kay lab and Cagla Eroglu for their comments on the
675 manuscript; Megan Stogsdill and Ari Pereira for mouse colony support; and X. Duan and J.
676 Sanes (Harvard) for *Kcng4*^{Cre} mice.

677

678 **COMPETING INTERESTS**

679 The authors have no competing interests to disclose.

680 **REFERENCES**

681 Amthor, F.R., and N.M. Grzywacz. 1993. Inhibition in ON-OFF directionally selective ganglion
682 cells of the rabbit retina. *J. Neurophysiol.* 69:2174–87.

683 Baier, H. 2013. Synaptic laminae in the visual system: molecular mechanisms forming layers of
684 perception. *Annu. Rev. Cell Dev. Biol.* 29:385–416. doi:10.1146/annurev-cellbio-101011-
685 155748.

686 Cai, D., K.B. Cohen, T. Luo, J.W. Lichtman, and J.R. Sanes. 2013. Improved tools for the
687 Brainbow toolbox. *Nat. Methods*. 10:540–7. doi:10.1038/nmeth.2450.

688 Chen, M., S. Lee, S.J.H. Park, L.L. Looger, and Z.J. Zhou. 2014. Receptive field properties of
689 bipolar cell axon terminals in direction-selective sublaminas of the mouse retina. *J.*
690 *Neurophysiol.* 112:1950–62. doi:10.1152/jn.00283.2014.

691 Chow, R.W., A.D. Almeida, O. Randlett, C. Norden, and W. a. Harris. 2015. Inhibitory neuron
692 migration and IPL formation in the developing zebrafish retina. *Development*. 142:2665–77.
693 doi:10.1242/dev.122473.

694 Chung, W.-S., L.E. Clarke, G.X. Wang, B.K. Stafford, A. Sher, C. Chakraborty, J. Joung, L.C.
695 Foo, A. Thompson, C. Chen, S.J. Smith, and B.A. Barres. 2013. Astrocytes mediate synapse
696 elimination through MEGF10 and MERTK pathways. *Nature*. 504:394–400.
697 doi:10.1038/nature12776.

698 Cooper, J.A. 2014. Molecules and mechanisms that regulate multipolar migration in the
699 intermediate zone. *Front. Cell. Neurosci.* 8:386. doi:10.3389/fncel.2014.00386.

700 Deans, M.R., A. Krol, V.E. Abraira, C.O. Copley, A.F. Tucker, and L. V Goodrich. 2011.
701 Control of neuronal morphology by the atypical cadherin Fat3. *Neuron*. 71:820–32.
702 doi:10.1016/j.neuron.2011.06.026.

703 Demb, J.B. 2007. Cellular mechanisms for direction selectivity in the retina. *Neuron*. 55:179–86.
704 doi:10.1016/j.neuron.2007.07.001.

705 Ding, H., R.G. Smith, A. Poleg-Polsky, J.S. Diamond, and K.L. Briggman. 2016. Species-
706 specific wiring for direction selectivity in the mammalian retina. *Nature*. 535:105–110.
707 doi:10.1038/nature18609.

708 Duan, X., A. Krishnaswamy, I. De la Huerta, and J.R. Sanes. 2014. Type II cadherins guide
709 assembly of a direction-selective retinal circuit. *Cell*. 158:793–807.
710 doi:10.1016/j.cell.2014.06.047.

711 Field, G.D., J.L. Gauthier, A. Sher, M. Greschner, T.A. Machado, L.H. Jepson, J. Shlens, D.E.
712 Gunning, K. Mathieson, W. Dabrowski, L. Paninski, A.M. Litke, and E.J. Chichilnisky.
713 2010. Functional connectivity in the retina at the resolution of photoreceptors. *Nature*.
714 467:673–7. doi:10.1038/nature09424.

715 Field, G.D., A. Sher, J.L. Gauthier, M. Greschner, J. Shlens, A.M. Litke, and E.J. Chichilnisky.
716 2007. Spatial properties and functional organization of small bistratified ganglion cells in

717 primate retina. *J. Neurosci.* 27:13261–72. doi:10.1523/JNEUROSCI.3437-07.2007.

718 Fiscella, M., F. Franke, K. Farrow, J. Müller, B. Roska, R. Azeredo da Silveira, and A.
719 Hierlemann. 2015. Visual coding with a population of direction-selective neurons. *J.*
720 *Neurophysiol.* 114:2485–2499. doi:10.1152/jn.00919.2014.

721 Fujitani, Y., S. Fujitani, H. Luo, F. Qiu, J. Burlison, Q. Long, Y. Kawaguchi, H. Edlund, R.J.
722 MacDonald, T. Furukawa, T. Fujikado, M.A. Magnuson, M. Xiang, and C.V.E. Wright.
723 2006. Ptf1a determines horizontal and amacrine cell fates during mouse retinal development.
724 *Development*. 133:4439–50. doi:10.1242/dev.02598.

725 Furuta, Y., O. Lagutin, B.L. Hogan, and G.C. Oliver. 2000. Retina- and ventral forebrain-
726 specific Cre recombinase activity in transgenic mice. *Genesis*. 26:130–2.

727 Galli-Resta, L., G. Resta, S.S. Tan, and B.E. Reese. 1997. Mosaics of islet-1-expressing
728 amacrine cells assembled by short-range cellular interactions. *J. Neurosci.* 17:7831–8.

729 Godinho, L., J.S. Mumm, P.R. Williams, E.H. Schroeter, A. Koerber, S.W. Park, S.D. Leach,
730 and R.O.L. Wong. 2005. Targeting of amacrine cell neurites to appropriate synaptic laminae
731 in the developing zebrafish retina. *Development*. 132:5069–79. doi:10.1242/dev.02075.

732 Green, E.S., J.L. Stubbs, and E.M. Levine. 2003. Genetic rescue of cell number in a mouse
733 model of microphthalmia: interactions between Chx10 and G1-phase cell cycle regulators.
734 *Development*. 130:539–52.

735 Greene, M.J., J.S. Kim, H.S. Seung, and EyeWirers. 2016. Analogous Convergence of Sustained
736 and Transient Inputs in Parallel On and Off Pathways for Retinal Motion Computation. *Cell*
737 *Rep.* 14:1892–900. doi:10.1016/j.celrep.2016.02.001.

738 Hinds, J.W., and P.L. Hinds. 1978. Early development of amacrine cells in the mouse retina: an
739 electron microscopic, serial section analysis. *J. Comp. Neurol.* 179:277–300.
740 doi:10.1002/cne.901790204.

741 Hoshiba, Y., T. Toda, H. Ebisu, M. Wakimoto, S. Yanagi, and H. Kawasaki. 2016. Sox11
742 Balances Dendritic Morphogenesis with Neuronal Migration in the Developing Cerebral
743 Cortex. *J. Neurosci.* 36:5775–84. doi:10.1523/JNEUROSCI.3250-15.2016.

744 Huberman, A.D., W. Wei, J. Elstrott, B.K. Stafford, M.B. Feller, and B.A. Barres. 2009. Genetic
745 identification of an On-Off direction-selective retinal ganglion cell subtype reveals a layer-
746 specific subcortical map of posterior motion. *Neuron*. 62:327–34.
747 doi:10.1016/j.neuron.2009.04.014.

748 Kay, J.N., M.W. Chu, and J.R. Sanes. 2012. MEGF10 and MEGF11 mediate homotypic
749 interactions required for mosaic spacing of retinal neurons. *Nature*. 483:465–9.
750 doi:10.1038/nature10877.

751 Kay, J.N., I. De la Huerta, I.-J. Kim, Y. Zhang, M. Yamagata, M.W. Chu, M. Meister, and J.R.
752 Sanes. 2011. Retinal ganglion cells with distinct directional preferences differ in molecular
753 identity, structure, and central projections. *J. Neurosci.* 31:7753–62.
754 doi:10.1523/JNEUROSCI.0907-11.2011.

755 Kay, J.N., and J.R. Sanes. 2013. Development of retinal arbors and synapses. *In* The New Visual
756 Neurosciences. J.S. Werner and L.M. Chalupa, editors. MIT Press, Cambridge.

757 Kim, J.S., M.J. Greene, A. Zlateski, K. Lee, M. Richardson, S.C. Turaga, M. Purcaro, M.
758 Balkam, A. Robinson, B.F. Behabadi, M. Campos, W. Denk, H.S. Seung, and EyeWirers.
759 2014. Space-time wiring specificity supports direction selectivity in the retina. *Nature*.
760 509:331–6. doi:10.1038/nature13240.

761 Knabe, W., S. Washausen, N. Happel, and H.J. Kuhn. 2007. Development of starburst
762 cholinergic amacrine cells in the retina of Tupaia belangeri. *J. Comp. Neurol.* 502:584–597.
763 doi:10.1002/cne.

764 Kostadinov, D., and J.R. Sanes. 2015. Protocadherin-dependent dendritic selfavoidance regulates
765 neural connectivity and circuit function. *Elife*. 4. doi:10.7554/eLife.08964.

766 Krah, N.M., J.-P. De La O, G.H. Swift, C.Q. Hoang, S.G. Willet, F. Chen Pan, G.M. Cash, M.P.
767 Bronner, C.V. Wright, R.J. MacDonald, and L.C. Murtaugh. 2015. The acinar
768 differentiation determinant PTF1A inhibits initiation of pancreatic ductal adenocarcinoma.
769 *Elife*. 4. doi:10.7554/eLife.07125.

770 Krol, A., S.J. Henle, and L. V Goodrich. 2016. Fat3 and Ena/VASP proteins influence the
771 emergence of asymmetric cell morphology in the developing retina. *Development*.
772 143:2172–82. doi:10.1242/dev.133678.

773 Lefebvre, J.L., J.R. Sanes, and J.N. Kay. 2015. Development of dendritic form and function.
774 *Annu. Rev. Cell Dev. Biol.* 31:741–77. doi:10.1146/annurev-cellbio-100913-013020.

775 Madisen, L., T.A. Zwingman, S.M. Sunkin, S.W. Oh, H.A. Zariwala, H. Gu, L.L. Ng, R.D.
776 Palmiter, M.J. Hawrylycz, A.R. Jones, E.S. Lein, and H. Zeng. 2010. A robust and high-
777 throughput Cre reporting and characterization system for the whole mouse brain. *Nat.*
778 *Neurosci.* 13:133–40. doi:10.1038/nn.2467.

779 Matsuoka, R.L., K.T. Nguyen-Ba-Charvet, A. Parray, T.C. Badea, A. Chédotal, and A.L.
780 Kolodkin. 2011. Transmembrane semaphorin signalling controls laminar stratification in the
781 mammalian retina. *Nature*. 470:259–63. doi:10.1038/nature09675.

782 Morgan, J.L., A. Dhingra, N. Vardi, and R.O.L. Wong. 2006. Axons and dendrites originate
783 from neuroepithelial-like processes of retinal bipolar cells. *Nat. Neurosci.* 9:85–92.
784 doi:10.1038/nn1615.

785 Moshiri, A., E. Gonzalez, K. Tagawa, H. Maeda, M. Wang, L.J. Frishman, and S.W. Wang. 2008.
786 Near complete loss of retinal ganglion cells in the math5/brn3b double knockout elicits
787 severe reductions of other cell types during retinal development. *Dev. Biol.* 316:214–27.
788 doi:10.1016/j.ydbio.2008.01.015.

789 Muzumdar, M.D., B. Tasic, K. Miyamichi, L. Li, and L. Luo. 2007. A global double-fluorescent
790 Cre reporter mouse. *genesis*. 45:593–605. doi:10.1002/dvg.20335.

791 Nadarajah, B., J.E. Brunstrom, J. Grutzendler, R.O. Wong, and A.L. Pearlman. 2001. Two
792 modes of radial migration in early development of the cerebral cortex. *Nat. Neurosci.*

793 4:143–50. doi:10.1038/83967.

794 Nakhai, H., S. Sel, J. Favor, L. Mendoza-Torres, F. Paulsen, G.I.W. Duncker, and R.M. Schmid.
795 2007. Ptf1a is essential for the differentiation of GABAergic and glycinergic amacrine cells
796 and horizontal cells in the mouse retina. *Development*. 134:1151–60.
797 doi:10.1242/dev.02781.

798 Oesch, N., T. Euler, and W.R. Taylor. 2005. Direction-selective dendritic action potentials in
799 rabbit retina. *Neuron*. 47:739–50.

800 Oyster, C.W., and H.B. Barlow. 1967. Direction-selective units in rabbit retina: distribution of
801 preferred directions. *Science*. 155:841–842. doi:10.1126/science.155.3764.841.

802 Peng, Y.R., N.M. Tran, A. Krishnaswamy, D. Kostadinov, E.M. Martersteck, and J.R. Sanes.
803 2017. Satb1 Regulates Contactin 5 to Pattern Dendrites of a Mammalian Retinal Ganglion
804 Cell. *Neuron*. 95:869–883.e6. doi:10.1016/j.neuron.2017.07.019.

805 Poleg-Polsky, A., and J.S. Diamond. 2016. Retinal Circuitry Balances Contrast Tuning of
806 Excitation and Inhibition to Enable Reliable Computation of Direction Selectivity. *J.*
807 *Neurosci.* 36:5861–76. doi:10.1523/JNEUROSCI.4013-15.2016.

808 Rawlins, E.L., T. Okubo, Y. Xue, D.M. Brass, R.L. Auten, H. Hasegawa, F. Wang, and B.L.M.
809 Hogan. 2009. The role of Scgb1a1+ Clara cells in the long-term maintenance and repair of
810 lung airway, but not alveolar, epithelium. *Cell Stem Cell*. 4:525–34.
811 doi:10.1016/j.stem.2009.04.002.

812 Rossi, J., N. Balthasar, D. Olson, M. Scott, E. Berglund, C.E. Lee, M.J. Choi, D. Lauzon, B.B.
813 Lowell, and J.K. Elmquist. 2011. Melanocortin-4 receptors expressed by cholinergic
814 neurons regulate energy balance and glucose homeostasis. *Cell Metab.* 13:195–204.
815 doi:10.1016/j.cmet.2011.01.010.

816 Sanes, J.R., and M. Yamagata. 2009. Many paths to synaptic specificity. *Annu. Rev. Cell Dev.*
817 *Biol.* 25:161–95. doi:10.1146/annurev.cellbio.24.110707.175402.

818 Sanes, J.R., and S.L. Zipursky. 2010. Design principles of insect and vertebrate visual systems.
819 *Neuron*. 66:15–36. doi:10.1016/j.neuron.2010.01.018.

820 Schindelin, J., I. Arganda-Carreras, E. Frise, V. Kaynig, M. Longair, T. Pietzsch, S. Preibisch, C.
821 Rueden, S. Saalfeld, B. Schmid, J.-Y. Tinevez, D.J. White, V. Hartenstein, K. Eliceiri, P.
822 Tomancak, and A. Cardona. 2012. Fiji: an open-source platform for biological-image
823 analysis. *Nat. Methods*. 9:676–82. doi:10.1038/nmeth.2019.

824 Sethuramanujam, S., A.J. McLaughlin, G. DeRosenroll, A. Hoggarth, D.J. Schwab, and G.B.
825 Awatramani. 2016. A Central Role for Mixed Acetylcholine/GABA Transmission in
826 Direction Coding in the Retina. *Neuron*. 90:1243–56. doi:10.1016/j.neuron.2016.04.041.

827 Sethuramanujam, S., X. Yao, G. DeRosenroll, K.L. Briggman, G.D. Field, and G.B. Awatramani.
828 2017. “Silent” NMDA Synapses Enhance Motion Sensitivity in a Mature Retinal Circuit.
829 *Neuron*. 96:1099–1111.e3. doi:10.1016/j.neuron.2017.09.058.

830 Stacy, R.C., and R.O.L. Wong. 2003. Developmental relationship between cholinergic amacrine
831 cell processes and ganglion cell dendrites of the mouse retina. *J. Comp. Neurol.* 456:154–66.
832 doi:10.1002/cne.10509.

833 Sun, L.O., Z. Jiang, M. Rivlin-Etzion, R. Hand, C.M. Brady, R.L. Matsuoka, K.-W. Yau, M.B.
834 Feller, and A.L. Kolodkin. 2013. On and off retinal circuit assembly by divergent molecular
835 mechanisms. *Science*. 342. doi:10.1126/science.1241974.

836 Tabata, H., and K. Nakajima. 2003. Multipolar migration: the third mode of radial neuronal
837 migration in the developing cerebral cortex. *J. Neurosci.* 23:9996–10001. doi:23/31/9996
838 [pii].

839 Taylor, W.R., and D.I. Vaney. 2002. Diverse synaptic mechanisms generate direction selectivity
840 in the rabbit retina. *J. Neurosci.* 22:7712–20.

841 Trenholm, S., K. Johnson, X. Li, R.G. Smith, and G.B. Awatramani. 2011. Parallel mechanisms
842 encode direction in the retina. *Neuron*. 71:683–94. doi:10.1016/j.neuron.2011.06.020.

843 Vaney, D.I., and D. V Pow. 2000. The dendritic architecture of the cholinergic plexus in the
844 rabbit retina: selective labeling by glycine accumulation in the presence of sarcosine. *J.*
845 *Comp. Neurol.* 421:1–13.

846 Vaney, D.I., B. Sivyer, and W.R. Taylor. 2012. Direction selectivity in the retina: symmetry and
847 asymmetry in structure and function. *Nat. Rev. Neurosci.* 13:194–208. doi:10.1038/nrn3165.

848 Visser, J.J., Y. Cheng, S.C. Perry, A.B. Chastain, B. Parsa, S.S. Masri, T.A. Ray, J.N. Kay, and
849 W.M. Wojtowicz. 2015. An extracellular biochemical screen reveals that FLRTs and Unc5s
850 mediate neuronal subtype recognition in the retina. *Elife*. 4:e08149.
851 doi:10.7554/eLife.08149.

852 Vlasits, A.L., R.D. Morrie, A. Tran-Van-Minh, A. Bleckert, C.F. Gainer, D.A. DiGregorio, and
853 M.B. Feller. 2016. A Role for Synaptic Input Distribution in a Dendritic Computation of
854 Motion Direction in the Retina. *Neuron*. 89:1317–1330. doi:10.1016/j.neuron.2016.02.020.

855 Wang, J., M.L. O'Sullivan, D. Mukherjee, V.M. Puñal, S. Farsiu, and J.N. Kay. 2017. Anatomy
856 and spatial organization of Müller glia in mouse retina. *J. Comp. Neurol.* 525:1759–1777.
857 doi:10.1002/cne.24153.

858 Wässle, H., C. Puller, F. Müller, and S. Haverkamp. 2009. Cone contacts, mosaics, and
859 territories of bipolar cells in the mouse retina. *J. Neurosci.* 29:106–17.
860 doi:10.1523/JNEUROSCI.4442-08.2009.

861 Whitney, I.E., P.W. Keeley, A.J. St John, A.G. Kautzman, J.N. Kay, and B.E. Reese. 2014. Sox2
862 regulates cholinergic amacrine cell positioning and dendritic stratification in the retina. *J.*
863 *Neurosci.* 34:10109–21. doi:10.1523/JNEUROSCI.0415-14.2014.

864 Xu, H.-P., T.J. Burbridge, M. Ye, M. Chen, X. Ge, Z.J. Zhou, and M.C. Crair. 2016. Retinal
865 Wave Patterns Are Governed by Mutual Excitation among Starburst Amacrine Cells and
866 Drive the Refinement and Maintenance of Visual Circuits. *J. Neurosci.* 36:3871–3886.
867 doi:10.1523/JNEUROSCI.3549-15.2016.

868 Yamagata, M., and J.R. Sanes. 2008. Dscam and Sidekick proteins direct lamina-specific
869 synaptic connections in vertebrate retina. *Nature*. 451:465–9. doi:10.1038/nature06469.

870 Yang, L., C.-L. Cai, L. Lin, Y. Qyang, C. Chung, R.M. Monteiro, C.L. Mummery, G.I. Fishman,
871 A. Cogen, and S. Evans. 2006. Isl1Cre reveals a common Bmp pathway in heart and limb
872 development. *Development*. 133:1575–85. doi:10.1242/dev.02322.

873 Yu, W.-Q., N.M. Grzywacz, E.-J. Lee, and G.D. Field. 2017. Cell-type specific changes in
874 retinal ganglion cell function induced by rod death and cone reorganization in rats. *J.*
875 *Neurophysiol.* jn.00826.2016. doi:10.1152/jn.00826.2016.

876

877 **MATERIALS AND METHODS**

878 **KEY RESOURCES TABLE**

Reagent type	Designation	Source or Reference	Identifier	Additional information
Antibody	Megf10: rabbit, 1:1000	Kay et al., 2012		
Antibody	Sox2: rabbit, 1:500	Abcam	ab97959	
Antibody	Sox2: goat, 1:500	Santa Cruz	sc-17320	
Antibody	ChAT: goat, 1:400	EMD Millipore	AB144P	
Antibody	Beta Galactosidase: rabbit, 1:5000	other		Antibody was a gift of J.R. Sanes, Harvard
Antibody	GFP: chicken, 1:1000	Life Technologies	A10262	
Antibody	GFP (Co-IP): rabbit, 1:1000	Thermo Fisher Scientific	A-6455	
Antibody	AP-2a: mouse, 1:200	Developmental Studies Hybridoma Bank	3B5	
Antibody	RBPMS: guinea pig, 1:2000	other		Antibody was a gift of N. Brecha, UCLA
Antibody	Chx10: sheep, 1:300	Exalpha	X1180P	
Antibody	Chx10: goat, 1:500	Santa Cruz	sc-21690	
Antibody	GAD65: rabbit, 1:1000	Millipore	AB1511	
Antibody	FLAG: mouse, 1:500	Sigma Aldrich	F-1804	
Antibody	VGLUT3 guinea pig	synaptic systems	135 204	
Antibody	Synaptotagmin-2 (Syt2), mouse, 1:250	Zebrafish International Resource Center	ZDB-ATB-081002-25	
Antibody	Isl1: mouse, 1:25	Developmental Studies Hybridoma Bank	39.4D5	
Antibody	Internexin: rabbit, 1:1000	EMD Millipore	AB5354	
Antibody	Normal Rabbit IgG	Cell signaling Technology	2729S	
Antibody	Normal Mouse IgG	Cell Signaling Technology	5415S	
Antibody	Alexa Fluor 488 AffiniPure Donkey Anti-Chicken: 1:1000	Jackson ImmunoResearch	703-545-155	
Antibody	Alexa Fluor 488 AffiniPure Donkey Anti-rabbit: 1:1000	Jackson ImmunoResearch	711-545-152	
Antibody	Alexa Fluor 488 AffiniPure Donkey Anti-goat: 1:1000	Jackson ImmunoResearch	705-545-147	

Antibody	Alexa Fluor 488 AffiniPure Donkey Anti-mouse: 1:1000	Jackson ImmunoResearch	706-605-148	
Antibody	Alexa Fluor 647 AffiniPure Donkey Anti-rabbit: 1:1000	Jackson ImmunoResearch	705-605-147	
Antibody	Cy3-AffiniPure Donkey Anti-rabbit: 1:1000	Jackson ImmunoResearch	715-165-151	
Antibody	Cy3-AffiniPure Donkey Anti-Guinea Pig: 1:1000	Jackson ImmunoResearch	706-165-148	
Antibody	Cy3-AffiniPure Donkey Anti-Goat: 1:1000	Jackson ImmunoResearch	705-165-147	
Antibody	IRDye® 680RD Donkey anti-Mouse IgG (H + L): 1:1000	Li-Cor Biosciences	925-68072	
Antibody	IRDye® 800CW Donkey anti-Rabbit IgG (H + L): 1:1000	Li-Cor Biosciences	925-32213	
biological sample (AAV)	AAV9.hEF1a.lox.TagBFP.lox.eYFP.lox.WPRE.hGH-InvBYF(Harvard)	Penn Vector Core	AV-9-PV2453	
biological sample (AAV)	AAV9.hEF1a.lox.mCherry.lox.mTFP1.lox.WPRE.hGH-InvCheTF(Harvard)	Penn Vector Core	AV-9-PV2454	
chemical compound	Fetal Bovine Serum	Life Technologies	16250-078	
chemical compound	Opti-MEM® I Reduced Serum Medium	Thermo Fisher Scientific	31985070	
chemical compound	Polyethylenimine (PEI), Linear (MW 25,000)	VWR/Polysiciences	23966-2	
chemical compound	16% Paraformaldehyde	Electron Microscopy Sciences	15710	
chemical compound	Normal Donkey Serum	Jackson ImmunoResearch	017-000-121	
Other	Immun-Blot Low Fluorescence PVDF membrane	Bio-Rad	1620264	
chemical compound	Fluoromount G	SouthernBiotech	0100-01	
chemical compound	Hoechst 33258	Invitrogen	H21491	
chemical compound	Isothesia: Isoflurane	Henry Schein	11695-6776	
chemical compound	Tissue Freezing Medium	VWR	15148-031	

chemical compound	Acrylamide/Bis solution	Bio-Rad	161-0158	
chemical compound	4x Laemmli Sample Buffer	Bio-Rad	1610747	
chemical compound	Immun-Blot® Low Fluorescence PVDF membrane	Bio-Rad	1620264	
chemical compound	Odyssey Blocking Buffer	Li-Cor Biosciences	927-40000	
chemical compound	Dynabeads® Protein G for Immunoprecipitation	Thermo Fisher Scientific	10003D	
chemical compound	cOmplete™, Mini, EDTA-free Protease Inhibitor Cocktail Tablets	Roche	4693159001	
commercial assay or kit	Bio-Rad DC Protein Assay Kit	Bio-Rad	5000112	
strain (mus musculus)	Mouse: Megf10^{LacZ}	Kay et al., 2012	Megf10$^{tm1b(KOMP)Jrs}$	
strain (mus musculus)	Mouse: Megf10^{flox}	this study	Megf10^{tm1c}	see Methods ("Animals" section)
strain (mus musculus)	Mouse: Ptf1a^{cko}	Krah et al., 2015	Ptf1a^{tm3Cvw}	
strain (mus musculus)	Mouse: Isl1^{Cre}	Jackson Labs 024242	Isl1$^{tm1(cre)Sev/J}$	
strain (mus musculus)	Mouse: Hb9:GFP	Jackson Labs 005029	B6.Cg-Tg(Hlxb9-GFP)1Tmj/J	
strain (mus musculus)	Mouse: ChAT^{Cre}	Jackson Labs 006410	Chat$^{tm2(cre)Lowl}$	
strain (mus musculus)	Mouse: Six3:Cre	Jackson Labs 019755	Tg(Six3-cre)69Frty	
strain (mus musculus)	Mouse: Kcng4^{Cre}	Jackson Labs 029414	Kcng4$^{tm1.1(cre)Jrs}$	
strain (mus musculus)	Mouse: Drd4:GFP	Huberman et al., 2009	Tg(Drd4-EGFP)W18Gsat	
strain (mus musculus)	Mouse: Gjd2:GFP	MMRRC	Tg(Gjd2-EGFP)JM16Gsat/Mmucd; RRID:MMRRC_030611-UCD	
strain (mus musculus)	Mouse: Rosa26^{mTmG}	Jackson Labs 007676	Gt(ROSA)26Sor$^{tm4(ACTB-tdTomato,-EGFP)Luo}$	
strain (mus musculus)	Mouse: Rosa26^{fGFP}	Rawlins et al., 2009	Gt(ROSA)26Sor$^{tm1(CAG-EGFP)Blh}$	
strain (mus musculus)	Mouse: Ai14	Jackson Labs 007914	B6.Cg-Gt(ROSA)26Sor$^{tm14(CAG-tdTomato)Hze/J}$	

strain (mus musculus)	Mouse: ACTB:FLPe B6;SJL	Jackson Labs 003800	B6;SJL-Tg(ACTFLPe)9205Dym/J	
strain (mus musculus)	Mouse: Gad1:GFP	Jackson Labs 007677	Tg(Gad1-EGFP)G42Zjh	
strain (mus musculus)	Mouse: C57Bl6/J	Jackson Labs 000664	C57BL/6J	
cell line (human)	HEK293T	ATCC	293T (ATCC® CRL-3216™)	Cell line was authenticated by ATCC at time of purchase
recombinant DNA reagent	CMV-M10-FLAG	this paper		see "Method Details" section
recombinant DNA reagent	CMV-M10-GFP	Kay et al., 2012		
recombinant DNA reagent	pCMV-MEGF10-ΔICD-GFP	Kay et al., 2012		
recombinant DNA reagent	MEGF10-ΔICD-Flag	this paper		see "Method Details" section
recombinant DNA reagent	pAAV-EF1a-Brainbow-tagBFP-EYFP-WPRE	Addgene	45185	
recombinant DNA reagent	pAAV-EF1a-Brainbow-mTFP1-Cherry-WPRE	Addgene	45816	
software	Fiji/ImageJ	Schindelin et al., 2012		
software	Prism	GraphPad		
software	NIS Elements	Nikon Instruments		
software	Custom JAVA scripts for spike sorting	Yu et al. 2017		
software	Matlab	Mathworks, Natick, MA		
software	Image Studio™	LI-COR Biosciences		
software	Photoshop	Adobe		
sequence-based reagent	M10flagNotI_Rev	IDT	ATAGCGGCCGCttaCTTGTCGTCATCGTCTTTGTAGTCttcactgctgctgctgctgctg	
sequence-based reagent	M10flag_Fwd	IDT	GGTACATGCCTGTGCGAAGCA	
sequence-based reagent	Cyto9_flag_Rev1	IDT	5'ATAGCGGCCGCttaCTTGTCGTCATCGTCTTTGTAGTCTTCCTTCCTCTTCTGCTTGTGT	

879

880 **METHOD DETAILS**

881 **Animals**

882 All animal experiments were reviewed and approved by the Institutional Animal Care
883 and Use Committee of Duke University. The animals were maintained under a 12-hour light-
884 dark cycle with *ad lib* access to food and water. Retinas from adult (4-8 weeks old) *Megf10*$^{-/-}$
885 mutant mice and wild-type control mice with same genetic background were used for
886 experiments performed on the multielectrode array (MEA). Animals were dark-adapted
887 overnight prior to the experiment.

888 For this study the following transgenic and mutant mouse lines were used: 1)
889 *Megf10*$^{tm1b(KOMP)Jrs}$ (Kay et al., 2012), referred to as *Megf10*$^{-}$ or *Megf10*^{lacZ}; 2) *Ptf1a*^{tm3Cvw} (Krah
890 et al., 2015), referred to as *Ptf1a*^{flox} or (when crossed to Cre mice) *Ptf1a*^{cKO}; 3) *Isl1*$^{tm(cre)Sev}$ (Yang
891 et al., 2006), referred to as *Isl1*^{Cre}; 4) *Hb9:GFP* (Trenholm et al., 2011); 5) *Chat*$^{tm2(cre)Lowl}$ (Rossi
892 et al., 2011), referred to as *Chat*^{Cre}; 6) *Tg(Six3-cre)69Frty* (Furuta et al., 2000) referred to as
893 *Six3:Cre*; 7) *Kcng4*$^{tm1.1(cre)Jrs}$ (Duan et al., 2014) referred to as *Kcng4*^{Cre}; 8) *Tg(Drd4-*
894 *EGFP)W18Gsat* (Huberman et al., 2009), referred to as *Drd4:GFP*; 9) *Tg(Gjd2-*
895 *EGFP)JM16Gsat*, referred to as *Gjd2:GFP*; 10) *Tg(Gad1-EGFP)G42Zjh*, referred to as
896 *Gad1:GFP*. Two Cre reporter strains were used that express membrane-targeted green
897 fluorescent protein (mGFP) upon Cre recombination: 1) *Gt(ROSA)26Sor*$^{tm4(ACTB-tdTomato,-EGFP)Luo}$,
898 also known as *mT/mG* (Muzumdar et al., 2007); 2) *Rosa26*^{fGFP} (Rawlins et al., 2009). An
899 additional Cre reporter strain was used that expresses tdTomato fluorescent protein upon Cre
900 recombination: *Gt(ROSA)26Sor*$^{tm14(CAG-tdTomato)Hze}$ (Madisen et al., 2010). See Key Resources
901 table for repository stock numbers where applicable.

902 To produce *Megf10*^{flox} mice, *Megf10*$^{tm1a(KOMP)Jrs}$ mice (Kay et al., 2012) were crossed to
903 germline Cre strain *B6;SJL-Tg(ACTFLPe)9205Dym/J*, thereby generating a functional allele
904 (also known as *Megf10*^{tm1c}) in which exon 4 was flanked by loxP sites.

905 **Cell Culture**

906 HEK293T cells were obtained from ATCC. The cells were cultured in Dulbecco's
907 Modified Eagle's Medium (DMEM) with 10% bovine growth serum, 4.5 g/L D-glucose, 2.0 mM
908 L-glutamine, 1% Penicillin/Streptomycin in 10 cm cell culture dishes. Cells were passaged every
909 2-3 days to reach confluence. Before splitting, culture media were removed and Dulbecco's
910 phosphate-buffered saline (D-PBS) was used to rinse cell layers as well as removing residual
911 serum. Cells were detached from dish with 4 ml of 0.05% Trypsin and incubated at 37ºC until
912 cell layer is dispersed (about 5 minutes). Equal volume of complete culture media was added to
913 the dish to inhibit protease activity. The suspension was centrifuged at 200 x g for 5 minutes.
914 Supernatant was aspirated and the cells were suspended with appropriate amount of media and
915 plated (1:4-1:8). Cells used for experiments were passaged no more than 10 times. Cell stocks
916 were stored as 2 million cells per vial in complete culture media with 10% DMSO in liquid
917 nitrogen.

918 **Identification of DS circuit cell types using antibody and transgenic markers**

919 *SAC markers in mature retina*

920 Antibodies to choline acetyltransferase (ChAT) were used as a SAC marker in mice older
921 than P5. This antibody stains SAC somata and their dendrites in the IPL (e.g. Fig. 8A).

922 *SAC markers in embryonic and neonatal retina*

923 Antibodies to ChAT and vesicular acetylcholine transporter, typically used as SAC
924 markers in the mature retina, do not stain reliably in the embryonic and neonatal (P0-P3) mouse
925 retina, precluding their use as markers during one of the key time periods of this study. We
926 therefore characterized several other SAC markers that we found to be suitable for definitive
927 SAC identification and their anatomical characterization in the E16-P3 period:

928 The *Megf10*^{lacZ} allele (Kay et al., 2012) drives strong, selective β-galactosidase (βgal)
929 expression in all SACs starting at embryonic day (E)17 (Fig. 1B; Fig. 1-Supplement 1; data not
930 shown). Horizontal cells are also labeled. Expression is strong enough to allow characterization
931 of SAC dendrite anatomy at these early stages. Antibodies to *Megf10* yield a similar staining
932 pattern (Fig. 1-Supplement 1; Fig. 4B,C), but staining of fine dendritic arbors was brighter with
933 anti-βgal staining of *Megf10*^{lacZ} mice, so this approach was used for most of our anatomical
934 experiments analyzing the full SAC population at or before P3. In some such experiments a
935 *Megf11*^{lacZ} allele (Kay et al., 2012) was also present; this allele drives βgal expression in
936 essentially the same pattern as *Megf10*^{lacZ} and therefore contributed to signal brightness. The
937 presence of this allele had no apparent effect on SAC anatomy, in either wild-type or *Megf10*
938 mutant background.

939 Antibodies to Sox2 (Whitney et al., 2014) strongly label all SAC nuclei in the INL and
940 GCL, starting at embryonic stages (Fig. 1-Supplement 1; Fig. 2D,E,G). Progenitor cells in the
941 ONBL are also labeled. This marker was typically used in conjunction with *Megf10*^{lacZ} to
942 provide definitive identification of SACs as βgal^{+}Sox2^{+} cells.

943 Antibodies to internexin label SAC intermediate filaments, which localize in a polarized
944 manner to the primary dendrite(s) and the side of the cell body from which they emerge (Fig. 2-

945 Supplement 1). Primary dendrites were defined as any first-order dendrite branch, i.e. those
946 arising directly from the cell body. Internexin is a selective marker of SAC in perinatal mouse
947 retina, as previously shown in tree shrew (Knabe et al., 2007). RGC axons are also labeled (Fig.
948 2-Supplement 1).

949 Antibodies to Isl1 (Fig. 2A) label all SAC nuclei, starting at cell cycle exit (Galli-Resta et
950 al., 1997). A large subset of RGCs are also labeled. The *Isl1*^{Cre} knock-in mouse (Yang et al.,
951 2006) faithfully recapitulated this expression pattern (Fig. 2A,B) and was used to study SAC
952 anatomy at embryonic stages (see below for further details).

953 *SAC single-cell labeling*

954 To assess the single-cell morphology of individual SACs during early postnatal
955 development, the *Chat*^{Cre} line was used. In contrast to mature retina (e.g. Fig. 8B), in which all
956 SACs were labeled, *Chat*^{Cre} expression was rare and sporadic in early postnatal retina (Fig. 1C;
957 Fig. 1-Supplement 1), as reported previously (Xu et al., 2016). Therefore, when crossed with Cre
958 reporter mice to make *Chat*^{mG} animals, the full anatomy of individual SACs was clearly
959 delineated (e.g. Fig. 2H-K). We did not typically observe Cre recombination in non-SAC cell
960 types; nevertheless, we always co-stained with another SAC marker, either Sox2 or *Megf10:*βgal,
961 to confirm the SAC identity of the cells that were analyzed.

962 *ooDSGC markers*

963 Two mouse lines were used, each of which labels distinct types of ooDSGCs. *Hb9:GFP*
964 labels the superior subtype of ooDSGC, while *Drd4:GFP* labels the posterior subtype of
965 ooDSGC (Trenholm et al., 2011; Huberman et al., 2009).

966 *DS-circuit bipolar cell markers*

967 Four types of bipolar cells have been shown to make monosynaptic connections with
968 SACs and/or ooDSGCs: Types BC2, BC3a, BC5, and BC7 (Duan et al., 2014; Ding et al., 2016;
969 Greene et al., 2016; Kim et al., 2014; Chen et al., 2014). OFF bipolar cells BC2 and BC3a were
970 labeled, respectively, by antibodies to Syt2 and HCN4 (Wässle et al., 2009).

971 ON bipolar cells BC5 and BC7 were marked with *Kcng4*^{Cre} (Duan et al., 2014) crossed to
972 mGFP Cre reporter mice (denoted *Kcng4*^{mG}). Labeling of BC7 was more prominent with the
973 Rosa26 locus mGFP Cre reporter line that we used, compared to the cytosolic GFP reporter
974 driven by Thy1 that was used by Duan et al. (2014).

975 *Gjd2-GFP* was also used to label BC5 bipolar cells (Fig. 11-Supplement 1). In adult
976 retina, GFP was strongly expressed by a bipolar cell type that ramified in a laminar location
977 typical of BC5 (Sidney Kuo, University of Washington, personal communication). We
978 confirmed this expression pattern; weak expression in amacrine cells was also noted (Fig. 11-
979 Supplement 1). At earlier developmental stages the amacrine cell staining was much stronger and
980 filled many amacrine processes throughout the IPL, precluding use of this line for developmental
981 studies of bipolar axons (M. Stogsdill and J.N.K, unpublished observations).

982 **Immunohistochemistry**

983 *Retinal cross sections:*

984 Mice were anesthetized by isoflurane or cryoanesthesia (neonates only) followed by
985 decapitation. Eyes were enucleated, washed in PBS, and fixed in PBS containing 4%
986 formaldehyde (pH 7.5) for 1.5 hours at 4° C. After fixation, eyes were washed 3X with PBS and
987 stored in PBS containing 0.02% sodium azide at 4° C until further processing. Retinas were

988 dissected from the eyecup, cryoprotected by equilibration in PBS containing 30% sucrose, then
989 embedded in Tissue Freezing Medium and frozen by submersion in 2-methylbutane chilled by
990 dry ice. Tissue sections were cut on a cryostat to 20 µm and mounted on Superfrost Plus slides.
991 Slides were dried on a slide warmer for 1 h then stored at -80° C or used immediately.

992 For antibody labeling, slides were washed for 5 min with gentle agitation in PBS to
993 remove embedding medium and blocked for 1 h in PBS + 0.3% Triton X-100 (PBS-Tx)
994 containing 3-5% normal donkey serum. Primary antibodies were diluted in blocking buffer,
995 added to slides, then incubated overnight at 4° C. Slides were washed with PBS 3X for 10
996 minutes followed by incubation with secondary antibody diluted in PBS-Tx for 1-2 h at RT.
997 Slides were washed again with PBS 3X for 10 minutes then coverslipped using Fluoromount G.

998 *Retinal whole-mounts:*

999 Tissue was processed as above up to the point of dissection from the eyecup. After
1000 dissection from eyecup, retinas were washed in PBS then blocked for 3 hours with agitation at 4°
1001 C in blocking buffer (constituted as described above). Primary antibodies were diluted in
1002 blocking buffer, added to retinas, and incubated for 5-7 days with gentle agitation at 4°C. Retinas
1003 were washed 3X with PBS over the course of 2 hours with gentle agitation. Secondary antibody
1004 was diluted in PBS containing 0.3% Triton X-100 and was added to retinas followed by
1005 incubation overnight at 4° C with gentle agitation. Retinas were washed again 3X in PBS over
1006 the course of 2 hours with gentle agitation. For mounting on slides, 4 radial incisions separated
1007 by 90° were made centripetally, approximately 1/3 the radius of the retina. Retinas were flattened
1008 on nitrocellulose paper photoreceptor side down and coverslipped with Fluoromount G.

1009 *Image acquisition and processing*

1010 Sections and whole-mounts were imaged on a Nikon A1 or an Olympus FV300 confocal
1011 microscope. Image Z-stacks (Z-resolution 0.4 - 0.5 µm for whole-mount images; 0.8 - 1.0 µm for
1012 cross-sections) were imported to Fiji (Schindelin et al., 2012), de-noised by median-filtering (0.5
1013 - 2.0 pixel radius), and projected to a single plane. The portion of the stack selected for
1014 maximum-intensity projection was determined by the Z-volume of the structure to be depicted in
1015 the final image. Except where noted, data analysis and quantification was only performed using
1016 original stacks, not Z-projections. Color channels were assembled, and minor adjustments to
1017 brightness and contrast were made, in Adobe Photoshop. When images were to be compared,
1018 equivalent adjustments were performed on all images in the experiment. The width of the IPL is
1019 marked in many of the figures; this was determined by one of the following methods: 1)
1020 counterstaining with Hoechst to label all cell nuclei; 2) tdTomato fluorescence from
1021 unrecombined cells in *mT/mG* mice, which fills the IPL; 3) immunofluorescence against GAD65,
1022 which also fills the IPL; 4) autofluorescence signal intensity differences between soma layers
1023 and IPL.

1024 **Analysis of SAC anatomy in embryonic retina**

1025 To study SAC anatomy during embryonic stages, $Isl1^{Cre}$ was crossed to *lox-stop-lox-*
1026 *mGFP* Cre reporter mice (*mT/mG* or $Rosa26^{GFPf}$; see Key Reagents) to generate $Isl1^{mG}$ animals.
1027 Timed-pregnant dams were sacrificed at E16 and eyes collected from embryos (n = 11 mice
1028 from 3 litters). Tissue was processed as described for postnatal eyes, except fixation time was 60
1029 min. Cross-sections were stained with anti-GFP to reveal the morphology of $Isl1^{mG}$-expressing
1030 neurons, as well as Sox2 to distinguish $Isl1^{mG}$-positive SACs from RGCs. (All cells shown in Fig.
1031 2B-G were confirmed to be SACs by Sox2 co-labeling.) In combination with these markers, anti-

1032 internexin staining was used to assess orientation of primary dendrites. Location and/or presence
1033 of the IPL was determined using Hoechst nuclear staining, which revealed cell body-free
1034 neuropil regions, and/or by *Isl1*^{mG} labeling of neuronal processes, which filled these neuropil
1035 regions (Fig. 2-Supplement 2). We assessed anatomy of mGFP^{+} migrating SACs in the ONBL,
1036 as well as SACs in the INBL that were concluding their migration. Morphology of ON SACs in
1037 the GCL could not be discerned due to *Isl1* expression by RGCs (Fig. 2A,B), but because
1038 displaced amacrine cells pause at the INL-IPL border before crossing to the GCL (Chow et al.,
1039 2015), the population of cells available to analyze might have included both ON and OFF SACs.

1040 To measure the orientation of primary dendrites at E16 and P1, the angle ROI function in
1041 ImageJ was used. This function outputs an angle degree measurement (absolute value) between
1042 two line segments. The first line segment of the angle was drawn to follow the trajectory of the
1043 internexin^{+} primary dendrite; the endpoint was at the cell body. The second line segment of the
1044 angle was a plumb line to the IPL (i.e. it was drawn to intersect the IPL at ~90˚). As such,
1045 dendrites oriented exactly towards the IPL were assigned an angle of 0˚. At E16 the IPL was
1046 occasionally not present yet; in this case the second line segment was a plumb line to the inner
1047 limiting membrane. In cases where the internexin^{+} dendrite curved, we traced the initial
1048 trajectory of the dendrite as it emerged from the cell body. Dendrites were classified as
1049 projecting 1) towards the IPL; 2) towards the ONBL; or 3) tangentially, according to the angle
1050 scheme delineated in Fig. 2-Supplement 1E. Image stacks were randomly selected for analysis
1051 from a larger library of images; within each selected stack every SAC was traced. *Isl1*^{mG} and
1052 Sox2 were used to confirm the SAC identity of each measured cell, as well as the trajectory of
1053 the internexin^{+} dendrite.

1054 **Characterization of SAC homotypic arbor network in soma layers**

1055 The homotypic nature of SAC soma-layer contacts was investigated by imaging single
1056 *Chat*^{mG}-labeled OFF SACs in mice also carrying a single copy of the *Megf10*^{lacZ} allele (Fig. 2I,J).
1057 Anti-βgal staining was used to reveal the full SAC population, including arbors. *En-face* images
1058 were captured in Z-stacks spanning the INL and IPL; slices corresponding to each layer were
1059 separately Z-projected for display in Fig. 2 and Fig. 2-Supplement 3. To quantify the frequency
1060 of SAC-SAC contacts, we used Z-stacks from P1 tissue to examine the trajectory and
1061 termination site of each dendritic tip in three dimensions. The fraction of *Chat*^{mG}-labeled
1062 dendrites terminating on the βgal-positive soma or arbor of a neighboring SAC was quantified.
1063 To be counted, the putative contact needed to be confirmed in a single Z-stack slice; where
1064 necessary, 3D reconstructions and orthogonal views were used to confirm contact.

1065 We also performed the same analysis on Z-stacks in which one channel had been flipped
1066 about the horizontal and vertical axes. This served as a negative control to measure the frequency
1067 with which GFP and βgal arbors interact by chance, given their density and geometry in the P1
1068 retina. Sample sizes are given in main text and in Fig. 2-Supplement 3.

1069 **Generation and analysis of "solitary" SACs**

1070 *Reduction of SAC density using Ptf1a*^{flox} *mice*

1071 *Ptf1a*^{flox} mutant mice (Krah et al., 2015) were crossed into the *Six3:Cre* background to
1072 generate *Ptf1a*^{cKO} mice. *Six3:Cre* is expressed by retinal progenitors starting at E9.5 in a high-
1073 central-to-low-peripheral gradient (Furuta et al., 2000; Fig. 3A). In central retina, where Cre is
1074 expressed in all progenitors, amacrine cells were completely absent but bipolar cells, RGCs,
1075 Müller glia, and photoreceptors remained (Fig. 3B; Fig. 3-Supplement 1; data not shown). In

1076 peripheral retina, where Cre recombination was incomplete, amacrine cells derived only from
1077 Cre-negative progenitors (Fig. 3C). Because the number of Cre-expressing progenitors in
1078 peripheral retina still vastly exceeded the number that escaped Cre, amacrine cell density in
1079 *Ptf1a*^{cKO} peripheral retina was markedly reduced compared to littermate controls (Fig. 3A,B; Fig.
1080 3-Supplement 1).

1081 *Quantification of dendrite phenotypes in solitary and touching SACs*

1082 To visualize SACs and quantify their arbor targeting frequencies in *Ptf1a*^{cKO} mice, we
1083 bred *Megf10*^{lacZ} into the *Ptf1a*^{flox} background. All *Ptf1a*^{cKO} and littermate control mice in these
1084 experiments carried one copy of the *Megf10*^{lacZ} allele. SAC morphology was revealed with anti-
1085 βgal. Sox2 was used to confirm the SAC identity of all cells included in the experiment. SACs
1086 were scored as "solitary" or "touching" based on whether their dendrites contacted neighboring
1087 SACs in the same or adjacent sections. If this could not be determined (e.g. because the adjacent
1088 section was missing or damaged), the cell was excluded from further analysis. Because SACs
1089 were only present in *Ptf1a*^{cKO} peripheral retina, analysis of littermate control SACs was also
1090 limited to peripheral retina. In *Ptf1a*^{cKO} mice, SACs were more frequently found in the INL than
1091 the GCL and it is possible that the INL SACs were a mixed population of ONs and OFFs.
1092 Therefore, we did not distinguish between SAC subtypes for the analyses.

1093 IPL projections of βgal-stained cells were examined, and cells were assigned to one of
1094 three categories: 1) no arbors projecting to the IPL; 2) Arbors enter the IPL but fail to stratify; 3)
1095 Arbors enter the IPL and ramify in a laminar pattern. Examples of the first category of solitary
1096 SACs are shown in Fig. 3F, left, and Fig. 3-Supplement 1. Examples of the second category are
1097 shown in Fig. 3F, right, and Fig. 3-Supplement 1. The third category is exemplified by all

1098 touching SACs shown (Fig. 3E; Fig. 3-Supplement 1). Each cell in the dataset was also scored
1099 on an independent criterion: whether it projected to the soma layer (e.g. Fig. 3D,F, white arrows).

1100 For each animal in the experiment, the following was calculated and plotted in Fig. 3G:
1101 1) Percentage of SACs with projections to the soma layers; 2) percentage of SACs projecting to
1102 the IPL (i.e., the cells assigned to categories 2 and 3 above); 3) percentage of SACs with
1103 stratified IPL dendrites (i.e. the cells in category 3). Sample sizes: $n = 3$ wild-type littermates
1104 (28, 62, 32 cells analyzed in each animal); $n = 4$ *Ptf1a*^{cKO} animals (11, 35, 13, 12 solitary and 27,
1105 44, 22, 23 touching SACs analyzed in each animal). Statistics: one-way ANOVA with Tukey's
1106 post-hoc test.

1107 **Quantification of SAC projection phenotypes in *Chat*^{mG} mice**

1108 Single SACs labeled in *Chat*^{mG} and *Chat*^{mG}*;Megf10*$^{-/-}$ mice were morphologically
1109 assessed in cross-sections. GFP signal was amplified with anti-GFP antibody staining. All GFP^{+}
1110 SACs on any given slide were imaged and analyzed, to avoid cell selection bias, with the
1111 exceptions of: 1) cells severed by the cryosectioning process; 2) cells with arbors that could not
1112 clearly be distinguished from those of their neighbors; 3) cells in the far retinal periphery, where
1113 sections were oblique to retinal layers, obscuring IPL strata. In experiments analyzing *Megf10*
1114 mutants, littermates were always used as controls to avoid complications arising from the fact
1115 that the precise state of retinal development at the time of birth might vary from litter to litter.

1116 A cell was scored as innervating the IPL if it ramified branched dendrites within the
1117 neuropil. Dendrites that entered the neuropil but did not branch or stratify (e.g. Fig. 6D) were not
1118 sufficient. A cell was scored as projecting to the soma layer if arbors emanating from the cell
1119 soma or primary dendrite terminated or arborized in the INL (for OFF SACs) or GCL (for ON
1120 SACs). The arbor was required to be ~ ≥ 1 cell diameter in length (i.e. small fine arbors were not

1121 counted). One other important exception that was not counted: We observed that many SACs at
1122 young ages had single unbranched arbors extending ~180˚ away from the IPL (e.g. Fig. 2J,K –
1123 all four cells have such arbors, even the ones that do not project towards neighboring SAC
1124 somata). These processes were not counted for two reasons. First, their trajectory was such that
1125 they were unlikely to join the soma-layer dendrite network or contact neighboring somata.
1126 Second, these 180˚ arbors were sometimes still present in P5 SACs (Fig. 2-Supplement 2) and
1127 therefore they did not appear to be subject to the same developmental regulation as tangentially-
1128 directed arbors (Fig. 2L). This observation suggests they are fundamentally different, and likely
1129 serve a different (as yet uncharacterized) purpose. No obvious difference in their frequency was
1130 observed between wild-type and *Megf10* mutants.

1131 To produce graphs in Figs. 2L, 6E, and 8F, the fraction of cells making ectopic
1132 projections – either to the soma layer or to inappropriate IPL sublayers – was calculated for each
1133 genotype and each time point. To determine whether a GFP+ IPL arbor was located in normal or
1134 abnormal IPL strata, *Megf10:*βgal was used as a counterstain. $Chat^{Cre}$ was rarely expressed in
1135 OFF SACs at P0, making it difficult to obtain large sample sizes at this age. For this reason, and
1136 because soma-layer projection frequency did not appear to differ much between P0 and P1, the
1137 data from each time point was pooled for analysis of *Megf10* litters.

1138 Sample sizes for Fig. 2M: P0, n =25 OFF, 63 ON; P1, n = 51 OFF, 79 ON; P2, n = 46
1139 OFF, 55 ON; P3, n = 33 OFF, 49 ON; P5, n = 15 OFF, 26 ON; P7, n = 23 OFF, 34 ON. Data
1140 were from four litters of mice, each of which was assessed at no less than two of these time
1141 points.

1142 Sample sizes for *Megf10;* $Chat^{mG}$ experiments (Figs. 5F, 7G): <u>*Megf10* heterozygous</u>
1143 <u>littermate controls</u>: P0/1, n = 11 OFF, 25 ON; P2, n = 25 OFF, 23 ON; P3, n = 17 OFF, 22, ON;

1144 P5, n = 16 OFF, 16 ON. *Megf10* mutants: P0/1, n = 6 OFF, 25 ON; P2, n = 14 OFF, 20 ON; P3,
1145 n = 34 OFF, 41 ON; P5, n = 48 OFF, 54 ON. Data were from two litters of mice.

1146 For the adult data reported in Fig. 8F, a different procedure was used; see "Quantification
1147 of Mosaic Spacing Phenotypes" section below.

1148 **Analysis of *Chat-Megf10^{cKO}* conditional mutants**

1149 *Characterization of timing of MEGF10 deletion*

1150 For initial characterization of when MEGF10 protein is eliminated by the *Chat^{Cre}* driver
1151 line, the following experiment was performed: *Chat^{Cre}; Megf10^{flox}* mice were intercrossed with
1152 *Chat^{Cre}; Megf10^{lacZ}* carriers to generate *Chat^{Cre}; Megf10$^{flox/lacZ}$* (*Chat-Megf10^{cKO}*) experimental
1153 animals and littermate controls (*Chat^{Cre}; Megf10$^{flox/+}$*). These animals also carried a *Rosa26*
1154 mGFP Cre reporter allele. Animals were sacrificed at P1, P3, and P5; retinas were cross-
1155 sectioned and immunostained for anti-MEGF10 (Fig. 6-Supplement 1). Comparisons were made
1156 across animals from the same litter to assess how MEGF10 immunoreactivity changed over time.
1157 Two litters were analyzed in this way, each yielding the same conclusion: MEGF10
1158 immunoreactivity was largely eliminated by P5 in *Chat-Megf10^{cKO}* mice (Fig. 6-Supplement 1).
1159 At P3, overall MEGF10 levels were reduced, but most SACs still expressed detectable protein
1160 (Fig. 6-Supplement 1). The cells that lost MEGF10 immunoreactivity by P3 were not necessarily
1161 the same cells that recombined the mGFP reporter at the *Rosa26* locus (Fig. 6F,G). At P1, only a
1162 very small number of cells (< 5 per retina) could be identified that lacked MEGF10
1163 immunoreactivity; most of these were ON SACs although a few recombined OFF SACs were
1164 identified (Fig. 6G). We conclude that a small fraction of SACs loses MEGF10 protein prior to

1165 P3, while the majority lose MEGF10 between P3 and P5. Further, ON SACs are somewhat more
1166 likely to lose MEGF10 before P3 than OFF SACs.

1167 *Assessment of morphological and IPL projection phenotypes*

1168 To ask if loss of MEGF10 prior to P3 affects dendritic targeting, *Chat*^{mG}-labeled single
1169 SACs were identified in retinal cross-sections from *Chat-Megf10*^{cKO} and *Chat*^{Cre}*; Megf10*$^{flox/+}$
1170 control mice, as described above. Analysis was performed at P1 and P3; data in Fig. 6H is from
1171 P3 only. All mGFP^{+} SACs were first scored as to whether they expressed MEGF10 protein (see
1172 Fig. 6F,G). Subsequently, each cell was scored for soma-layer projection as described above for
1173 wild-type and *Megf10*$^{-/-}$ animals. This scoring was done blind to the cell's MEGF10 expression
1174 status. The fraction of cells classified as either "soma-projecting" or "IPL-only" was calculated
1175 for MEGF10^{+} SACs, MEGF10^{-} SACs, and littermate control SACs (Fig. 6H). Sample sizes: n =
1176 26 OFF, 18 ON cells from controls; 24 OFF, 19 ON MEGF10^{+} cells from *Chat-Megf10*^{cKO}; 9
1177 OFF, 17 ON MEGF10^{-} cells from *Chat-Megf10*^{cKO}.

1178 To assess SAC stratification at maturity, cross-sections from P17 *Chat-Megf10*^{cKO} and
1179 littermate controls were stained for anti-ChAT. Four mutants and three littermate controls, from
1180 two litters, were examined.

1181 **Analysis of *Six3-Megf10*^{cKO} conditional mutants**

1182 *Characterization of Cre recombination patterns*

1183 Breeders carrying the relevant alleles were interbred to generate *Six3:Cre; Megf10*$^{flox/lacZ}$
1184 (*Six3-Megf10*^{cKO}) mice and littermate controls (*Six3:Cre; Megf10*$^{+/lacZ}$ or *Cre*$^{-}$ *Megf10*$^{flox/lacZ}$). As
1185 noted above in *Ptf1a* section, Cre is expressed very early (~E9.5) in *Six3:Cre* retina, but
1186 expression is incomplete, with some parts of peripheral retina spared from Cre activity (Furuta et

1187 al., 2000). Therefore, all mice used for these experiments also carried the *Rosa26*^{GFPf} Cre
1188 reporter, to reveal retinal regions that either lacked MEGF10 (GFP^{+} cells) or were spared from
1189 MEGF10 deletion (GFP^{-} cells). Anti-MEGF10 staining confirmed that the GFP Cre reporter is a
1190 reliable marker of MEGF10 expression status (Fig. 6-Supplement 1).

1191 *Assessment of morphological phenotypes*

1192 For quantification of INL projection frequency at P2, *Six3-Megf10*^{cKO} and littermate
1193 control whole-mount retinas were stained for βgal, Sox2, and anti-GFP. This staining marked
1194 SACs (Sox2 and βgal), revealed their dendritic morphology (βgal), and defined their MEGF10
1195 expression status (GFP). Confocal stacks were acquired through the INL, extending to the IPL
1196 (which was clearly discernable due to dense βgal and GFP expression). The INL was defined as
1197 the region above this in the image stack, containing Sox2^{+} neurons. Cells that projected into the
1198 INL were clearly discernable due to their multipolar morphology with numerous dendritic
1199 protrusions (e.g. Fig. 7B). Cells that did not project to the INL had a round morphology with
1200 only minor lateral branches less than one cell radius in length (Fig. 7C). Each βgal-labeled SAC
1201 was scored as to whether it expressed GFP, and whether it projected lateral arbors into the INL.
1202 If the cell had only INL branches directed towards the IPL through the stack Z-plane, it was not
1203 counted as INL-projecting. Scoring was done in separate sessions so that the scorer was blind to
1204 GFP expression status when determining INL projections. Sample sizes: n = 117 SACs from 2
1205 control mice; n = 302 GFP^{+} SACs and 149 GFP– SACs from 2 *Six3-Megf10*^{cKO} mice.

1206 To assess SAC stratification in cross-sections, P2, P4, or P17 *Six3-Megf10*^{cKO} and
1207 littermate control retinas were sectioned and stained for anti-βgal (P2) or anti-ChAT (P17). The

1208 number of animals examined was: P2, 4 mutants, 2 controls; P4, 2 mutants, 3 controls; P17, 2
1209 mutants, 2 controls.

1210 **Quantification of area covered by SAC dendritic arbors**

1211 *Neonatal individual SAC arbor territory*

1212 P0 *Chat*^{mG} retinas were imaged in whole-mount preparations stained with anti-Sox2 and
1213 anti-GFP antibodies to identify single GFP^{+} SACs. To avoid cell selection biases, all labeled
1214 SACs with arbors that were clearly distinguishable from their neighbors were imaged and
1215 analyzed, except for far-peripheral cells that may have been damaged during mounting. At least
1216 4 animals were imaged for each genotype. Z stacks were acquired through the GCL, IPL, and
1217 INL to encompass all arbors of a single cell. Images were imported into ImageJ, z-projected into
1218 a single plane, and polygons were drawn connecting the dendritic tips, nearest neighbor to
1219 nearest neighbor, until the dendritic field was captured. Area of this polygon was calculated
1220 using ImageJ. Sample sizes: OFF SACs, n = 16 wild-type and 16 *Megf10*$^{-/-}$; ON SACs, n = 31
1221 wild-type and 34 *Megf10*$^{-/-}$. Statistics: two-tailed t-tests.

1222 *Adult individual SAC arbor territory*

1223 Individual SACs were labeled by injection of *Chat*^{Cre} mice with "Brainbow" Adeno-
1224 associated virus (AAV) driving fluorophore expression in a Cre-dependent manner (Cai et al.,
1225 2013). The two Brainbow AAV9 viruses, encoding farnesylated fluorescent proteins that are
1226 targeted to the plasma membrane (University of Pennsylvania Vector Core), were mixed to 1.5 x
1227 10^{12} genome copies per mL. Adult mice (P40-50) were anesthetized with ketamine-xylazine by
1228 intraperitoneal injection. Propraracaine hydrochloride (0.5%) ophthalmic solution (Akorn, Lake
1229 Forest, IL) was applied to the eye to provide local anesthesia. A 30 1/2G needle was used to

1230 make a small opening near the ora serrata, and 1µl of virus was injected with a 33G blunt-ended
1231 Hamilton syringe intravitreally. Tissue was collected 3 weeks after the virus injection.

1232 Retinas were stained in whole-mount with anti-GFP, anti-mCherry, and anti-mKate
1233 antibodies to reveal SACs. OFF SACs were not labeled in large numbers, so analysis was
1234 restricted to more abundantly labeled ON SACs. Imaging, image processing, and quantification
1235 were as for P0, except that only SACs in central and mid-peripheral retina were used to avoid
1236 confounding effects of eccentricity on arbor size. Sample sizes: n = 10 wild-type and 16 *Megf10*
1237 mutant SACs.

1238 *ChAT+ arbor plexus retinal coverage*

1239 *En-face* images of adult (P46) ON or OFF SAC plexus were obtained from confocal Z-
1240 stacks (0.4 µm Z resolution) by performing maximum-intensity Z-projections of 2-4 optical
1241 slices encompassing the relevant layer. Using ImageJ, these images were then thresholded,
1242 converted to binary, and the percentage of the field of view covered by ChAT-positive arbors
1243 was calculated. All image stacks were obtained from central or mid-peripheral retina. Sample
1244 size: 9 fields of view from 2 *Megf10* mutants and 2 heterozygous littermate controls were used to
1245 calculate average coverage for each genotype. Percent change is reported in the Results; total
1246 retinal coverage was as follows: Control ON, 65.9 ± 1.3 %; control OFF, 70.6 ± 3.6%; mutant
1247 ON 56.9 ± 3.8%; mutant OFF, 60.0 ± 3.7% (mean ± S.D).

1248 ***Hb9-GFP* stratification**

1249 P1-P2 retinas carrying *Megf10*^{lacZ} and *Hb9-GFP* were co-stained for βgal and GFP.
1250 RGCs with dendrites that co-fasciculated with βgal-positive IPL strata were counted. Cells that
1251 projected to βgal-positive regions, but also filled non-SAC-projecting IPL regions, were not

1252 counted as co-fasciculated. To judge co-fasciculation, we used 2 criteria: 1) inspection of
1253 dendrite anatomy across the confocal stack; 2) fluorescence profiles of GFP and βgal channels
1254 across IPL (see next section below). Examples of cells falling into each category are provided in
1255 Fig. 1 and Fig. 1-Supplement 2. See Results for sample sizes.

1256 **Quantitative assessment of IPL stratification level**

1257 Images of retinal cross sections were processed in ImageJ. A vertical ROI (12.5 μm
1258 wide) was drawn to perpendicularly bisect the IPL strata, from the edge of the INL to the edge of
1259 the GCL. IPL stratification levels were reported as percentage of IPL width. Intensity was
1260 calculated for each pixel along the length of the ROI as an average across its width. Background
1261 (minimum pixel value) was subtracted; then, all pixel intensity values were normalized to the
1262 maximum value of that ROI. Location of fluorescent peaks was calculated as the pixel with
1263 maximum intensity; if multiple pixels had the same intensity the peak was defined as the center
1264 of the plateau. The procedure was typically performed on single confocal optical sections, but for
1265 some P1-2 cells, which have much smaller arbors, it was necessary to use a maximum-intensity
1266 projection of a small number of slices in order to fully capture dendrite morphology.

1267 For BC5-BC7 arbor distance measurements (Fig. 9F), distances as percentage of total IPL
1268 width were compared by one-way ANOVA/Tukey's post-hoc test. n = 14 measurements from 2
1269 control mice; n = 7 normal IPLs, 11 SAC clumps, 11 SAC gaps from 3 *Megf10*$^{-/-}$ mice.

1270 **Generation of Megf10-ΔICD Constructs**

1271 The MEGF10-ΔICD-GFP construct was reported previously (Kay et al., 2012), which
1272 was originally made from pUbC-MEGF10-GFP (Addgene #40207). It encodes a version of
1273 MEGF10 in which the cytoplasmic domain is truncated after the 9th amino acid and replaced by

1274 GFP. Inclusion of those 9 amino acids was necessary to achieve plasma membrane localization.
1275 For this study it was subcloned into the pEGFPN3 plasmid, containing the CMV promoter, to
1276 make pCMV-MEGF10-ΔICD-GFP.

1277 To make the MEGF10-ΔICD-Flag construct, Megf10 (truncated after the 9th intracellular
1278 domain amino acid as above) was PCR amplified from pUbC-MEGF10-GFP vector using
1279 M10flag_Fwd forward primer and Cyto9_flag_Rev1 reverse primer. Resulting PCR products
1280 were digested with NotI and AscI restriction enzymes and ligation cloned into pEGFPN3 vector
1281 linearized with corresponding restriction enzymes.

1282 **Assay for interaction of MEGF10-ΔICD constructs**

1283 *Co-Immunoprecipitation*

1284 HEK293T cells were grown to 80% confluency. Cells were then transfected using a
1285 linear polyethylenimine (PEI) transfection reagent: DNA, PEI, and Opti-MEM were mixed in a
1286 1:3:30 ratio and incubated for 10 minutes at room temperature then applied to confluent cells.
1287 Cells were harvested 48-hour post transfection. Cells were lysed with NP-40 lysis buffer (1%
1288 NP-40, 150mM NaCl, 50mM Tris-Cl, and 1X proteinase inhibitor) by pipetting. Lysate was
1289 centrifuged at 14000 x g at 4ºC for 15 min. to remove insoluble material. The soluble protein
1290 fraction was quantified with Bio-Rad DC assay. For immunoprecipitation, 500µl (1µg/ µl)
1291 protein in NP-40 buffer lysis buffer was incubated overnight at 4ºC with antibody (1µl of
1292 chicken anti-GFP or 2µl of mouse anti-Flag). Protein G Dynabeads (10µl) were added to mixture
1293 for 1 hour at 4ºC while rotating. Beads were sequestered by magnet and flow-through was
1294 removed. Beads were washed with 500µl lysis buffer (3x) on ice then eluted with 30µl 2X
1295 Laemmli containing 5% β-mercaptoethanol.

1296 *Western Blot*

1297 Samples were prepared in 2X Laemmli sample buffer, heated at 95°C for 10 minutes, and
1298 loaded onto SDS-acrylamide gel (running gel: 8% acrylamide/bis Tris-HCl with 0.1% SDS pH
1299 8.8; stacking gel: 5% acrylamide pH 6.8; cross linked with TEMED and APS). Precision Plus
1300 Protein Dual Color Standards (BioRad) were used as a molecular weight marker. The gel was
1301 run on a BioRad mini gel running apparatus with SDS-PAGE running buffer (25 mM Tris, 192
1302 mM glycine, 0.1% SDS). Electrophoresis was carried out at 50 V through the stacking gel then
1303 adjusted to 120 V until the dye front reached the lower end of the gel. BioRad Immobilon-FL
1304 PVDF membrane and Whatman filter paper were used with the BioRad mini cassette for transfer.
1305 Samples were transferred in 25 mM Tris, 192 mM glycine, 20% methanol at 100 V for 90
1306 minutes. Membranes were blocked with PBS/Odyssey blocking buffer and stained with chicken
1307 anti-GFP 1:20000, mouse anti FLAG 1:20000 overnight at 4°C with shaking. After washing with
1308 PBST for 4 times, membranes were stained with 1:20000 secondary antibodies for one hour at
1309 room temperature. The membranes were washed with PBST four times and then rinsed with PBS
1310 and water. Finally, the membranes were imaged with LI-COR Odyssey using the Image Studio
1311 software.

1312 **Quantification of mosaic spacing phenotypes and their effects on SAC IPL projections**

1313 *Regularity index*

1314 Regularity of SAC cell body distribution in *Six3-Megf10*^{cKO}, *Chat-Megf10*^{cKO}, and
1315 littermate control mice was calculated as previously described (Kay et al., 2012). The Voronoi
1316 domain regularity index (VDRI) was used as a measure of regularity. It is calculated by first
1317 assigning a Voronoi domain to each cell in an array (Fig. 9-Supplement 1), and then calculating

1318 the mean and standard deviation of the domain areas. The VDRI is defined as the mean area
1319 divided by the standard deviation. Arrays that are less regularly distributed will have a lower
1320 VDRI because their domain sizes are more variable (and hence have a higher standard deviation).

1321 P17 whole-mount retinas were stained with an antibody to ChAT and imaged *en face*.
1322 One eye was processed from each animal used in the experiment. For each eye, 3 confocal image
1323 stacks were obtained using a 20x objective (636.5 μm^2 field of view). Images of INL SACs were
1324 analyzed using Fiji software. The location of each SAC in the field of view was marked; this
1325 information was used to count the number of SACs (Fig. 9B) as well as define Voronoi domains
1326 belonging to each cell, using Fiji functions. The area of each Voronoi domain (excluding edges)
1327 was calculated in Fiji.

1328 For statistical analysis of regularity effects across genotypes, we first calculated the per-
1329 animal average cell density and VDRI from the 3 acquired images. Differences between
1330 genotypes were then evaluated using one-way ANOVA and Fisher's PLSD. Previously
1331 published *Megf10* null and simulation data was also included for comparison (Kay et al., 2012).
1332 The simulations define the VDRI that would be expected for a randomly-arranged array of cells
1333 matched in size and density to real SACs. Data collection and analysis was virtually the same as
1334 in the previous study, allowing us to include these data in our statistical comparisons.

1335 *Effects of soma position upon IPL errors: Single-cell analysis*

1336 To ask if soma position correlates with IPL errors, we first defined the ectopic projection
1337 status of each OFF SAC in a set of Z-stacks acquired from ChAT-immunostained retinal whole-
1338 mounts. Sample sizes: n = 515 cells from 2 control (*Megf10*$^{+/-}$) mice; n = 584 cells from 2
1339 *Megf10* mutant mice. The Z-stacks encompassed, at different levels of the stack, SAC somata in
1340 the INL and their ramified arbors in the IPL. In *Megf10* mutants, the OFF ectopic IPL arbor

1341 network and the typical OFF DS circuit sublayer were identified at different stack levels (Fig.
1342 8C,E). ChAT$^+$ arbors arising from individual OFF SAC somata were traced through the stack to
1343 identify those that joined into the ectopic network. The fraction of SACs that did so was then
1344 calculated and plotted in Fig. 8F. For Fig. 8G, we further examined these stacks to look for SACs
1345 that made ectopic projections at the INL level.

1346 Next, we defined the severity of mosaic spacing perturbations in the local neighborhood
1347 of each SAC. Because SAC position is random in *Megf10* mutants, SACs might be more
1348 crowded or more isolated from their neighbors than in controls; or, by chance, they might be
1349 located at a fairly normal distance from their neighbors. The size of a cell's Voronoi domain is
1350 influenced by the distance of all nearest neighbors (Fig. 9-Supplement 1), and therefore serves as
1351 a convenient measure of local cell density. For simplicity we refer to Voronoi domains as
1352 "territory size" in Fig. 9-Supplement 1. The effect of local cell density upon IPL projection
1353 errors was determined by plotting the ectopic error rate for each 100 μm^2 territory size bin (Fig.
1354 8D,F). Sample size per bin, in order from smallest (<200 μm^2) to largest (>1100 μm^2): n = 32,
1355 65, 89, 102, 91, 80, 30, 39, 24, 34.

1356 **Multielectrode array recordings**

1357 *Isolation of retina, recording, and spike sorting*

1358 Two wild-type and two *Megf10*$^{-/-}$ animals were used for multielectrode array (MEA)
1359 recordings. Immediately following euthanasia, retinas were isolated under infrared (IR, >900
1360 nm) illumination with the assistance of IR-to-visual converters. This preserved the
1361 photosensitivity of the retina during the dissection. Dissections were performed in sodium
1362 bicarbonate-buffered Ames' solution (Sigma, St. Louis, MO) equilibrated with 5% CO_2 + 95%

1363 O_2 to pH 7.4 and maintained at 32-34° C. Hemisection of the eye was performed along the ora
1364 serrata by first making a small incision, following which the vitreous was removed and the retina
1365 was isolated from the pigment epithelium and eye cup. A piece of dorsal retina (1-2 mm^2) was
1366 dissected and placed RGC-side down on the planar MEA.

1367 The MEA consisted of 519 electrodes with 30 μm inter-electrode spacing, covering a
1368 hexagonal region with 450 μm on a side (Field et al., 2010). The voltage on each electrode was
1369 digitized at 20 kHz and stored for post-hoc analysis. Details of recording methods and spike
1370 sorting have been described previously (Field et al., 2007). Spikes were identified using a
1371 threshold of four times the voltage standard deviation on each electrode. Principal component
1372 analysis applied to the ensemble of spike waveforms measured on each electrode provided a
1373 subspace for clustering spikes according to their shape. A Gaussian mixture model was used to
1374 cluster the spikes originating from individual RGCs. The clusters were manually inspected for
1375 each identified ooDSGC to ensure the spike waveforms were well isolated from other
1376 simultaneously recorded RGCs and all spikes were captured within each cluster. When a single
1377 cluster of spikes was captured by more than one Gaussian or when a single Gaussian included
1378 spikes from more than one cluster, the clustering was manually adjusted to generate a new set of
1379 initial conditions for re-fitting the mixture of Gaussians. Spike clusters with >10% estimated
1380 contamination based on refractory period violations, or spike rates <1 Hz, were excluded from
1381 further analysis.

1382 *Visual stimulation and RGC responses*

1383 Visual stimuli were focused on the photoreceptor outer segment, from an OLED display
1384 (Emagin, Inc.) with 60.35 Hz refresh rate. The mean intensity of the stimulus was 7000

1385 photoisomerizations per rod per s, or 5000 photoisomerizations per cone per s for a cone
1386 containing all M-opsin. These estimates do not account for the effect of pigment self-screening.
1387 To measure the direction tuning of ooDSGCs as a function of contrast, a positive contrast bar
1388 (1200 μm wide) was presented on a gray background (Fig. 10B). On each presentation, the bar
1389 moved in one of twelve equally spaced directions at 400 μm/sec and was presented at one of the
1390 following (Weber) contrasts: 5%, 10%, 20%, 40%, 80%, 150% and 300%. Responses to a total
1391 of 8 trials were collected for every condition; stimulus conditions were presented pseudo
1392 randomly. Spike times were binned at 1 ms resolution for all subsequent analyses.

1393 To distinguish DSGCs from other RGCs recorded on the MEA, square-wave drifting
1394 gratings were used. These gratings drifted in one of twelve different and equally spaced
1395 directions and at two different speeds (225 μm/sec and 900 μm/sec; spatial period 400μm/cycle).
1396 DSGCs were identified based on their direction selectivity index (DSI) defined as:

$$DSI = \frac{|\sum \vec{v}_i|}{\sum n_i}$$

1397 calculated from responses to drifting gratings and moving bars. Here, n_i is the number of spikes
1398 elicited to stimulus movement along the direction i defined by the vector $\vec{v}_i$.

1399 The distribution of DSIs across all recorded RGCs was bimodal, with DSGCs forming
1400 the high mode (Fig. 10A). Based on these distributions, a DSI of 0.25 reliably identified DSGCs
1401 in wild-type and *Megf10*$^{-/-}$ retinas. ooDSGCs were isolated from ON DSGCs by their distinct
1402 ON and OFF responses to a bar entering and exiting the receptive field (Fig. 10B). The total
1403 ooDSGC sample size obtained by this procedure was n = 80 from the two wild-type and n = 74
1404 from the two *Megf10*$^{-/-}$ retinas. The paired Kolmogorov-Smirnov (KS) test was used to compare
1405 cumulative probability distributions from these two populations.

Analysis of ooDSGC response

Measurement of direction tuning width

First, the direction tuning curve for each ooDSGC was obtained by calculating the number of spikes elicited across all trials for each direction of bar movement. Due to the circular nature of the data, the direction tuning curve was treated as circular normal distribution, also called von Mises distribution (Oesch et al., 2005), and the tuning width was measured as the circular standard deviation (σ_{circ}), defined by

$$\sigma_{circ} = \sqrt{-2\ln(R)}$$

where R is the second moment of the von Mises distribution:

$$f(\theta, \mu) = \frac{1}{2\pi I_0(\kappa)} e^{\kappa \cos(\theta - \mu)}$$

This yielded a nonparametric estimate of the tuning curve width.

Measurement of direction tuning strength

To measure the strength of tuning, the difference between spike counts to motion in the preferred and null directions was normalized by the sum of these responses. The tuning curves were sampled at 30 degree intervals. To estimate the response in the preferred (null) direction, which could fall between sampled directions, a cosine-weighted average of the two strongest

(weakest) responses was calculated. This yielded the following equation for measuring tuning strength:

$$\text{Tuning strength} = \frac{\sum_{i=1}^{2} r_i \cos(|\theta_{PD}-\theta_i|) - \sum_{j=1}^{2} r_j \cos(|\theta_{ND}-\theta_j|)}{\sum_{i=1}^{2} r_i \cos(|\theta_{PD}-\theta_i|) + \sum_{j=1}^{2} r_j \cos(|\theta_{ND}-\theta_j|)}$$

where the summation $\sum_{i=1}^{2}$ is performed over the responses r_i weighted by the cosine terms for the two nearest neighbor movement directions θ_i around the preferred direction θ_{PD} and the null direction θ_{ND}. This resulting index for tuning strength varied between zero and unity.

Measurement of direction tuning similarity between ON and OFF responses

To separately analyze the ON and OFF responses of ooDSGCs, we first defined temporal windows for each ooDSGC that distinctly separate the ON and OFF responses. This was done by passing high-contrast moving bars (150% and 300% contrast) through the receptive field. In the resulting spike rasters, ON and OFF response phases were clearly discernible (Fig. 10B,F). The boundary for separating the ON and OFF responses was set halfway between the peak ON and OFF spike rate locations (Fig. 10F,G). Once the temporal boundary was defined, the preferred direction was calculated independently for the ON and OFF responses for each ooDSGC. The same ON-OFF temporal boundaries were used for all contrasts shown in Fig. 10-Supplement 1. The difference between the preferred directions, $\Delta\phi$, quantified the angular difference between the ON and OFF preferred directions (Fig. 10F).

Analysis of ooDSGC subtypes

ooDSGC subtype classification was performed using the K-means clustering algorithm. This was done by first assigning a set of four initial seed values corresponding to the four

1445 cardinal directions of ooDSGCs (Oyster and Barlow, 1967). Next, the angular difference
1446 between the seed values (for first iteration) or the cluster means (for later iterations), and the
1447 preferred directions of each ooDSGCs was calculated. The cluster for which the angular
1448 difference was minimum was the cluster to which an ooDSGC was assigned. This yielded the
1449 four subpopulations of ooDSGCs described in Fig. 10-Supplement 1.

1450 **QUANTIFICATION AND STATISTICAL ANALYSIS**

1451 Statistical analysis was performed using GraphPad Prism software
1452 (anatomy/development studies) or using custom JAVA based software and MATLAB software
1453 (physiology studies). Statistical tests used for each experiment are given in the METHOD
1454 DETAILS section above, and/or in the figure legends. Sample sizes for each experiment are
1455 given in the METHOD DETAILS section above or else in the Results. *P*-values ($\alpha = 0.05$) are
1456 given in figure legends, or in the Results if no figure is shown. Error bars are defined in figure
1457 legends. Exact *p*-values are reported unless the value was less than 1.0×10^{-7}.

Figure 1

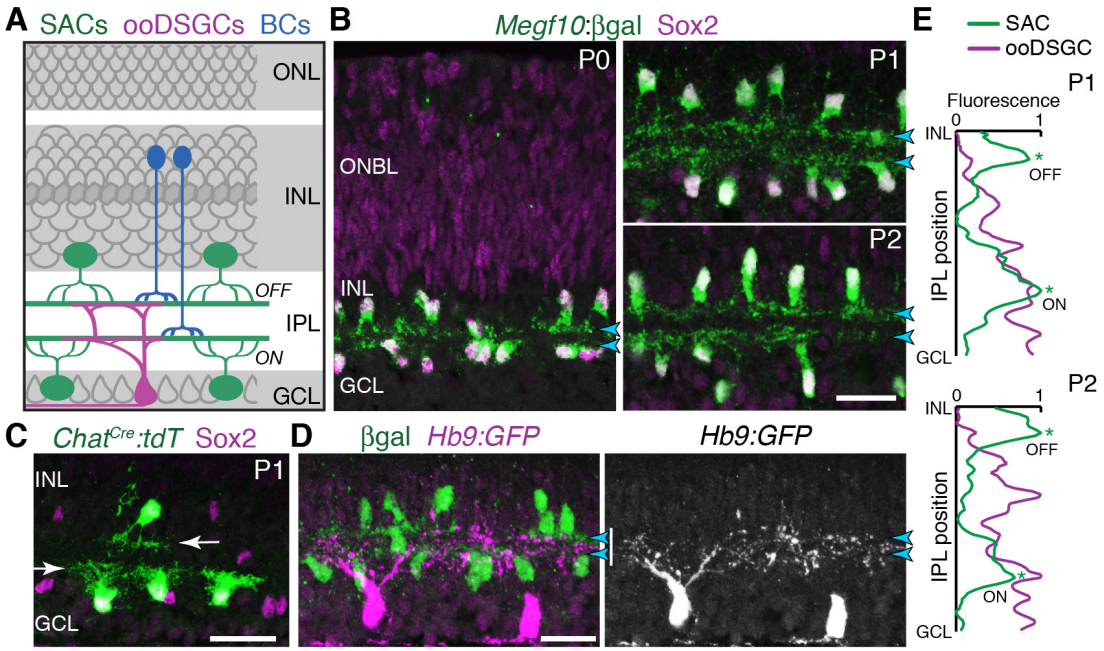

Figure 1: Initial formation of DS circuit IPL sublayers.

A: Schematic of mature direction-selective (DS) circuit and its cell types, depicted in cross-section. SACs (green) and bipolar cells (blue) project to one of two IPL sublayers (*OFF, ON*). OFF SACs reside in inner nuclear layer (INL); ON SACs reside in ganglion cell layer (GCL). ooDSGCs (purple) send dendrites to both DS circuit sublayers. ONL, outer nuclear layer.

B: SAC IPL sublayer formation assessed in *Megf10*^{lacZ} mice. All SACs are double-positive for anti-Sox2 (purple) and anti-βgal (green). Progenitors in outer neuroblast layer (ONBL) also express Sox2. SAC IPL sublayers (arrowheads) begin to appear by P0, and are fully apparent by P1.

C: Sparse labeling of neonatal SACs in *Chat*^{Cre} mice. Individual SACs have laminar-specific projections by P1 (arrows). tdT, tdTomato.

D,E: ooDSGCs (labeled by *Hb9:GFP*) project diffusely in the IPL at P1-P2, whereas SAC arbors are stratified (arrowheads). D: retinal cross-sections. Vertical white bar denotes IPL width. E: Fluorescence intensity plots of SAC and ooDSGC dendrite staining across IPL, from representative images (P2 image in D; P1 image in Fig.1-Supplement 2). ON and OFF strata (asterisks) are clear for SACs but not for ooDSGC dendrites.

Scale bars: 25 μm.

Figure 2

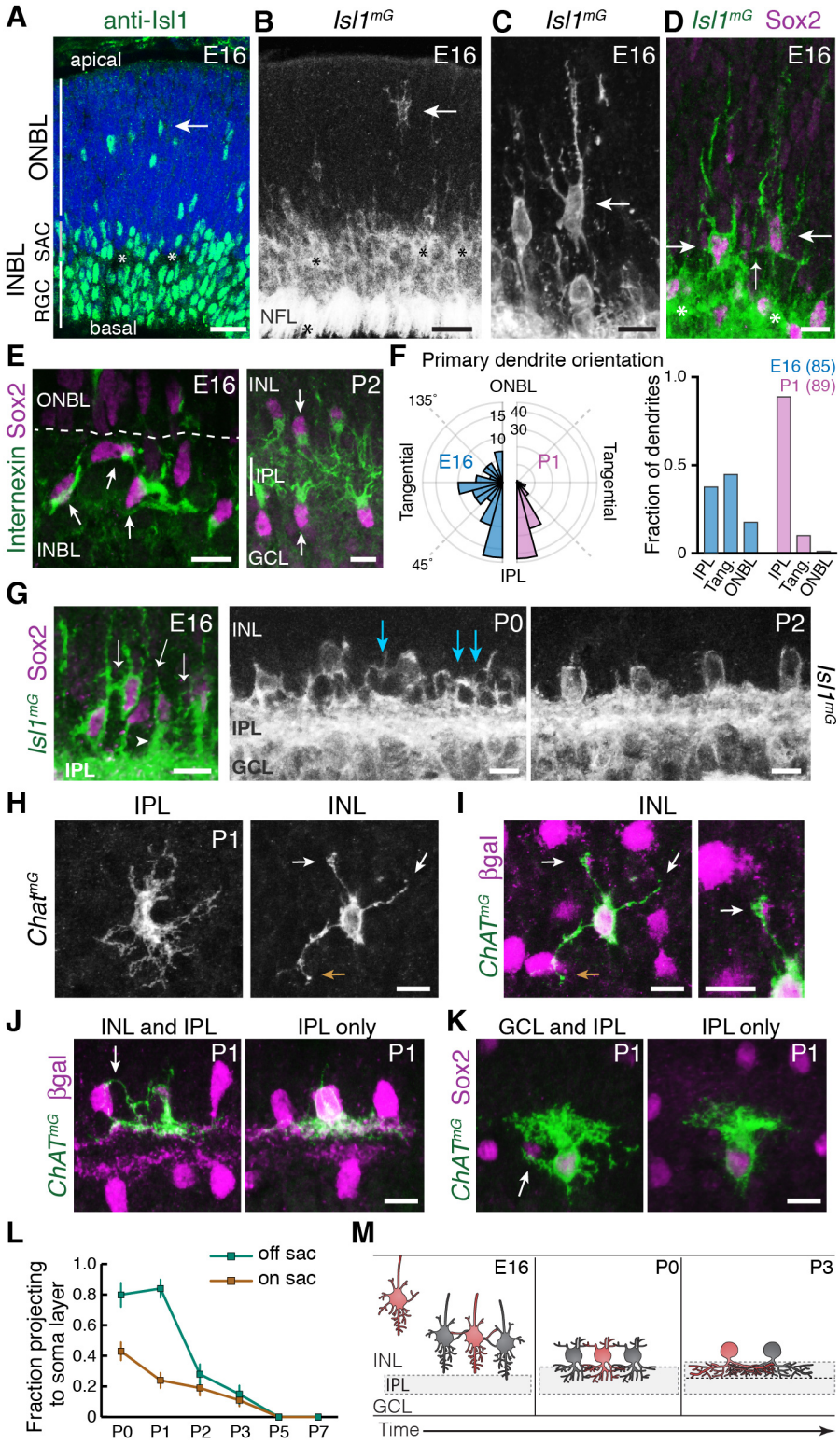

Figure 2: Newborn SACs contact each other via a network of soma layer arbors.

A,B: Isl1 labels SACs and RGCs in embryonic retina. A, immunostaining; B, mGFP driven by *Isl1*^{Cre} (*Isl1*^{mG}). Arrows, newborn SACs migrating apico-basally through ONBL. INBL SACs and RGCs predominantly reside in indicated regions. IPL neuropil (asterisks) exists in discontinuous patches at this age. NFL, nerve fiber layer containing RGC axons. Blue, nuclear counterstain.

B,C: Migrating SACs in ONBL (arrows) have multipolar morphology. They are far from other SACs and do not contact them.

D: Morphology of Sox2^{+}Isl1^{+} SACs (large arrows) upon arrival at INBL. SACs contact each other outside the IPL (small arrow, connecting arbor). Their migratory morphology and distance from IPL (asterisks) indicate they have not yet innervated IPL (also see Fig. 2-Supplement 2).

E: Internexin immunostaining reveals polarization of SAC primary dendrites. SACs project towards IPL at P2. E16 INBL SACs often project tangentially within INBL, towards neighboring SAC somata (arrows).

F: Quantification of primary dendrite orientation. Left, polar histogram (raw counts) of primary dendrite angles (absolute values). 0˚ was defined as perpendicular towards IPL. Note that E16 and P1 are displayed on different scales; each plot is scaled to size of largest bin, aiding legibility in E16 plot where bin sizes are more evenly distributed. Right, fraction of dendrites oriented towards IPL, ONBL, or tangential quadrants of the polar plot (denoted by dashed lines, labels). Sample size of scored dendrites is indicated.

G: A network of arbors (arrows) connects somata of INBL SACs at E16. The network remains prominent in INL at P0 but is mostly gone by P2. Arrowhead, IPL-directed projection.

H,I: An individual P1 OFF SAC labeled by *Chat*^{mG}, imaged *en face* to show its arbor morphology at IPL and INL levels. Full SAC population is revealed using *Megf10*:βgal. INL arbors (I) make selective contacts with SAC neighbors (purple): GFP^{+} arbor tips terminate on SAC somata (orange arrow) or SAC arbors (white arrows). Right panel (I): Higher magnification view of touching arbors. Images are Z-projections of confocal stacks encompassing each arbor's volume (H, 2.0 µm; I, 3.5 µm). Projections are shown for illustration but all contacts were verified across stack volume – see Fig. 2-Supplement 3 for details.

J,K: Individual P1 OFF (K) and ON (L) SACs labeled by *Chat*^{mG} (green) in cross-section. Purple, full SAC population. Some SACs are bi-laminar with arbors that contact neighboring somata (arrows, left panels); others project only to IPL (right panels).

L: Frequency of soma layer projections across development, determined from single *Chat*^{mG} cells as in J,K. Error bars, standard error. Sample sizes, see Methods.

M: Schematic of newborn SAC morphology based on B-L. Soma-layer homotypic contacts are established upon completion of migration, and are mostly eliminated by P3.

Scale bars: 25 µm (A,B); 10 µm (all others).

Figure 3

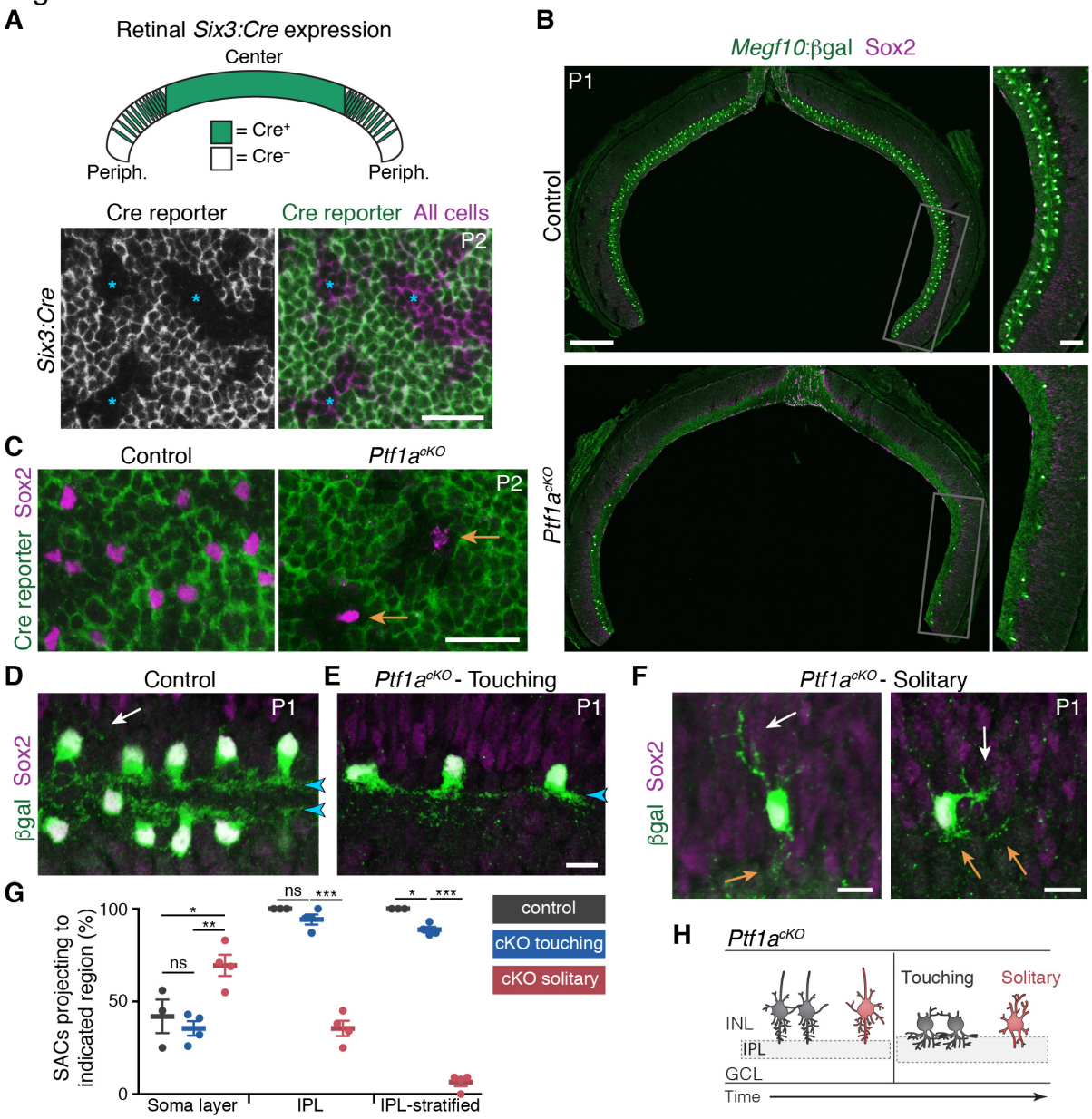

Figure 3: SAC homotypic contact is required for IPL sublayer formation.

A: Top: Schematic illustrating *Six3:Cre* expression pattern in retinal cross-section. Bottom: *En-face* view of *Six3:Cre* recombination in peripheral retina, revealed using GFP Cre reporter. Asterisks, Cre$^-$ regions.

B. Reduced SAC density in *Ptf1a*^{cKO} retina. SACs (labeled by Sox2 and *Megf10*^{lacZ}) are completely eliminated from *Ptf1a*^{cKO} central retina; some remain in peripheral retina (boxed regions, right panels). Top, littermate control (*Ptf1a*$^{+/+}$).

C: *En-face* view of SACs in peripheral retina of *Ptf1a*^{cKO} and littermate control. Green, GFP Cre reporter. Control SACs were either Cre$^+$ or Cre$^-$. Mutant SACs were Cre$^-$ (arrows), indicating that they derive only from cell lineages that maintain *Ptf1a* function.

D-F: SAC IPL laminar targeting in *Ptf1a*^{cKO} (E,F) and littermate control (D). *Ptf1a*^{cKO} SACs close enough to touch (E) form IPL strata (blue arrowheads), similar to control SACs (D). Solitary SACs (F) are not polarized towards IPL; they have extensive INL-directed arbors (white arrows) and rudimentary IPL-directed arbors (orange arrows). Some solitary SACs entirely fail to innervate IPL (F, left cell) and resemble migrating E16 SACs (Fig. 2B,C); others innervate IPL with minimally-branched, non-stratified arbors (F, right cell).

G: Quantification of SAC dendrite phenotypes at P1-2. Left, frequency of soma layer innervation. *p = 0.0350; **p = 0.0081; ns, p = 0.7516. Center, frequency of IPL innervation failure (e.g. F, left). ***$p = 4.0 \times 10^{-7}$; ns, p = 0.3723. Right, frequency of cells that send arbors into IPL but fail to stratify (e.g. F, right). * p = 0.0110; ***$p < 1.0 \times 10^{-7}$. Dots, individual animals. Error bars, S.E.M. P-values, Tukey's post-hoc test. Sample sizes, see Methods.

H: Summary of *Ptf1a*^{cKO} SAC phenotype. Touching SACs are similar to wild-type SACs (Fig. 2M); they are able to innervate the IPL and form sublayers. Solitary SACs remain multipolar, similar to migrating SACs, and fail to innervate the IPL. Soma layer arbors are more elaborate than in wild-type or touching SACs.

Scale bars: 25 µm (A,C); 200 µm (B, left), 50 µm (B, right), 10 µm (D-F).

Figure 4

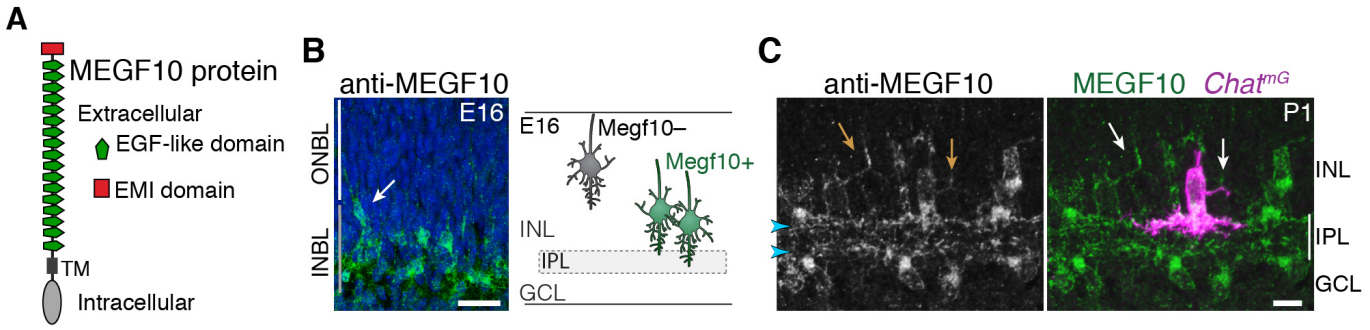

Figure 4: MEGF10 is expressed by SACs during early homotypic contact

A: Schematic of MEGF10 protein. TM, transmembrane domain.

B: Left, MEGF10 immunostaining at E16 reveals onset of protein expression at conclusion of radial migration. INBL SACs express MEGF10, but SACs migrating through ONBL do not. Arrow, INBL SAC with migratory morphology suggesting it is newly-arrived. Right: Schematic illustrating timing of *Megf10* expression onset in SACs (also see Kay et al., 2012).

C: SAC arbors in the INL (arrows) express MEGF10 protein. IPL dendrites are also labeled (arrowheads).

Scale bars: 25 µm (B); 10 µm (C)

Figure 5

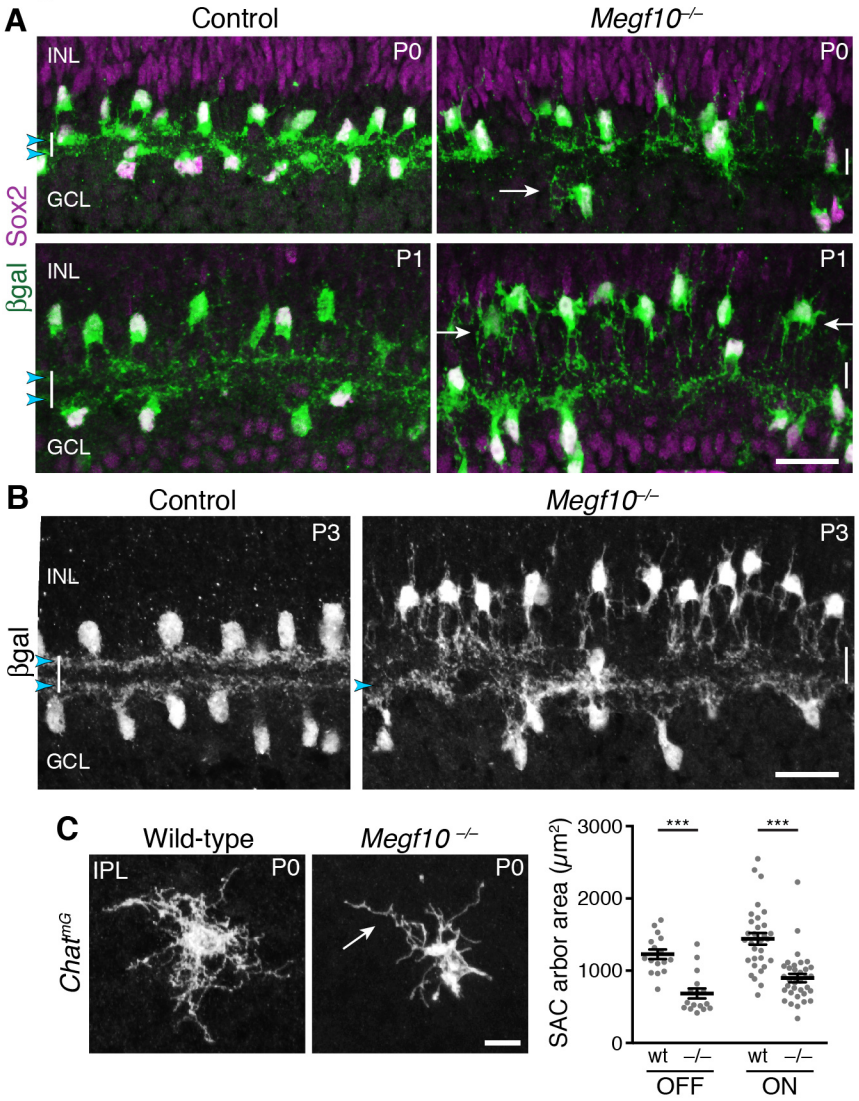

Figure 5: *Megf10* is required for initial formation of SAC IPL sublayers.

A: SAC sublayers are absent from P0-1 *Megf10* mutant IPL. Antibodies to Sox2 and βgal reveal SACs in retinal cross-sections. Littermate control, *Megf10*$^{lacZ/+}$. Vertical white lines denote IPL location. Arrowheads, SAC IPL strata. Arrows, exuberant arbor growth in mutant INL and GCL. Note that mutant somata abut the IPL at P0, indicating their radial migration was similar to controls. By P1 OFF somata have moved apically.

B: At P3, SAC IPL sublayers remain disrupted in *Megf10* mutants. Mutant OFF SACs mostly fail to ramify arbors in IPL; instead they arborize in INL (also see Fig. 6). INL projections are absent from controls. Some ON SACs are stratified in mutants (arrowhead) but have not yet formed a continuous restricted sublayer as is seen in controls.

C: Individual SACs show IPL innervation deficits in *Megf10* mutants. *En-face* whole-mount view of single P0 OFF SAC IPL arbors. Mutant SAC IPL dendrites appear undifferentiated, with less branching (arrow). Their arbors cover smaller retinal territories than SACs from wild-type (wt) littermate controls (quantified at right, mean ± s. e. m.). Images are Z-projections of slices encompassing full IPL arbor volume. ***p(on) < 1.0 x 10^{-7}, p(off) = 9.38 x 10^{-5}; one-way ANOVA/Tukey's post-hoc test. Sample size, see Methods.

Scale bars: 25 μm (A,B); 10 μm (C).

Figure 6

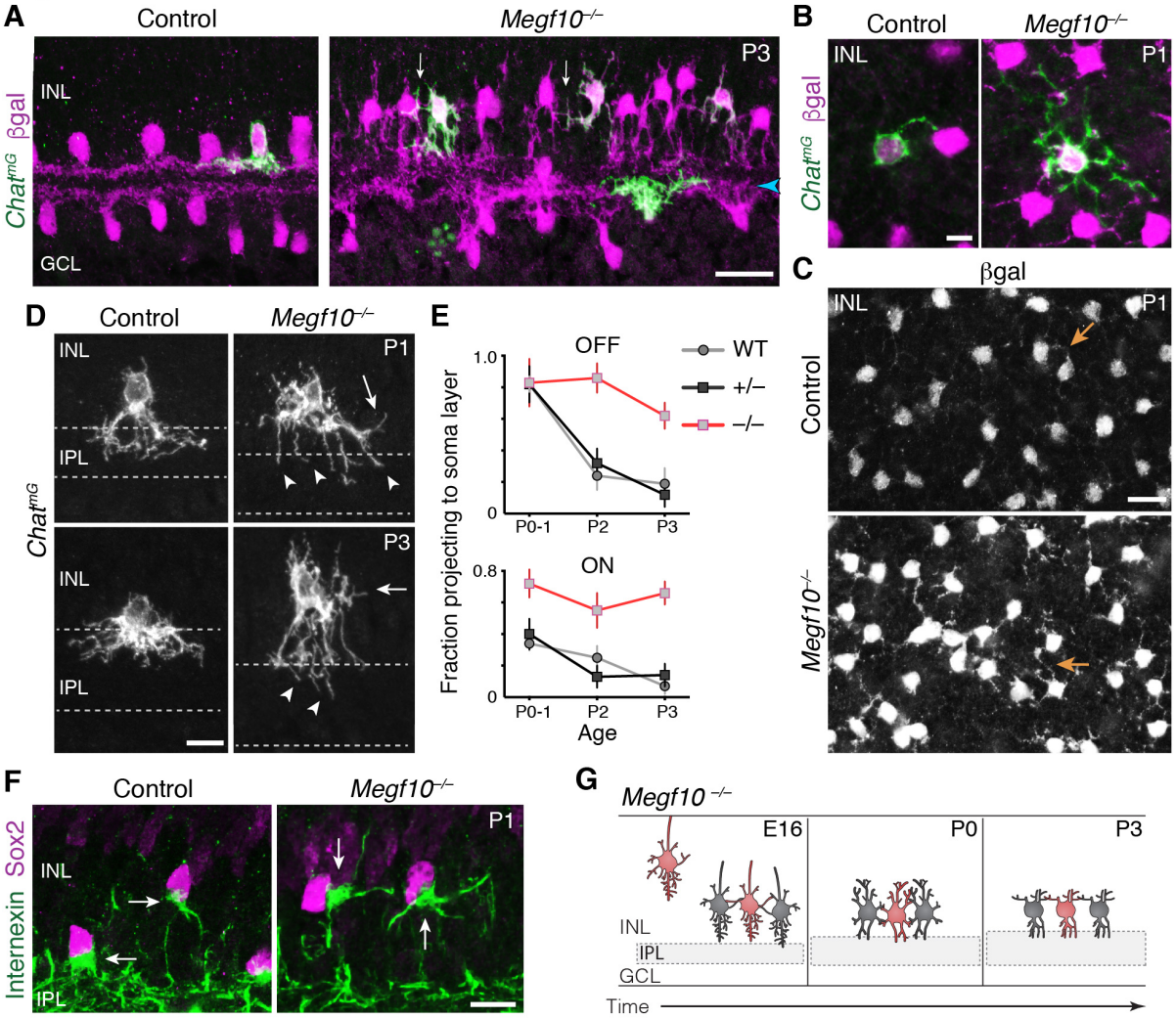

Figure 6: Exuberant soma-layer innervation by *Megf10* mutant SACs.

A,B: Individual SACs seen in cross-section (A) and whole-mount *en face* view (B) of *Chat*^{mG} tissue at indicated ages. *Megf10* mutant SACs have more extensive branches in INL than littermate *Megf10*$^{+/-}$ control SACs. Images in B are Z-projections of confocal slices encompassing each cell's INL arbors.

C: E*n face* images of βgal staining to show complete SAC INL network at P1. INL projections (arrows) are present at this age in controls (top); however, they are much more prominent in mutants (bottom), consistent with single-cell anatomy (B). Images are Z-projections of confocal slices encompassing volume of 2.0 µm (bottom) or 2.4 µm (top).

D: Higher-magnification view of individual OFF SACs labeled as in A. Genotypes and ages are indicated. Arrows, arbors in INL. Dashed lines denote borders of IPL. Mutant IPL projections (arrowheads) fail to arborize or stratify. See Fig. 6-Supplement 1 for ON SACs.

E: Frequency of soma layer projections across development in mutants (–/–) and littermate controls (+/–), determined from single *Chat*^{mG} cells as in D. Wild-type (WT) data replotted from Fig. 2L to show that +/– controls resemble WT. Error bars, standard error. Sample size, see Methods.

F: Internexin immunoreactivity reveals orientation of SAC primary dendrites (arrows) at P1. Right: Example of mutant SACs projecting primary dendrites in tangential plane, within soma layer. Control primary dendrites were almost exclusively oriented towards IPL (left). **G**: Summary of *Megf10*$^{-/-}$ phenotype. After initial contact at E16, mutant SACs do not immediately innervate the IPL, instead overgrowing arbors in cell body layers. This leads to delayed sublayer formation and persistent soma-layer projections at P3.

Scale bars: 25 µm (A,C); 10 µm (B,D,F).

Figure 7

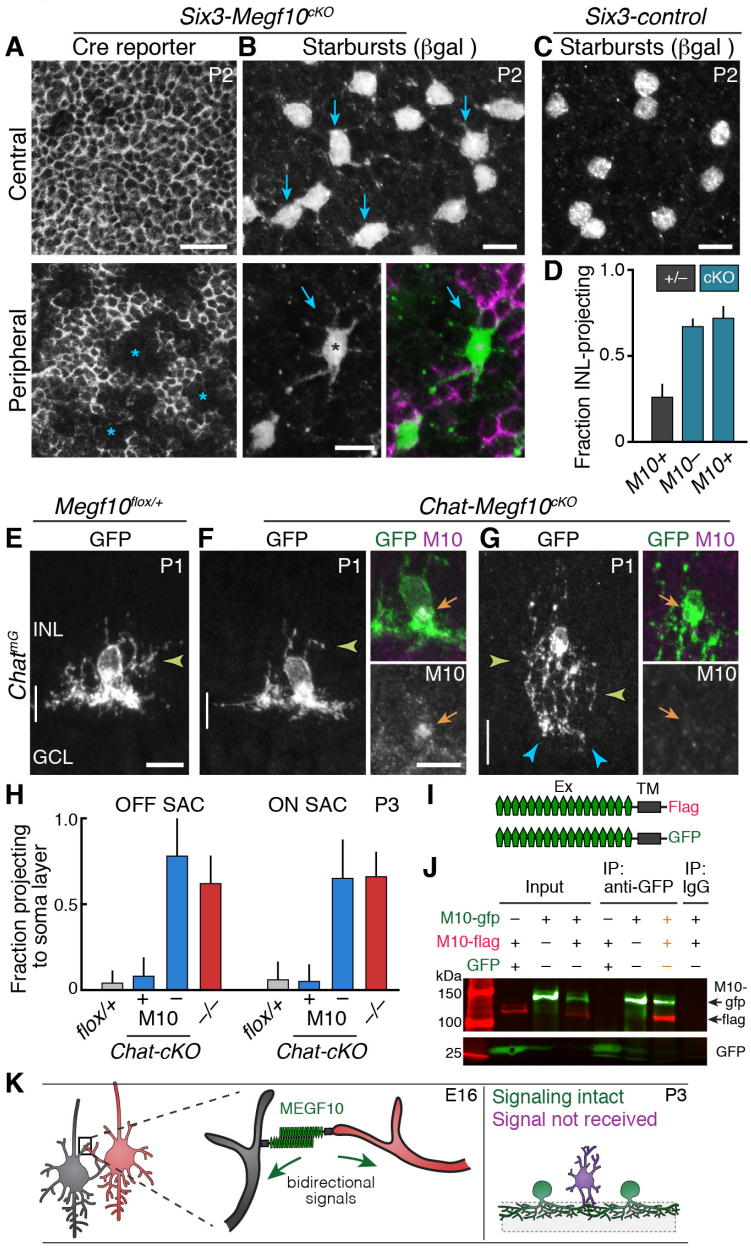

Figure 7: *Megf10* mediates transcellular SAC signals for dendrite development.

A,B: *En-face* images of INL in *Six3-Megf10*^{cKO} retinas stained for GFP Cre reporter (A) and βgal SAC marker (B). Reporter expression indicates loss of MEGF10 (see Fig. 7-Supplement 1). In central retina (top row), most SAC are mutant, and project extensive INL dendrites (B, arrows; compare to C). In peripheral retina (bottom row), some cells escape Cre (asterisks) and retain MEGF10 but still make ectopic INL projections. Purple, Cre reporter; green, βgal.

C: Littermate control retina imaged as in B; SACs rarely project INL dendrites at P2.

D: Quantification of P2 INL projection phenotypes illustrated in A-C. *Six3-Megf10*^{cKO} (*cKO*) SACs that escape Cre (M10^{+}) make projection errors at similar rate as surrounding mutant cells from the same tissue (M10$^{–}$).

E-G: *Chat-Megf10*^{cKO} phenotype. Morphology of single SACs, revealed by *Chat*^{mG} in cross-sections. Anti-MEGF10 (M10) distinguished two classes of *cKO* SACs (orange arrows): Those that express MEGF10 (F) are anatomically similar to littermate control SACs (E). Those lacking MEGF10 (G) arborize extensively in INL (yellow arrowheads) but minimally in IPL (blue arrowheads). Vertical line, IPL.

H: Quantification of SAC soma-layer projection frequency at P3. Sparse M10 deletion (blue, –) phenocopied germline null (red). *Chat-Megf10*^{cKO} cells that retained M10 (blue, +) resembled controls (*flox/+*).

I: Schematic of MEGF10 proteins used for co-immunoprecipitation (IP). Intracellular domain was deleted (ΔICD) and replaced with epitope tags (Flag or GFP). Ex, extracellular; TM, transmembrane.

J: Co-IP from lysates of HEK 293T cells transfected with indicated constructs (I). Western blot with antibodies to GFP (green) and Flag (red). IP with anti-GFP, but not rabbit IgG control, pulled down both MEGF10-ΔICD constructs (2nd lane from right, orange text). IP with anti-Flag gave similar result (Fig. 7-Supplement 2). GFP alone did not co-IP with M10-Flag. Ladder molecular weights (kDa) at left. Full blots in Fig. 7-Supplement 2.

K: Model of MEGF10 function in early SAC dendrite development. Left, soma-layer contact between neighboring SACs initiates MEGF10-mediated signaling in each cell. This signal inhibits soma-layer dendrite growth and promotes arborization in IPL (see green cell, right panel). Purple, phenotype of SACs that fail to receive MEGF10 signals, either because neighbors do not have MEGF10, or because the cell itself lacks MEGF10 as a receptor. These SACs project exuberant soma-layer arbors and fail to ramify dendrites in IPL.

Error bars, 95% confidence interval. Sample sizes, see Methods. Scale bars: 25 µm (A), 10 µm (B-G).

Figure 8

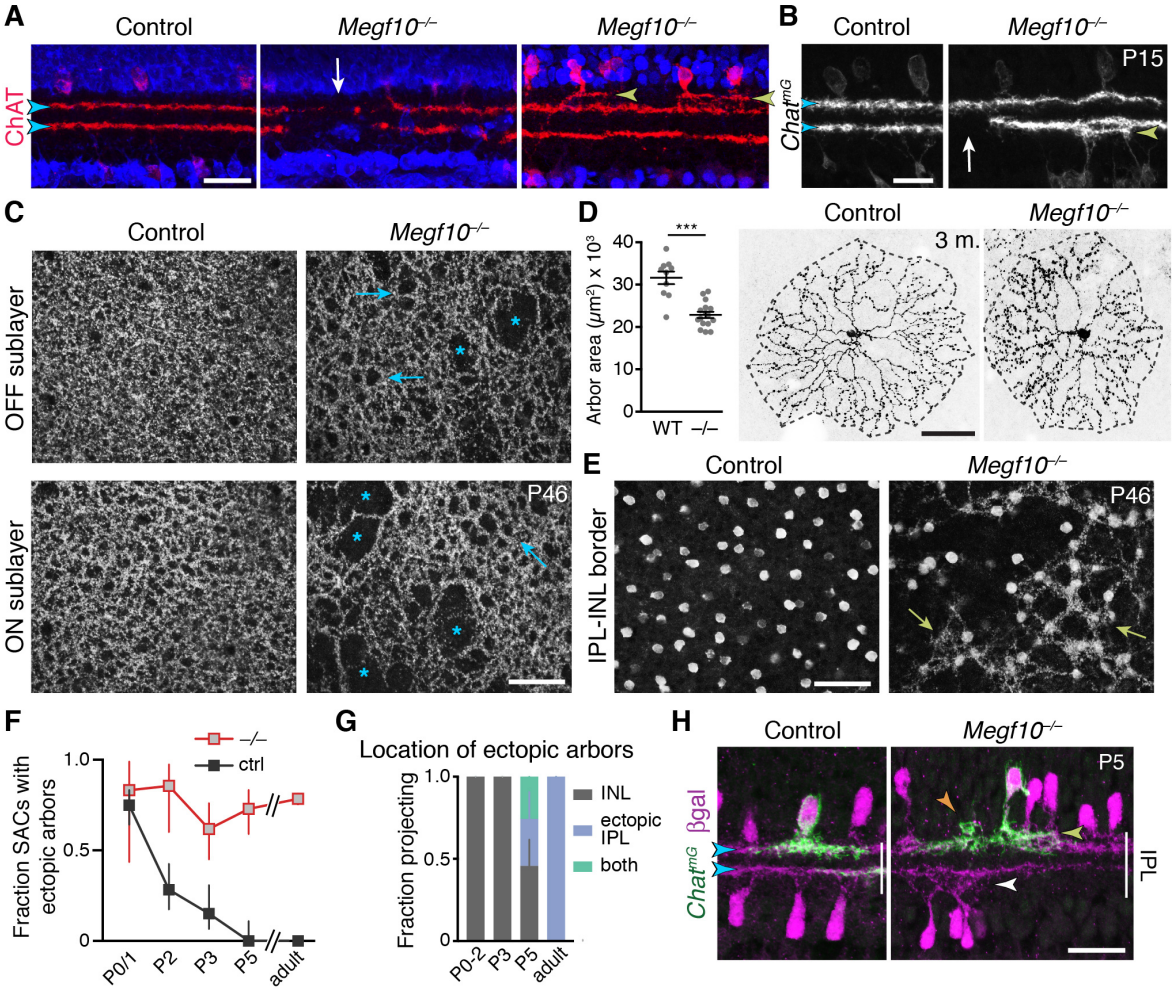

Figure 8: SAC IPL errors persist to maturity in *Megf10* mutants.

A,B: SAC IPL phenotype in mature (two-week-old) retina, cross-section view. Blue, soma counterstain. Control IPL has two continuous SAC dendrite bands (blue arrowheads). Mutant IPL has sporadic ectopic SAC arbors (yellow arrowheads) or laminar gaps (white arrows).

C: *En-face* views of SAC dendrites, stained with anti-ChAT, in adult retinal whole-mounts. The same fields of view are shown at two different Z-stack planes, corresponding to OFF and ON SAC sublayers. SAC dendrite plexus is uniform in littermate controls, but has holes (arrows) and large gaps (asterisks) in mutants. Note that errors are not spatially correlated between OFF and ON sublayers. Images are Z-projections of 5 slices encompassing 2.0 µm in Z.

D: Single SAC labeling in adult (3 month old) mice, via $Chat^{Cre}$-dependent viral fluorescent protein expression. $Megf10^{-/-}$ SACs have relatively normal morphology but are significantly smaller than wild-type (WT) control cells (***$p = 4.6 \times 10^{-6}$, two-tailed *t*-test). Sample size, see Methods.

E: *En-face* images reveal extent of ectopic mutant SAC dendrite network. Same fields of view as C, but at different Z-planes depicting OFF IPL (at IPL-INL border). In mutant but not control, SAC dendrite fascicles (arrows) are evident at this IPL level. Images are Z-projections of 3 (left) or 2 (right) slices spaced 0.4 µm in Z.

F,G: Dendrite targeting of individual OFF SACs assessed across development. Fraction of mutant SACs projecting into ectopic network does not change over time (F). However, location of ectopic arbors shifts from INL to IPL (G), starting at P5, when cells projected to either or both locations (G,H). In F, P0-3 data are replotted from Fig. 6E, with both control groups combined.. Sample sizes, see Methods.

H: Example P5 SACs from *Megf10* mutant and littermate control. A mutant SAC projects to three different locations: 1) correct IPL sublayer (blue arrowhead); 2) ectopic IPL sublayer (yellow arrowhead); 3) ectopic INL arbor aggregate (orange arrowhead). ON SACs also make ectopic IPL projections (white arrowhead). Control cells are monostratified in IPL (left). Note that SAC sublayers have formed by P5 in mutants.

Error bars, 95% confidence intervals. Scale bars: 50 µm (C-E); 25 µm (A,B,H).

Figure 9

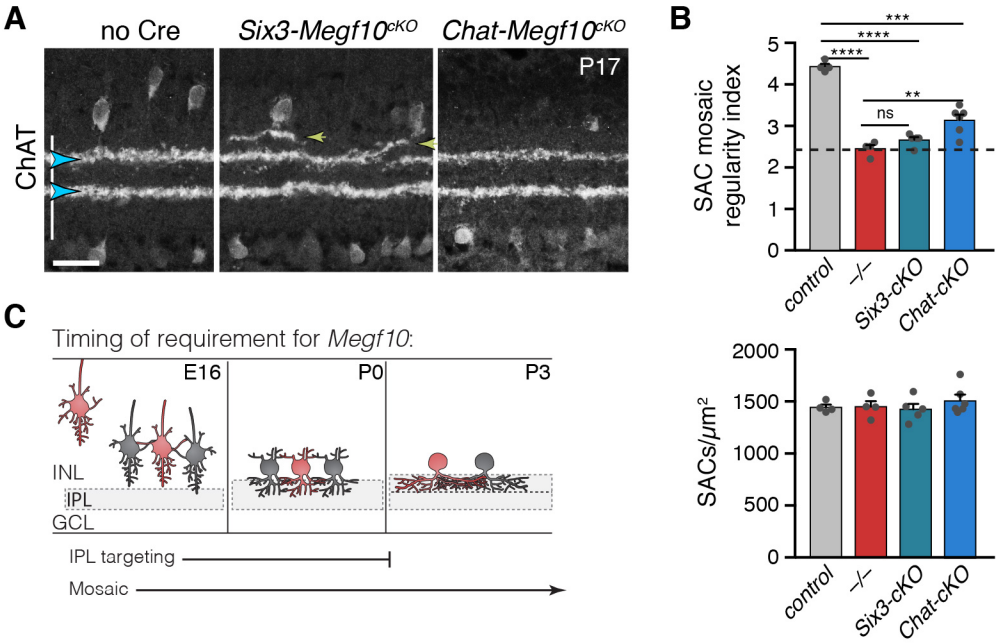

Figure 9: Temporal requirements for MEGF10 in SAC IPL stratification and mosaic spacing.

A: SAC IPL errors (yellow arrowheads) induced by early deletion of *Megf10* in *Six3-Megf10*^{cKO} mice, but not deletion between P3-5 in *Chat-Megf10*^{cKO} mice (see Fig. 7-Supplement 1 for MEGF10 expression in these strains). Blue arrowheads, SAC sublayers.

B: Mosaic spacing phenotype measured at P17 using Voronoi domain regularity index (top graph). Dashed line, index for simulated random SAC arrays. In both *Six3* and *Chat* conditional mutants, SAC positioning is less regular than in controls (*Chat*^{Cre}; *Megf10*$^{flox/+}$). *Megf10*$^{-/-}$ and simulation data from Kay et al. (2012). ns, $p = 0.6438$; $^{**}p = 0.0023$; $^{***}p = 2.1 \times 10^{-6}$; $^{****}p < 1.0 \times 10^{-6}$ (one-way ANOVA/Tukey's post-hoc test). Bottom graph, regularity effects are not due to changes in SAC cell density across genotypes. One-way ANOVA, $F(3, 15) = 0.6063$; $p = 0.6210$.

C: Summary of results from all conditional *Megf10* mutant studies (A, B; Fig. 7). Loss of MEGF10 while soma-layer arbors are present (i.e. prior to P3) disrupts both SAC mosaic patterning and IPL laminar targeting; this conclusion is based on phenotypes of: 1) germline mutant; 2) *Six3-Megf10*^{cKO} mutant; 3) occasional cells in *Chat-Megf10*^{cKO} mice that lost MEGF10 prior to P3 (Fig. 7F-H). When MEGF10 is lost after P3, as is the case for most *Chat-Megf10*^{cKO} SACs (Fig. 7-Supplement 1), only mosaic is disrupted (A,B). Thus, MEGF10 acts at distinct, albeit partially overlapping times, to influence these two distinct SAC developmental events.

Error bars, S.E.M. Scale bar, 25μm.

Figure 10

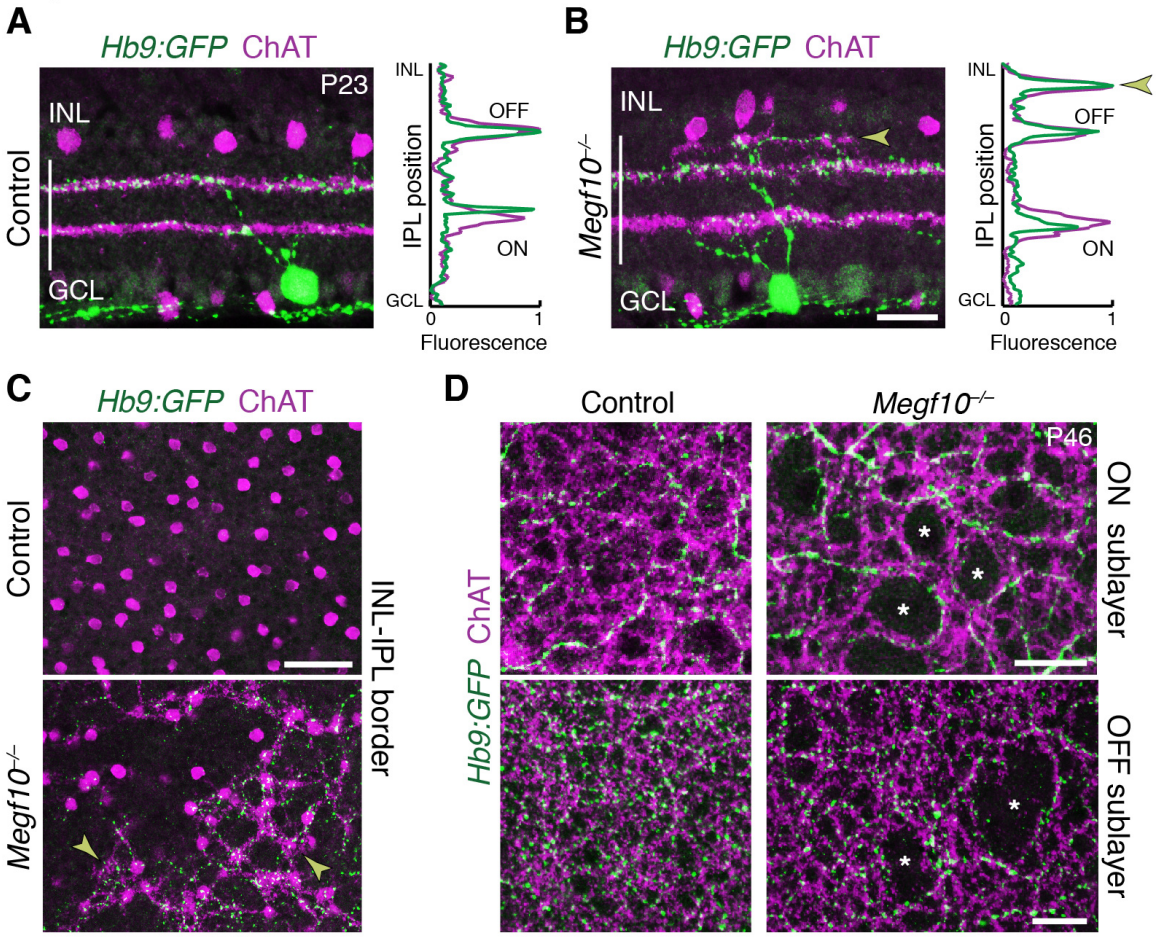

Figure 10: SACs guide IPL sublayer choice by ooDSGCs.

A,B: SACs (ChAT, purple) and ooDSGCs (*Hb9:GFP*, green) labeled in cross-sections. Right panels, fluorescence profile plots across IPL showing position of ON and OFF sublayers. In both controls (A) and *Megf10* mutants (B) ooDSGC dendrites strictly co-localize with SAC arbors. Arrowhead (B), ectopic sublayer.

C: *En-face* view of OFF IPL near INL border. Same fields of view as Fig. 8E. In *Megf10* mutants (bottom), the ectopic SAC network is extensively innervated by ooDSGC dendrites (arrowheads). Control retina (top) lacks DS circuit arborization at this IPL level.

D: *En-face* view of ON (top) and OFF (bottom) SAC IPL sublayers. In *Megf10* mutants, ooDSGC dendrites (green) fail to enter IPL regions (asterisks) that are not innervated by SACs (purple).

Images in C,D are Z projections of confocal slices encompassing ≥ 1.2 µm (C) or 2-4 µm (D).

All scale bars: 25 µm. Also see Fig. 10-Supplement 1 for phenotype of *Drd4:GFP* ooDSGCs.

Figure 11

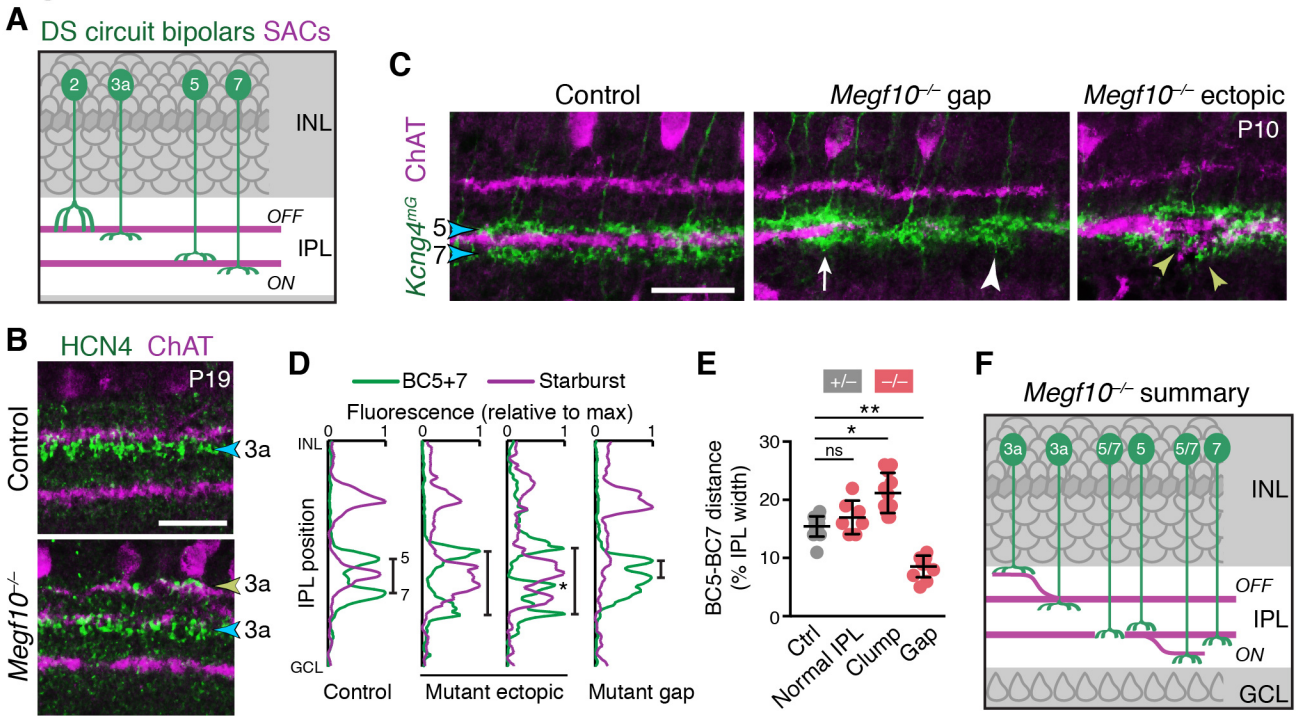

Figure 11: SACs guide IPL sublaminar targeting by DS circuit bipolar cells.

A: Illustration depicting anatomy of four bipolar cell types known to participate in DS circuit. BC3a, BC5, and BC7 arborize axons in narrow sublayers directly adjacent to SAC strata. BC2 projects more broadly through OFF IPL, overlapping with SAC sublayer (see Fig. 11-Supplement 1).

B: BC3a IPL projections assessed with anti-HCN4. Blue arrowhead, normal BC3a stratum. Yellow arrowhead, ectopic stratum containing SAC dendrites (purple) and BC3a axons (green).

C,D: BC5 and BC7 IPL projections (blue arrowheads), labeled in *Kcng4*^{mG} mice. D, images; E, representative fluorescence plots of *Kcng4*^{mG} (green) and ChAT (purple) across IPL. In littermate controls, or normal regions of mutant IPL (C, arrow), BC5 and BC7 arborize in sublayers immediately adjacent to ON SAC layer, but do not enter it. In *Megf10* mutants, ectopic SAC arbors displace BC5+7 terminals to new IPL locations, where they remain adjacent to SACs but non-overlapping (C, yellow arrowheads; D, center plots). Asterisk (D): ectopic BC arbors between normal and ectopic SAC strata. BC5/7 arbors can innervate gaps in the SAC stratum (C, center panel); in these cases their terminals are abnormally close together (C, white arrowhead; D, right plot). Vertical bars in D: distance between BC5/7 strata.

E: Quantification of BC5-BC7 distance in normal IPL and in presence of SAC innervation gaps or ectopic arbor clumps. *$p = 0.0219$; **$p = 0.0012$; ns, $p = 0.3965$ (Tukey's post-hoc test). Sample sizes, see Methods. Error bars, S.E.M.

F: Summary of *Megf10*$^{-/-}$ bipolar cell phenotypes. BC3a, BC5, and BC7 are illustrated here (see Fig. 11-Supplement 1 for BC2). Each of these cell types can either make errors (left cell in each pair) or project normally (right cell). All three cell types show recruitment to ectopic IPL locations. BC5 and BC7 terminals innervating SAC gaps colonize the sublayer normally occupied by SACs.

Error bars, 25 µm.

Figure 12

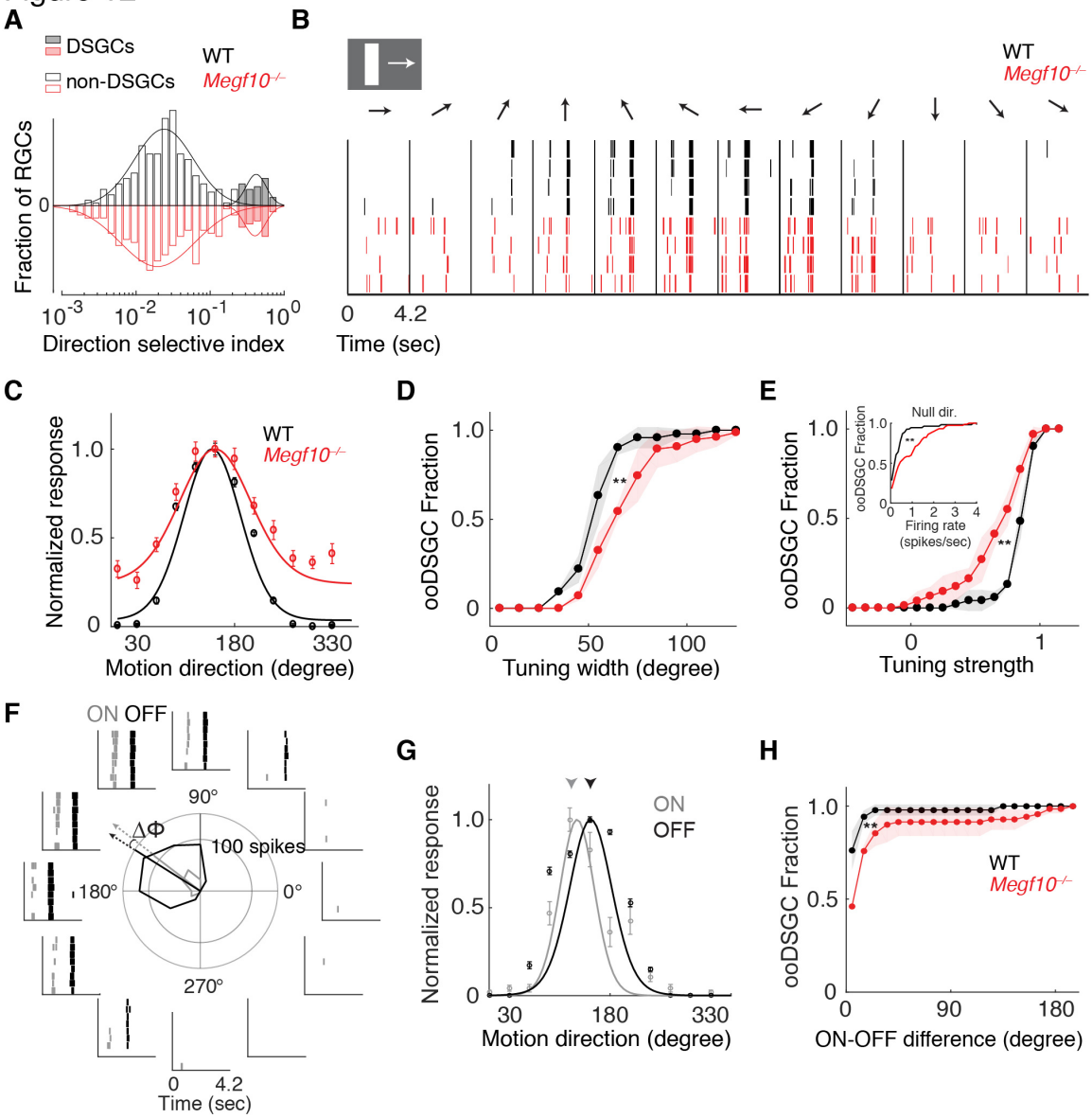

Figure 12: Broader and weaker direction tuning of ooDSGCs in *Megf10* mutants.

A: Histograms of RGC direction selectivity indices, measured on a multielectrode array, for wild-type (WT, black) and *Megf10*$^{-/-}$ (red) retinas. Bimodal histograms fit with two-Gaussian mixture model distinguished DSGCs (filled bars) from non-DSGCs (open bars).

B: Spike rasters from representative WT and *Megf10*$^{-/-}$ posterior-preferring ooDSGCs in response to a bright bar moving along 12 directions (arrows).

C: Direction tuning curves from cells in B normalized to the maximum response (line: von Mises fit). Non-zero values at tails of mutant curve reflect increase in null-direction spikes (B, left- and right-most bins).

D,E: Cumulative distribution of tuning widths (D) and tuning strengths (E) for all ooDSGCs recorded from two retinas of each genotype (WT n = 80 cells; *Megf10*$^{-/-}$ n = 74 cells). Mutant ooDSGC population is tuned more broadly (D, right shift of red curve) and more weakly (E, left shift of red curve) than WT. Similar results were obtained when ON and OFF responses were considered separately (not shown). Mutant ooDSGCs also exhibit higher firing rate to null direction motion (E, inset). **p = 0.005 (D), p = 0.003 (E), paired KS-test.

F: Rasters and polar plot of a representative WT ooDSGC, highlighting preferred directions of ON (gray) and OFF (black) responses (arrows). Δϕ, angular difference between preferred directions of ON and OFF responses.

G: ON and OFF direction tuning curves for cell in F (line, von Mises fit). ON and OFF preferred directions (arrowheads) are well aligned in WT retina.

H: Cumulative distribution across all ooDSGCs of ON-OFF preferred direction difference (Δϕ). Same cells as in D,E. Rightward shift of mutant curve indicates larger ON-OFF misalignment. **p = 0.004, paired KS test.

For all panels, background light level was photopic (10^4 P*/M-cone/sec; contrast of moving bar was 60%). Error bars/bands, S.E.M. Also see Fig. 12-Supplement 1.

Formation of retinal direction-selective circuitry initiated by starburst amacrine cell homotypic contact

Thomas A. Ray, Suva Roy, Christopher Kozlowski, Jingjing Wang, Jon Cafaro, Samuel W. Hulbert, Christopher V. Wright, Greg D. Field, and Jeremy N. Kay

SUPPLEMENTAL FIGURES & LEGENDS

Figure 1 - Supplement 1

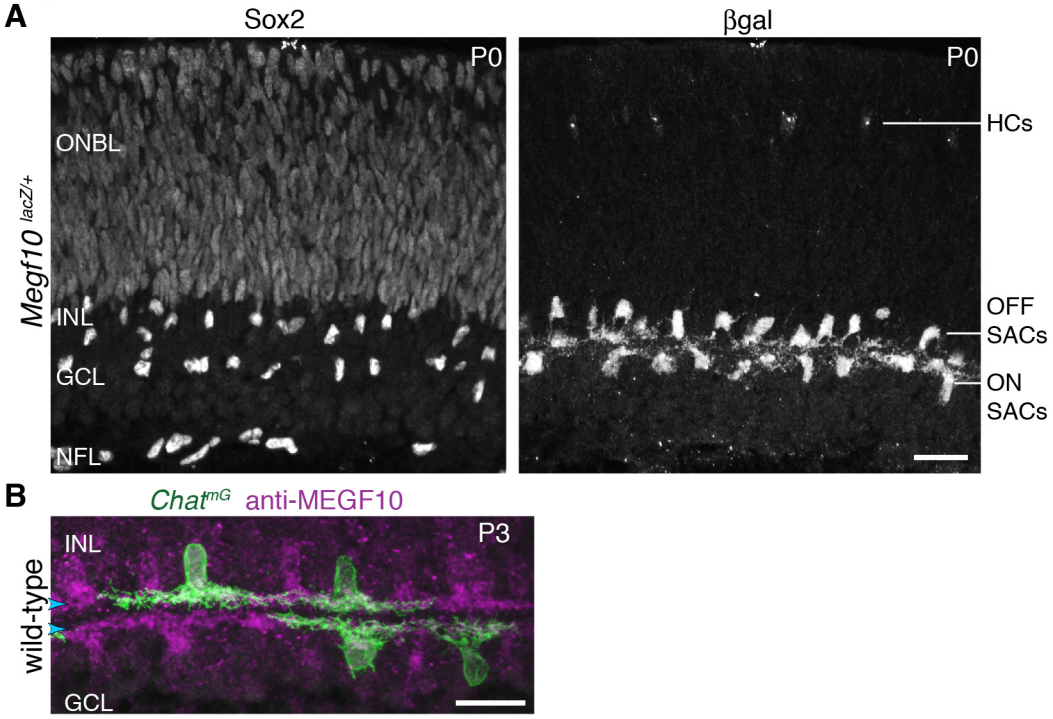

Figure 1-Supplement 1: Characterization of SAC markers in neonatal retina. **A**: Sox2 and *Megf10* as SAC markers at P0. Individual color channels of P0 cross-section image shown in Fig. 1B. Sox2 (A, left panel) is a pan-SAC nuclear marker. Antibodies to Sox2 strongly label all SACs in the inner nuclear layer (INL) and ganglion cell layer (GCL), as well as astrocytes in the nerve fiber layer (NFL). Progenitor cells in the outer neuroblast layer (ONBL) are weakly labeled. Antibodies to βgal (A, right panel) label the complete SAC population in *Megf10*^{lacZ} mice. Horizontal cells (HCs) in outer retina are also labeled.

B: Antibodies to MEGF10 (purple) are selective for SACs and label the complete SAC population. *Chat*^{mG} mice (i.e. *Chat*^{Cre} crossed to membrane-targeted GFP Cre reporter) label a subset of SACs in the neonatal retina (green). Whereas *Chat*^{Cre} is a marker of the full SAC population at later stages, its expression in neonatal retina is more sporadic (Xu et al., 2016). We took advantage of this feature for two purposes: 1) Single-cell anatomy studies of SAC dendrite morphology, as shown here; and 2) sporadic early knock-out of genes in a sparse subset of SACs (See Fig. 6).

Scale bars: 25 µm.

Figure 1 - Supplement 2

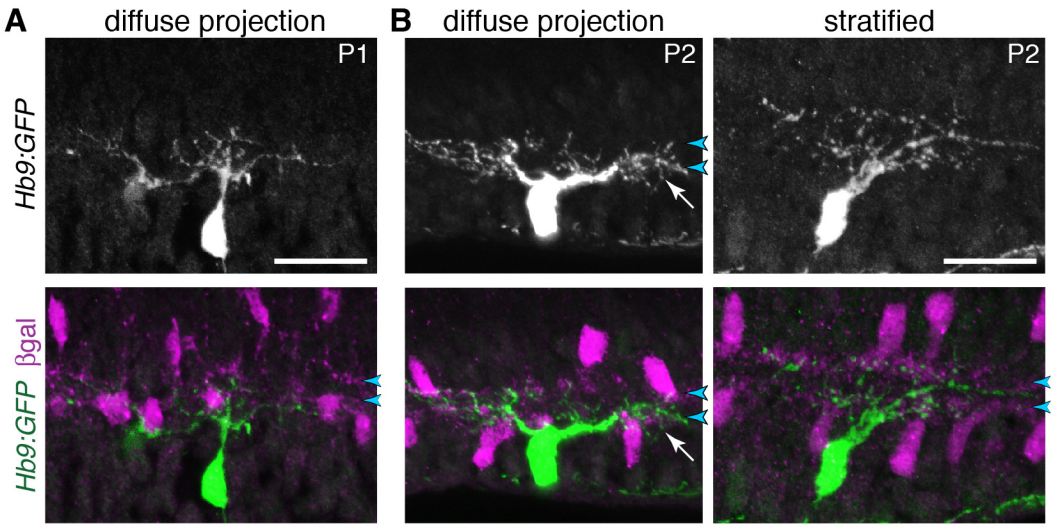

Figure 1-Supplement 2: ooDSGC stratification in neonatal retina.

A: Anatomy of P1 ooDSGCs labeled with *Hb9:GFP*. SACs are labeled by *Megf10*:βgal. At this age, ooDSGC dendrites are rudimentary with few branches. No IPL stratification is evident. This cell was used for the IPL fluorescence plot shown in Fig. 1E.

B: Examples of P2 ooDSGCs that were scored as diffusely-projecting (left) or stratified (right). Blue arrowheads, SAC sublayers. Arrow (center panel), arbors that fill IPL in area between SAC strata. See main text for quantification of stratification frequency.

Scale bars: 25 µm.

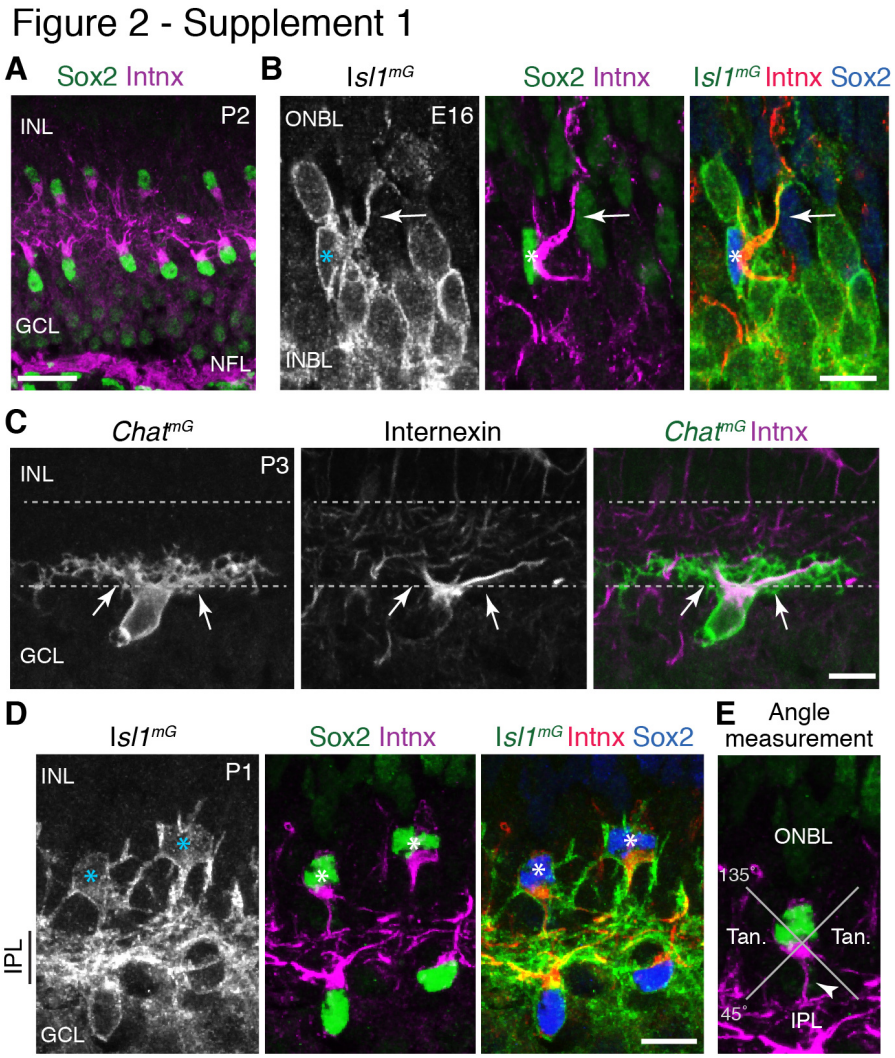

Figure 2-Supplement 1: Characterization of internexin as a primary dendrite marker of developing SACs.

A: Expression pattern of internexin in P2 mouse retina. Internexin (Intnx) immunoreactivity is detected in Sox2$^+$ SACs, and in RGC axons within the nerve fiber layer (NFL). This pattern is typical of the entire first postnatal week. In RGCs, axons are selectively labeled; their cell bodies in the GCL are internexin-negative. In SACs, internexin selectively labels primary dendrites, as well as the portion of the soma from which the primary dendrites arise. Therefore, internexin$^+$ intermediate filaments are trafficked to specific subcellular compartments of both SACs and RGCs. P2 SACs are strongly polarized towards the IPL (also at P1; see D). Note that this image is the same one depicted in Fig. 2E, but cropped differently; also, colors have been reversed to match other panels of this figure.

B: An individual E16 INBL SAC (asterisk), surrounded by *Isl1^{mG}*-positive RGCs (identified as RGCs because they lack Sox2 or internexin staining). At E16, internexin has the same subcellular localization within SACs as at P1-2 (A,D): It localizes to the primary dendrites (arrow) and the side of the cell body from which it emerges. However at E16, SAC primary dendrite orientation is more variable than at P2 (see Fig. 2E,F). This SAC sends a primary dendrite towards the outer retina (ONBL) where it could potentially contact migrating SACs as they arrive at the INBL.

C: Antibodies to internexin strongly label SAC primary dendrites originating from the cell body (arrows), but fine dendritic branches within IPL are unlabeled. Occasionally, higher-order branches arising from the primary dendrites are weakly labeled. *Chat^{mG}* was used to reveal the full dendritic arbor.

D: Internexin distinguishes IPL-directed primary dendrites from soma-layer arbors in neonatal SACs. *Isl1^{mG}* labels full morphology of bi-laminar P1 OFF SACs (asterisks) that project to both INL and IPL. Only IPL-directed primary dendrites of these cells are internexin-positive (middle, right panels).

E: Schematic of method used to measure primary dendrite orientation (Fig. 2F). For each cell, the angle between the primary dendrite (arrowhead) and a plumb line directed to IPL was measured. Cells projecting within the labeled quadrants were defined as projecting towards IPL, towards ONBL, or tangentially (Tan).

Scale bars: 25 µm (A), 10µm (B-D).

Figure 2-Supplement 2

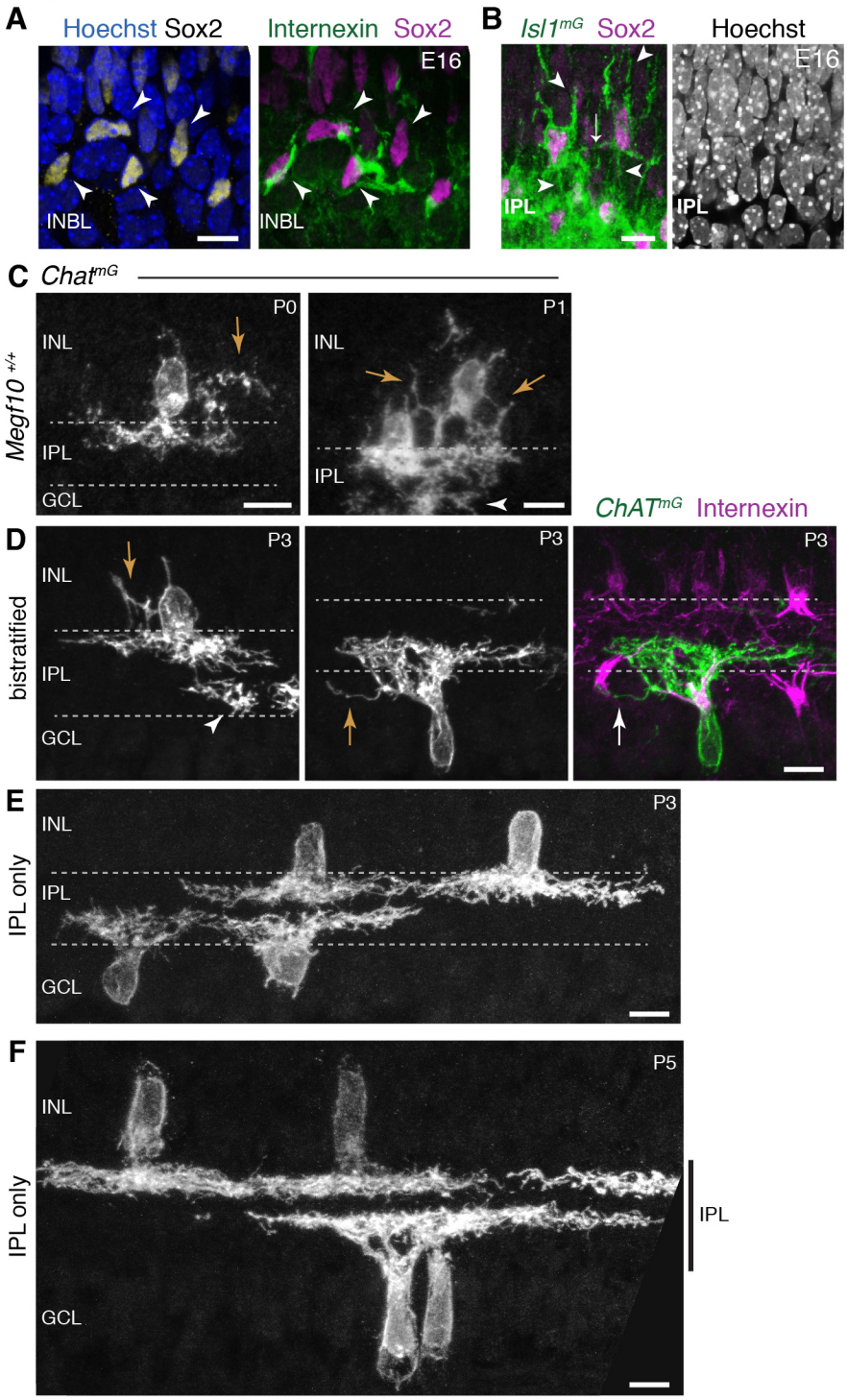

Figure 2-Supplement 2: Soma-layer SAC arbors across development.

A: E16 soma-layer arbor network can be established prior to IPL formation. Right panel, same cells as Fig. 2E, showing INBL SACs projecting towards each other. Left panel, same field of view showing Sox2 SAC nuclear marker and Hoechst nuclear stain (blue). These SACs are surrounded by other INBL cell bodies, with no IPL neuropil evident in this retinal region.

B: E16 homotypic SAC soma contacts occur outside the IPL. Left panel, same cells as Fig. 2D. Cells have migratory morphology, as shown by their prominent apical and basal processes (arrowheads). They do not make obvious projections into IPL, delineated by dense *Isl1*^{mG} staining. Contact between the two SACs (arrow) occurs outside of IPL Right panel, Hoeschst nuclear stain confirms location of nascent IPL inferred from *Isl1*^{mG} labeling. IPL is narrow cell-free gap that corresponds to location of dense GFP^{+} arbors (left panel).

C: Examples of soma layer-projecting *Chat*^{mG}-labeled SACs in mice that are wild-type at the *Megf10* locus (*Megf10*$^{+/+}$), demonstrating that the soma-contacting arbors shown in Fig. 2H-K are not a consequence of *Megf10* heterozygosity. Arrows, arbors in INL. Arrowhead, arbors arising from a neighboring ON SAC with cell body located in adjacent section.

D-F: Examples of P3 (D-E) and P5 (F) cells used to generate graph in Fig. 2L. SAC single-cell morphology was revealed using *Chat*^{mG} labeling. At P3, most SACs project only to the IPL (E), but some SACs still make soma-layer projections (D). Representative INL-projecting OFF cell (D, left) and GCL-projecting ON cell (D, center, right) are depicted. The ON cell makes contact with the neighboring internexin-positive SAC soma (arrow in right panel of D). Arrows, soma-layer projecting arbors. Arrowhead, arbor of a neighboring ON SAC only partially present in the section. At P5 (F), all SACs project exclusively to IPL (vertical bar).

All scale bars: 10 µm.

Figure 2 - Supplement 3

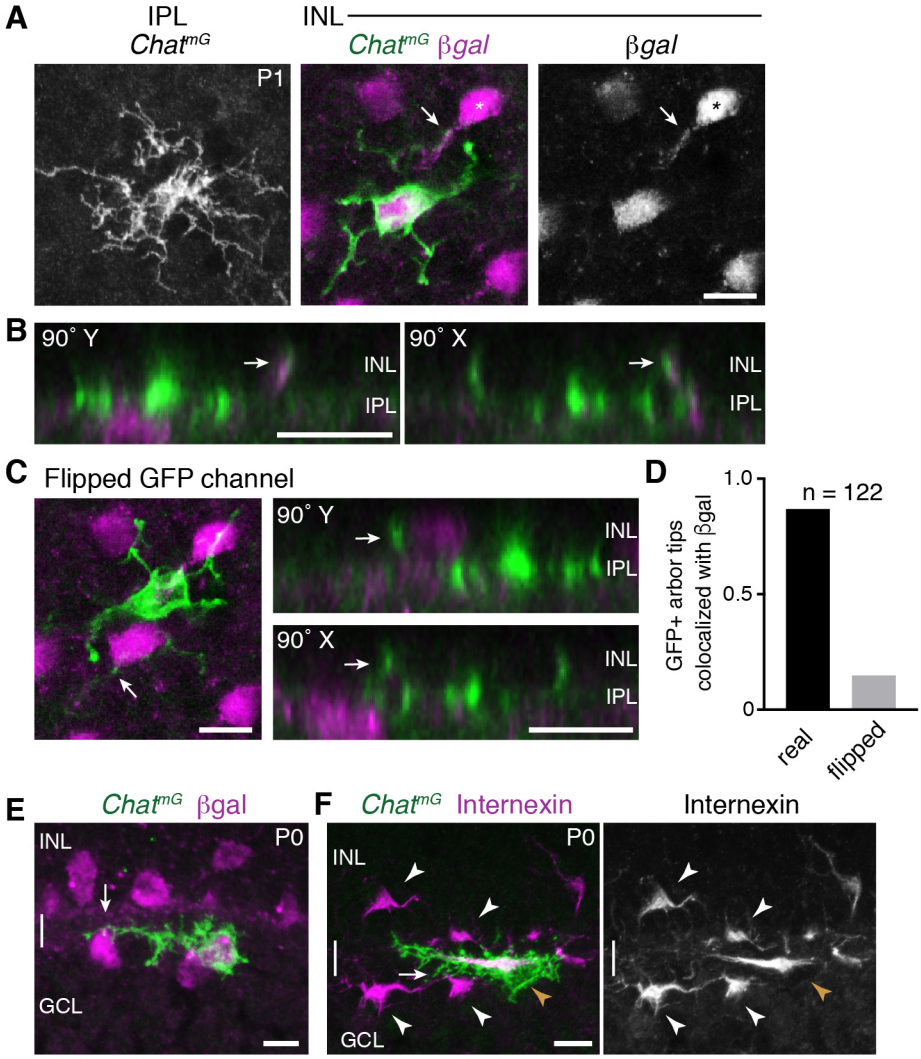

Figure 2-Supplement 3: Homotypic specificity of soma-layer SAC projections.

A: Single SAC from P1 *Chat*^{mG} retinal whole-mount, imaged at level of IPL (left) and INL (center, right). *Megf10*:βgal marks the full SAC population. INL images are from a single confocal Z-stack plane. A GFP+ arbor tip that terminates on a βgal-positive neighboring SAC is marked (arrow, arbor tip). Most of the cell's other arbor tips are outside this focal plane, where several terminate on other SACs (not shown). IPL image is a maximum-intensity projection of 3 Z-stack slices (1.5 µm total distance).

B: Orthogonal (90˚ rotation) views of a Z-stack (0.5 µm Z resolution) through the cell shown in A. Left, Y-axis rotation; right, X-axis rotation. Arrows mark the same interacting INL arbors as in A. Note colocalization of green and purple arbors regardless of whether cell is viewed *en face* (A), or from the orthogonal perspectives (B).

C: The same cell as in A but with the GFP channel flipped in X and Y. This serves as a negative control to test whether superposition of GFP and βgal signals might occur by chance, given the density and geometry of each staining in the P1 retina. Arrows mark same arbor tip as in A,B. In *en face* view (left), the arbor crosses a βgal^{+} cell body but terminates just beyond it. The lack of colocalization between this arbor tip and the adjacent cell body is clear in orthogonal rotation views (right).

D: Quantification of INL arbor homotypic specificity. The fraction of *Chat*^{mG}-labeled SAC dendrite arbor tips terminating on βgal^{+} neighbors was counted by examining z-stacks and orthogonal views (as in B). This was done for real image stacks, as well as for stacks with one channel flipped as in C. A high rate of homotypic interaction was observed for the real data (88.8%) but not the flipped negative control data (14.9%). Sample size, n = 122 arbors from 22 SACs, two retinas each genotype.

E,F: ON SACs can contact neighboring SAC somata (arrows) without being bi-laminar. Cross-sections of P0 retina, co-stained for individual SACs (*Chat*^{mG}) and markers of the complete SAC population (E, *Megf10:*βgal; F, internexin). The two cells shown here establish soma contact without a separate GCL projection; instead, these cells send fine branches from their IPL arbors to establish contact. These cells are representative of a phenomenon that was observed frequently among ON SACs at P0. The existence of such cells may help explain why the frequency of soma layer-projecting ON SACs is lower than for OFF SACs (Fig. 2L). Internexin staining (F) shows that these ON SACs (orange arrowhead) are polarized in the tangential plane along the INL-

GCL border towards their neighbors, adopting a horizontal morphology distinct from surrounding OFF and ON SACs (white arrowheads). This morphology is typical of a displaced amacrine cell in the process of crossing from the INL to the GCL (Chow et al., 2015).

Scale bars: 10 μm.

Figure 3 - Supplement 1

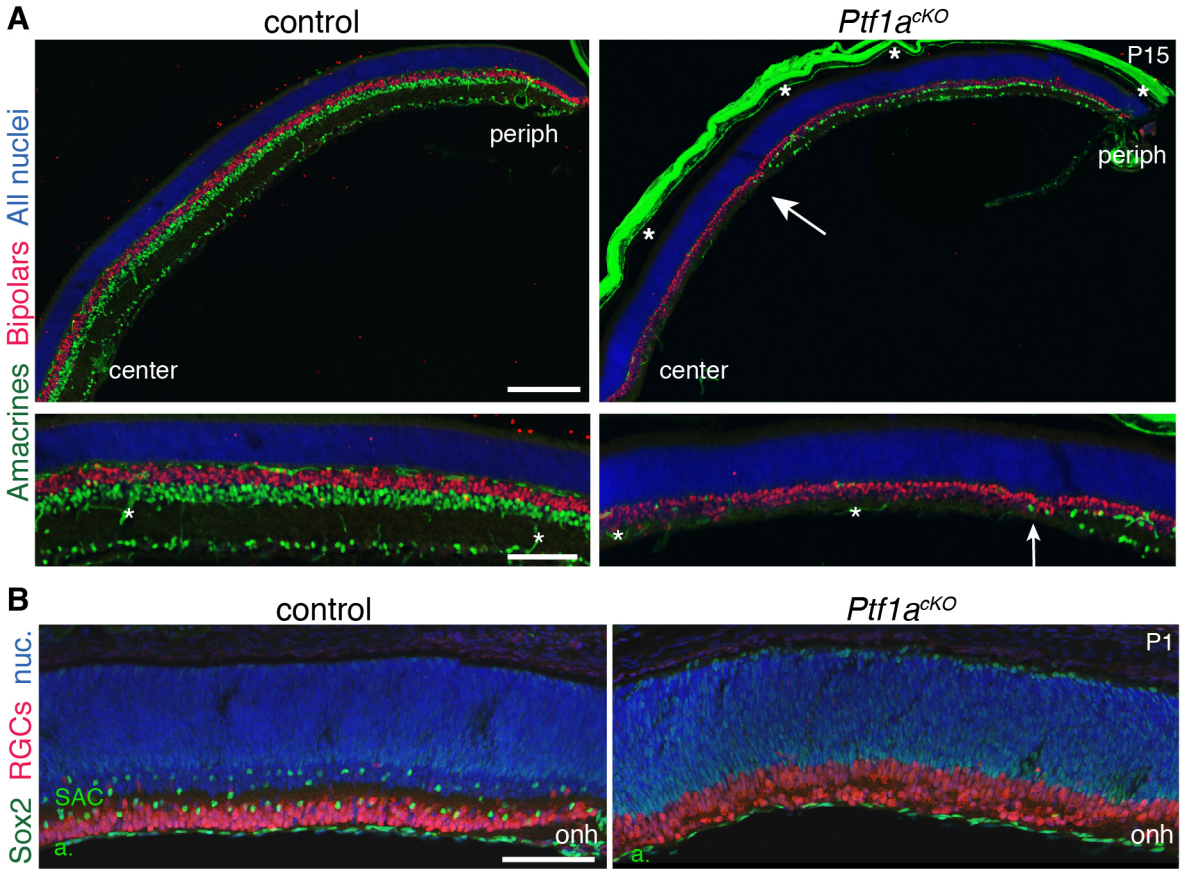

Figure 3-Supplement 1: Retinal cell types in *Ptf1a*^{cKO} mutants.

A: Immunostaining with pan-amacrine marker AP2α (green) and pan-bipolar marker Chx10 (red), in littermate control and *Ptf1a*^{cKO} retinal cross sections. Blue, Hoechst nuclear counterstain. Top panels: low-power view illustrating center-peripheral differences in amacrine number that arise due to Cre expression pattern (see Fig. 3A-C). Bottom panels: Higher magnification views of mid-peripheral retina. AP2α^{+} cells are completely eliminated from *Ptf1a*^{cKO} central retina. Some amacrines that have escaped Cre recombination (see Fig. 3C) are produced in the periphery, albeit at lower density than controls. Arrow marks central-most amacrine cells. Bipolar cell number is not obviously different between genotypes. Asterisks, non-specific staining, due to anti-mouse secondary antibody, in blood vessels and sclera. Note that sclera became detached from control section prior to imaging.

B: Cross-sections through central retina of littermate control and *Ptf1a*^{cKO} mutant, stained for pan-RGC marker RBPMS (red) and Sox2 (green) to mark SACs. Blue, Hoechst nuclear counterstain (nuc). Optic nerve head (onh) marks center of retina. In *Ptf1a*^{cKO} mice, SACs are entirely absent from central retina, but Sox2+ astrocytes (*a*) in nerve fiber layer are present in normal numbers. RGC cell number appears to be increased, consistent with previous observations in embryonic retina of *Ptf1a* null mice (Fujitani et al., 2006; Nakhai et al., 2007).

Scale bars: 200 µm (A top); 100 µm (A bottom, B).

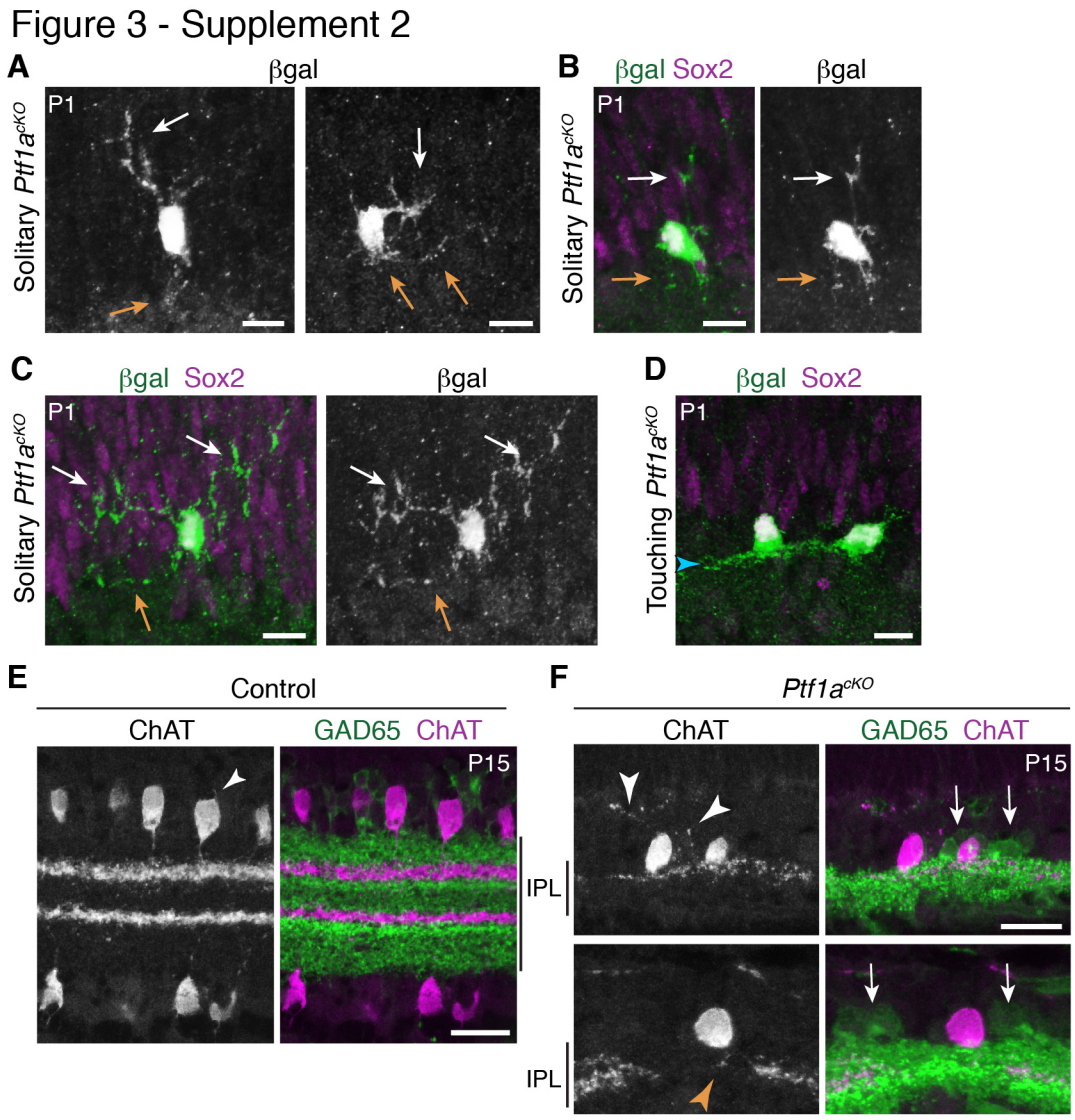

Figure 3-Supplement 1: SAC anatomy in *Ptf1a*^{cKO} mutants.

A-D: Additional representative examples of SACs in *Ptf1a*^{cKO} retinal cross-sections, from dataset used to compile graph in Fig. 3G. Neurons were validated as SACs by co-expression of *Megf10:*βgal and Sox2. Touching SACs (D) stratify their arbors normally (arrowhead). Note that the right-hand cell appears to be polarized towards the left-hand cell, suggesting asymmetric growth towards the side with homotypic contact and away from the side lacking it. Representative solitary SACs are shown in A-C. A depicts same cells as Fig. 3F (βgal channel only) in grayscale to highlight arbor morphology. Two cells (A, left; B) are examples of the class that failed to project to the IPL. The other cells (A, right; C) exemplify the class that sends only abnormal unbranched, unstratified arbors into the IPL. The cell in C also has particularly exuberant arbors in the INL that were much larger than those seen in any cells that touched their neighbors (e.g. D; also see Fig. 3D,E). White arrows, soma-layer arbors. Orange arrows, IPL arbors.

E,F: SAC errors in *Ptf1a*^{cKO} mutants persist to maturity. P15 littermate control (E) and mutant (F) retinal cross-sections stained for anti-ChAT to label SACs (red) and anti-GAD65 to label a broad non-SAC amacrine population (green). Control SACs no longer have soma layer arbors at this age; the only processes not directed toward the IPL were very short and minimal (E, arrowhead). In mutant retina, SACs from low-density regions often innervated the INL (F, white arrowheads), or failed to innervate gaps in the SAC IPL network (F, orange arrowhead). SACs that made errors likely interacted in the IPL with GAD65^{+} amacrine cell arbors (F, arrows) because these arbors completely filled the IPL in the region innervated by the SAC dendrites. This suggests that generic amacrine contacts are not sufficient to prevent SAC errors. Instead, because these SACs had few homotypic neighbors, the errors were likely due to paucity of SAC-SAC interactions.

Scale bars: 10 µm (A-D); 25 µm (E,F).

Figure 5 - Supplement 1

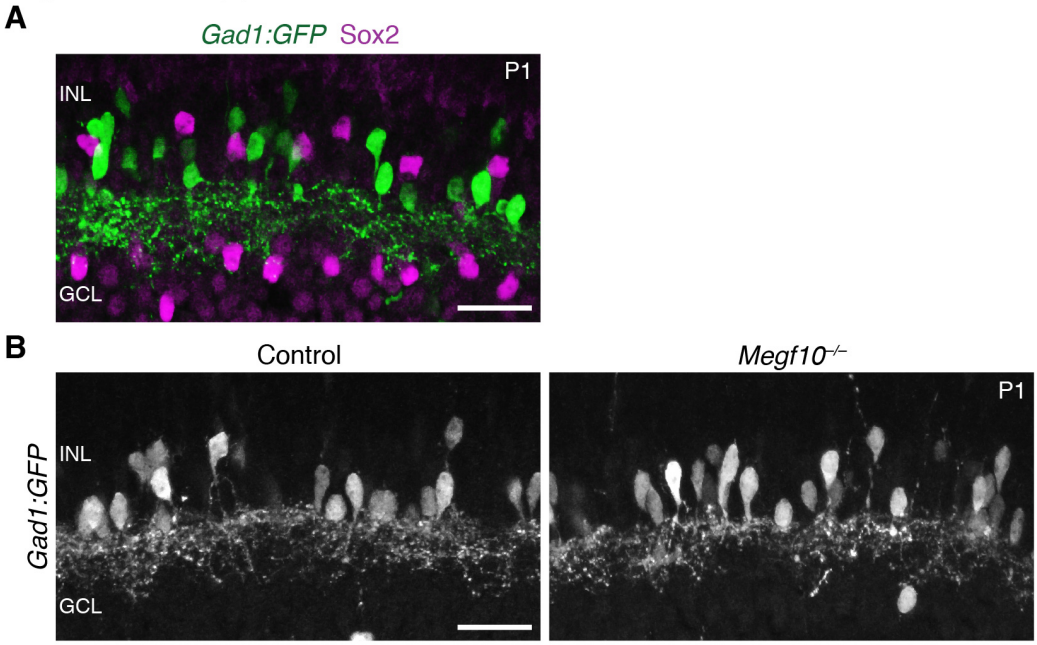

Figure 5-Supplement 1: *Gad1:GFP*$^+$ amacrine cells show normal dendrite projections in *Megf10* mutants.

A: Retinal cross-sections from P1 mice carrying *Gad1:GFP* transgene. GFP labels a large subset of amacrine cells in INL. Sox2$^+$ SACs do not express GFP. Therefore, the GFP$^+$ cells constitute a broad non-SAC amacrine population.

B; Retinal cross-sections from P1 *Megf10* mutants and littermate (*Megf10*$^{+/-}$) controls carrying *Gad1:GFP*. Unlike SACs (Fig. 5A), *Gad1:GFP*$^+$ amacrine cells innervated the INL normally in *Megf10* mutants, and did not make exuberant projections within the INL.

Scale bars: 25 µm

Figure 6 - Supplement 1

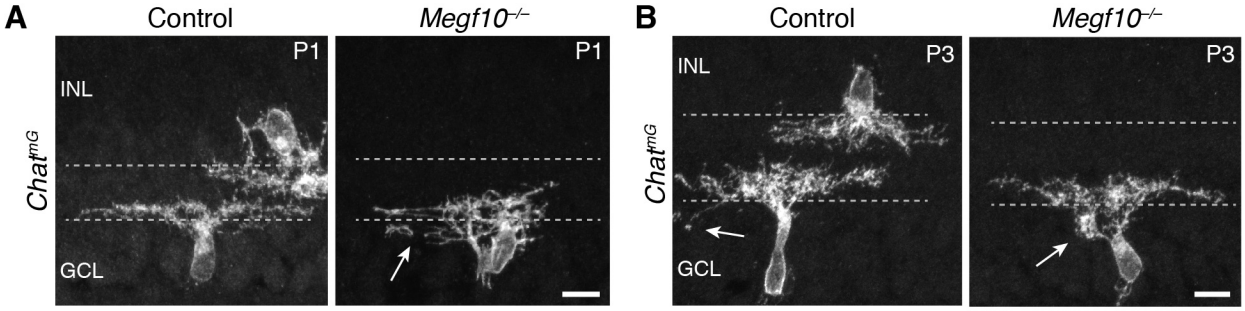

Figure 6-Supplement 1: ON SACs also make exuberant soma-layer projections in *Megf10* mutants.

A,B: Examples of P1 (B) and P3 (C) *Chat*^{mG}-labeled ON SACs that were part of the dataset used to generate graphs in Fig. 6E. At P1 (B) many mutant ON cells are bi-laminar, with projections in both IPL and GCL (arrow, GCL arbor). IPL projections were underdeveloped relative to controls, and not sufficient to generate a clear sublayer (Fig. 5A). C: P3 control and mutant ON SACs, both of which project to the GCL. The control cell sends a single arbor to the GCL (left, arrow), typical of those few SACs that still project to the soma layers at this age. The mutant cell (right) makes a dense dendritic arborization in the GCL (right, arrow), which was never seen in P3 controls.

Scale bars: 10 µm.

Figure 7 - Supplement 1

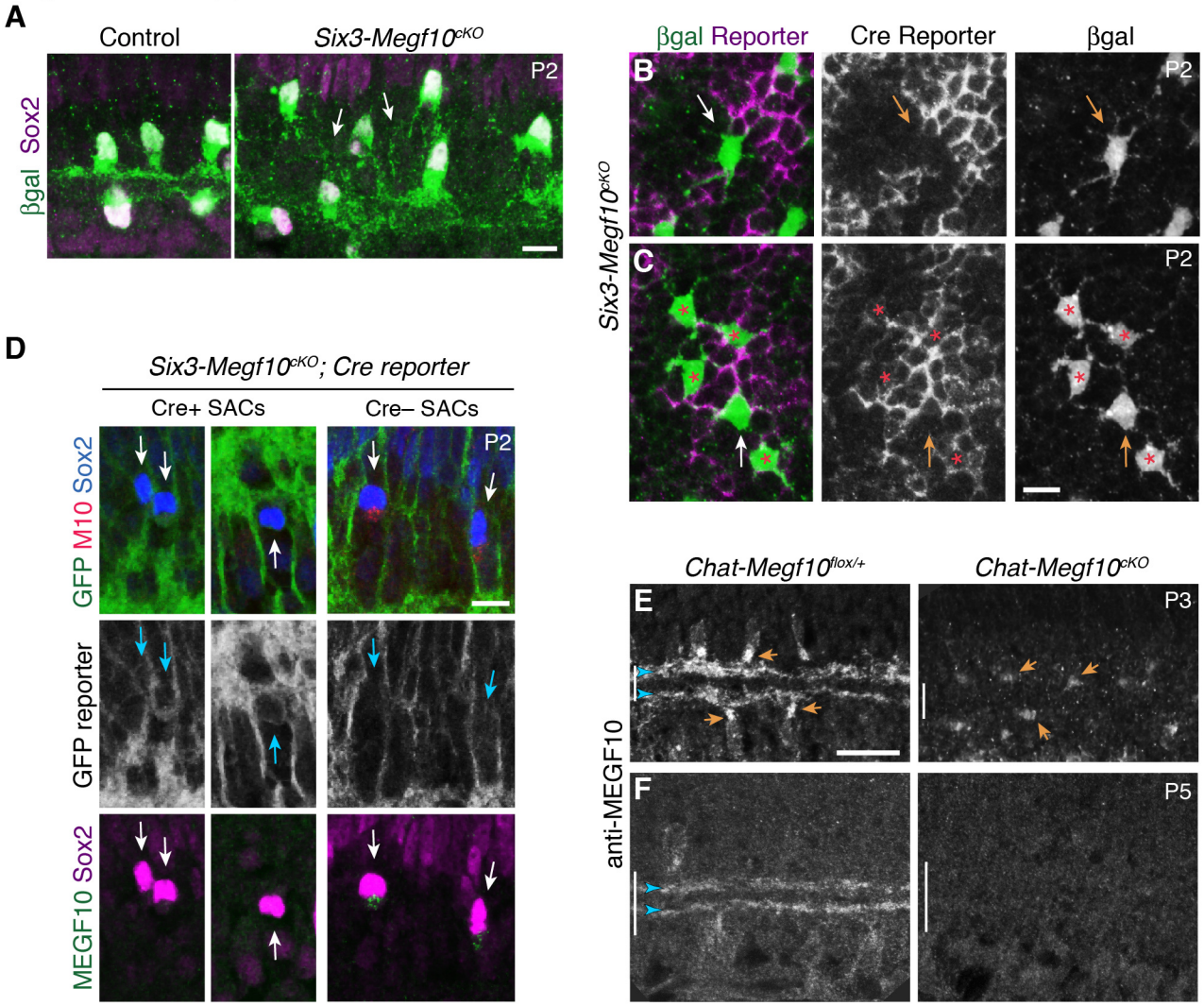

Figure 7-Supplement 1: *Megf10* cell autonomy: Characterization of conditional mutant mice

A: *Six3-Megf10*^{cKO} mice phenocopy SAC sublayer formation errors seen in null mutants. Cross-sections through central retina of P2 *Six3-Megf10*^{cKO} and littermate control mice. Immunostaining for *Megf10*: βgal and Sox2 revealed SAC morphology. Control SACs (left) have formed IPL sublayers by P2 and they rarely project to soma layers. In *Six3-Megf10*^{cKO} mice (right), sublayers are absent and SACs project exuberantly to soma layers (arrows).

B: The same *Six3-Megf10*^{cKO} Cre-negative SAC from Fig. 6B (arrow). βgal and GFP (Cre reporter) channels are shown separately (middle, bottom) to demonstrate lack of GFP expression in this cell.

C: Another example of a Cre reporter-negative *Six3-Megf10*^{cKO} SAC (arrow) surrounded by mutant Cre-positive cells (asterisks). All 5 cells, including the unrecombined one, participate in an aberrant INL dendritic network (bottom).

D: GFP Cre reporter is a reliable proxy for MEGF10 protein expression status in *Six3-Megf10*^{cKO} mice. Cre^{+} SACs (left, center panels) express the GFP reporter and lack MEGF10 immunoreactivity. Cre^{-} SACs lack GFP reporter expression and retain MEGF10 immunoreactivity. Arrows denote position of Sox2^{+} SACs in each panel.

E,F: Timing of MEGF10 protein loss in *Chat-Megf10*^{cKO} mice. At P3 (E), MEGF10 immunoreactivity is much lower in mutants (right) than in littermate controls (left), but most SACs still express some protein (arrows

indicate examples of MEGF10-positive cells). At P5 (F), MEGF10 immunoreactivity is virtually absent in mutants but readily detectable in controls. Arrowheads, SAC IPL strata. Vertical bar, IPL.

Scale bars: 10 µm (A-D); 25 µm (E,F). Scale bar in C applies to B, and bar in E applies to F.

Figure 7 - Supplement 2

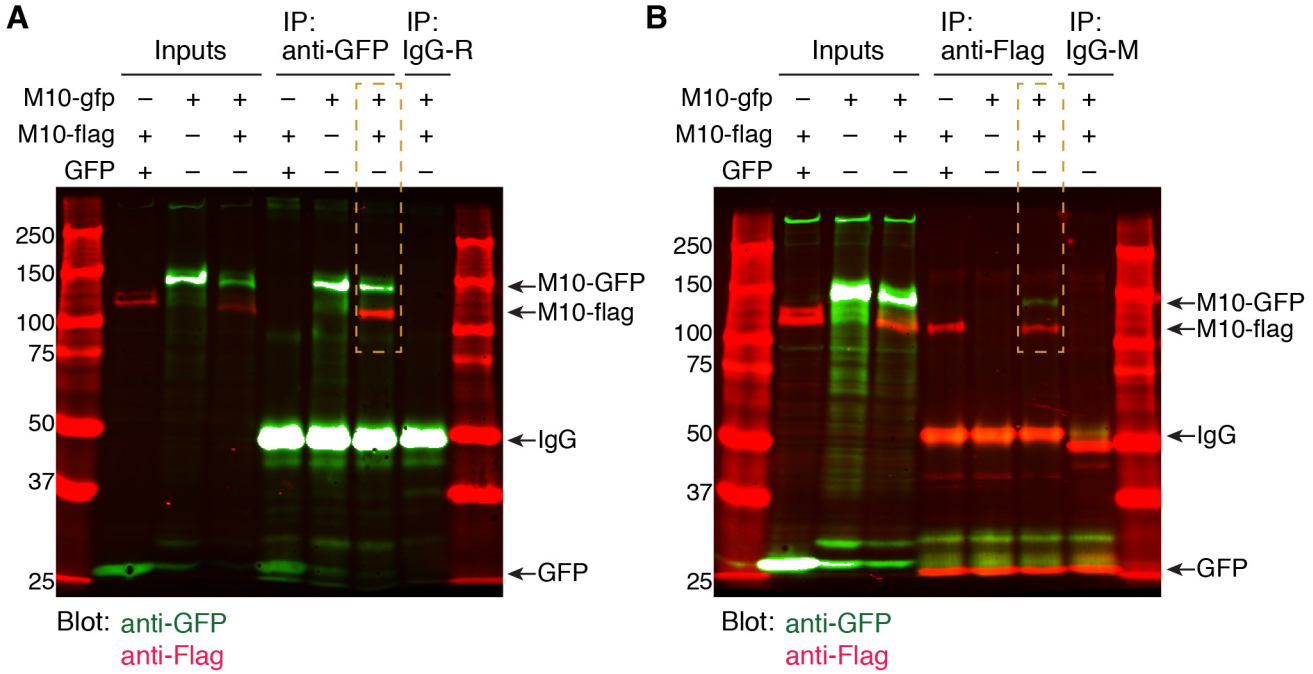

Figure 7-Supplement 2: MEGF10 co-immunoprecipitation experiments

A: Uncropped blot image for co-IP experiment depicted in Fig. 6J. Anti-GFP was used for pull-down. Blot was stained for anti-GFP (green) and anti-Flag (red). Orange box indicates the condition in which cells were transfected with both MEGF10-ΔICD constructs. In this condition, pull-down with anti-GFP precipitated both MEGF10-ΔICD-GFP and MEGF10-ΔICD-Flag constructs, demonstrating that they interact. Ladder markings in kDa. Expected sizes for MEGF10-ΔICD constructs, GFP, and IgG are indicated (arrows). R, rabbit IgG control. See Fig. 6I for illustration of in MEGF10-ΔICD construct design.

B: Independent replicate of MEGF10-ΔICD co-IP experiment, using anti-Flag for pull-down. Labels as in F. IP with anti-Flag co-precipitated both GFP and Flag-tagged MEGF10-ΔICD constructs (orange box). Mouse (M) IgG control did not precipitate MEGF10 constructs, and MEGF10-ΔICD-Flag did not co-precipitate with GFP alone.

Figure 8- Supplement 1

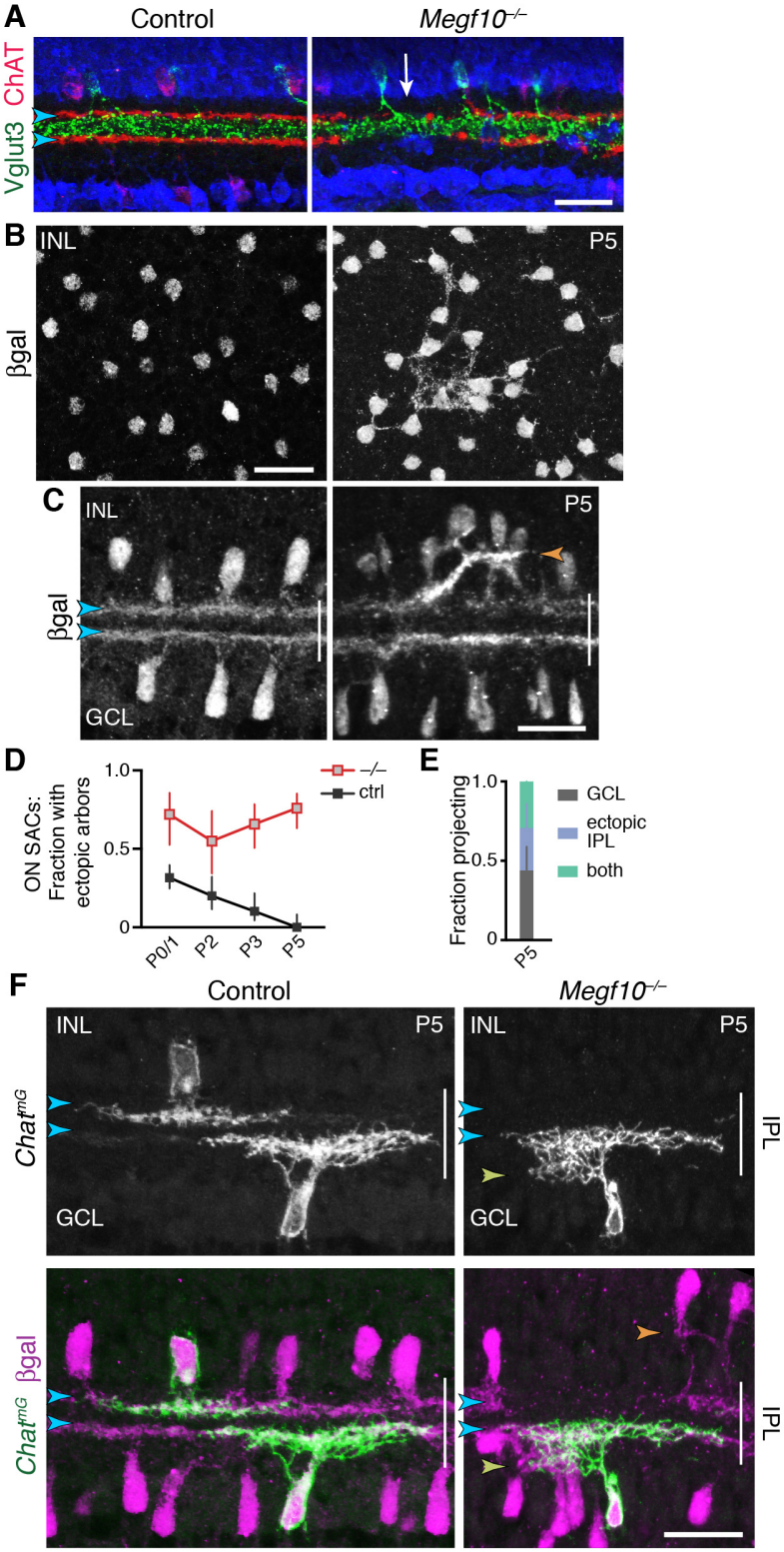

Figure 8-Supplement 1: SAC phenotypes in *Megf10* mutants at P5 and at maturity.

A: Specificity of *Megf10*$^{-/-}$ SAC IPL innervation phenotype. The same cross-sections from Fig. 8A are shown here, overlaid with anti-Vglut3 staining (green) to label amacrine cells that project to an IPL sublayer between the SAC strata (arrowheads). Regions of mutant IPL not innervated by SACs (arrow) are still innervated by Vglut3^{+} amacrine cells, demonstrating that absence of ChAT^{+} arbors is not due to histology artifact and that impaired IPL innervation is a SAC-specific phenotype.

B,C: Anatomy of mutant SAC ectopic network at P5 provides further evidence that it shifts from INL to IPL. *Megf10:*βgal staining seen *en face* at level of INL (B), and in cross-section (C). Mutant SAC arbors are aggregated and fascicular by P5; this contrasts with P3 when exuberant INL arbors are more diffuse (Fig. 6). Unlike later stages (Fig. 8A), when fascicles are only found in IPL, P5 fascicles could be located in the INL (B). Some arbor fascicles crossed the INL-IPL boundary at P5 (C, orange arrowhead). This was not seen at earlier or later ages (Fig. 6A; Fig. 8A), suggesting P5 is a transitional age in the INL-to-IPL shift.

D,E: ON SAC ectopic projections transition to the IPL at P5 in *Megf10* mutants, similar to OFF SAC projections (Fig. 8F,G). Frequency of mutant ectopic ON SAC projections does not decline over development (D), even though arbor anatomy changes by P5 (E). P0-3 data in D replotted from Fig. 6E, with both control groups combined. E: As with mutant OFF SACs, ON SACs can make ectopic projection errors either within the GCL or the IPL at P5.

F: *Megf10* mutant ON SAC phenotype at P5, revealed using *Chat*^{mG} to label single cells and *Megf10:*βgal to label the full SAC population. Control SACs (left panels) are monostratified within the DS circuit IPL sublayers (blue arrowheads). Right: Example of a mutant ON SAC that makes an ectopic projection to inappropriate IPL sublayer (yellow arrowhead) while also projecting to the expected DS circuit sublayer (blue arrowheads). OFF SACs in this same field of view make ectopic projections within the INL (orange arrowhead), illustrating the simultaneous soma-layer and IPL ectopias observed only at P5.

Scale bars: 25 µm.

Figure 9 - Supplement 1

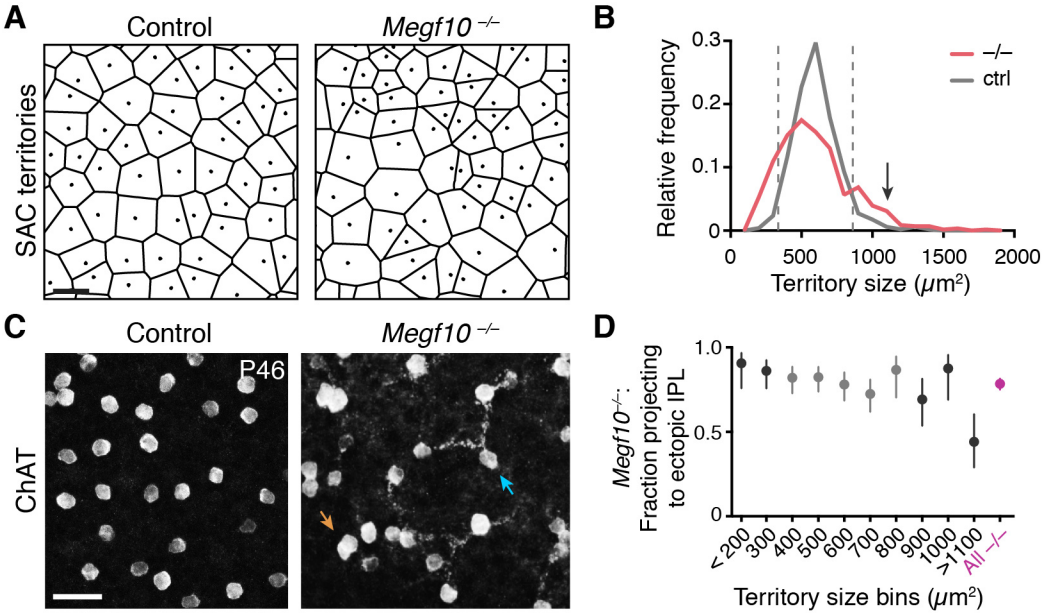

Figure 9-Supplement 1: Severity of *Megf10*$^{-/-}$ SAC mosaic phenotype does not correlate with IPL targeting error rate.

A,B: Strategy for quantifying severity of mosaic phenotype on single-cell level. The Voronoi domain (A; see Methods) is determined by the position of a cell relative to all its neighbors and therefore serves as a useful single-cell measure of local cell positioning (see Methods). In control retina, the position of SACs relative to their neighbors is constrained by local cell-cell repulsion. This can be seen in the uniform size distribution of their Voronoi territories: A, representative Voronoi domain images (dots, cell body positions); B, histogram of SAC territory (i.e. Voronoi domain) sizes. Control distribution (gray line) has a sharp peak.

In *Megf10* mutants, the arrangement of SAC cell bodies is random; as a result, there are many mutant cells that, by chance, are positioned quite normally relative to their neighbors, while other SACs are abnormally near or far. This population-level phenotype manifests as a broader distribution of SAC territory sizes (B, red line). For individual mutant SACs, their position along this size distribution curve can be used as a measure of mosaic phenotype severity. Dashed lines (B), upper and lower 95% tolerance intervals of the control distribution. Mutant cells outside these lines experience crowding or isolation rarely seen in control retina. Arrow in B denotes largest bin in D. Bin size = 100 μm^2. Sample sizes: n = 515 cells from 2 littermate control (*Megf10*$^{+/-}$) mice; n = 584 cells from 2 *Megf10*$^{-/-}$ mice.

C: No obvious correlation between a mutant cell's local neighborhood density and its projection to ectopic IPL network. *En-face* view of SAC cell bodies and outer IPL, generated by Z-projecting part of a confocal stack corresponding to these layers (Z distances: left, 4.4 μm, right 4.0 μm). Controls lack SAC dendrites at this IPL level. Arrows, examples of cells that are unusually far from their neighbors yet join the ectopic network (blue arrow), or that are unusually crowded yet do not join (orange arrow).

D: Frequency of ectopic IPL projections for mutant SACs in each 100 μm bin of histogram in D. Dark shading, bins outside dashed lines in D. Smallest and largest bins were pooled to ensure adequate sample size ($n \geq 24$ SACs per bin; see Methods for bin sizes). Across all bins except the largest one (denoted in B by arrow), error rate was similar to the overall mutant error rate (red). Even in this last bin, SACs still made errors about 50% of the time. These results demonstrate that ectopic IPL lamination errors are largely independent of soma positioning errors. X values denote bin center (aside from pooled bins <200 μm^2 and >1100 μm^2). Error bars, 95% confidence intervals.

Scale bars, 25μm.

Figure 10 - Supplement 1

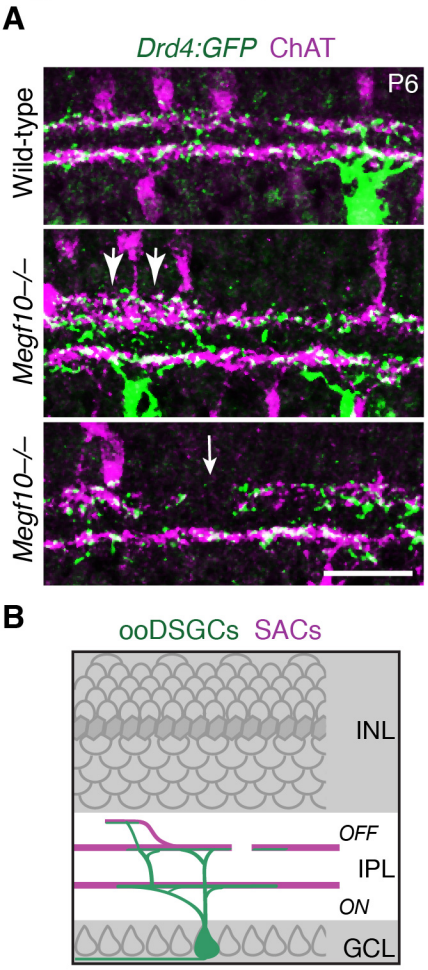

Figure 10-Supplement 1: IPL innervation by ooDSGCs in *Megf10* mutants.

A: *Drd4:GFP* mouse line was used to label a subset of ooDSGCs that is mutually exclusive with *Hb9:GFP*. IPL laminar targeting by *Drd4:GFP*$^{+}$ ooDSGCs was assessed in cross-sections of *Megf10*$^{-/-}$ and littermate control retinas, co-stained for ChAT to reveal SAC dendrites. In mutants, *Drd4:GFP*$^{+}$ cells made the same laminar targeting errors observed in the *Hb9:GFP* line (Fig. 10): When SACs projected to inappropriate laminar locations, ooDSGC dendrites were recruited to join them (center panel, large arrows). GFP^{+} dendrites also failed to enter IPL regions not innervated by SACs (bottom panel, white arrow).

B: Summary of ooDSGC laminar targeting errors in *Megf10* mutants. Dendrites of ooDSGCs go to ectopic IPL locations when SACs do so, and fail to enter SAC IPL gaps.

Scale bar: 25 µm

Figure 11 - Supplement 1

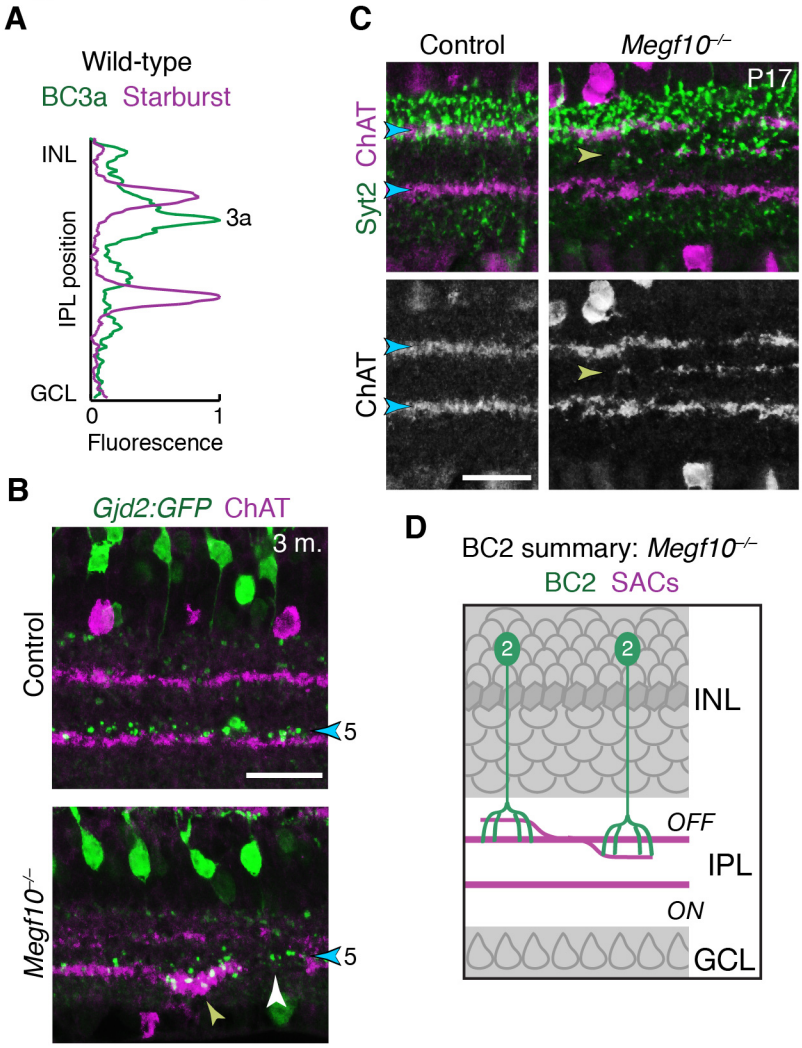

Figure 11-Supplement 1: IPL innervation by DS circuit bipolar cells in *Megf10* mutants.

A: Fluorescence intensity plot across IPL obtained from a wild-type image similar to Fig. 11B – i.e. tissue stained with anti-ChAT (purple) and the BC3a marker HCN4 (green). BC3a arbors are excluded from the OFF SAC sublayer and arborize adjacent to it, similar to the behavior of BC5 and BC7 (Fig. 11D).

B: *Gjd2:GFP* mouse line was used as an independent marker of BC5 bipolar cells. In cross-sections of adult retinas stained for anti-GFP (green) and anti-ChAT (red), GFP was found to label BC5 neurons arborizing in their characteristic position adjacent to the ON SAC sublayer (blue arrowhead). Thus, unlike the *Kcng4*^{mG} line in which both BC5 and BC7 were labeled, this line could be used to specifically assess BC5 phenotypes. In *Megf10* mutants, an ectopic SAC projection near the GCL border (yellow arrowhead) recruited BC5 terminals to an inappropriate IPL location. BC5 terminals are also seen innervating a gap in the SAC sublayer (white arrowhead). These phenotypes are similar to observations in *Kcng4*^{mG} mice (Fig 11C-E).

C,D: Laminar targeting errors by BC2 bipolar cells in *Megf10* mutants. In control retina, BC2 axon terminals (stained with anti-Syt2, green) fill the entire IPL region between the INL border and the OFF SAC layer. This is the same region in which OFF SAC misprojection errors typically were found in mutants (e.g. Fig. 9A); therefore, most mutant errors did not probe whether BC2 axons could be recruited to new IPL regions. However, we did find a small number of cases, such as the one shown here, in which OFF SACs project inappropriately to central IPL regions where BC2 terminals are not normally found (yellow arrowhead). In these cases BC2 arbors are recruited to join SAC arbors in their abnormal laminar location. Thus, BC2 IPL projections are likely guided by similar SAC-derived cues as the other DS circuit-projecting bipolar cell types. D, summary of the BC2 projection phenotype in *Megf10* mutants, showing SAC errors that occurred within the normal BC2 domain (left) as well as those that recruited BC2 arbors to new laminar positions.

Scale bars: 25 µm.

Figure 12-Supplement 1

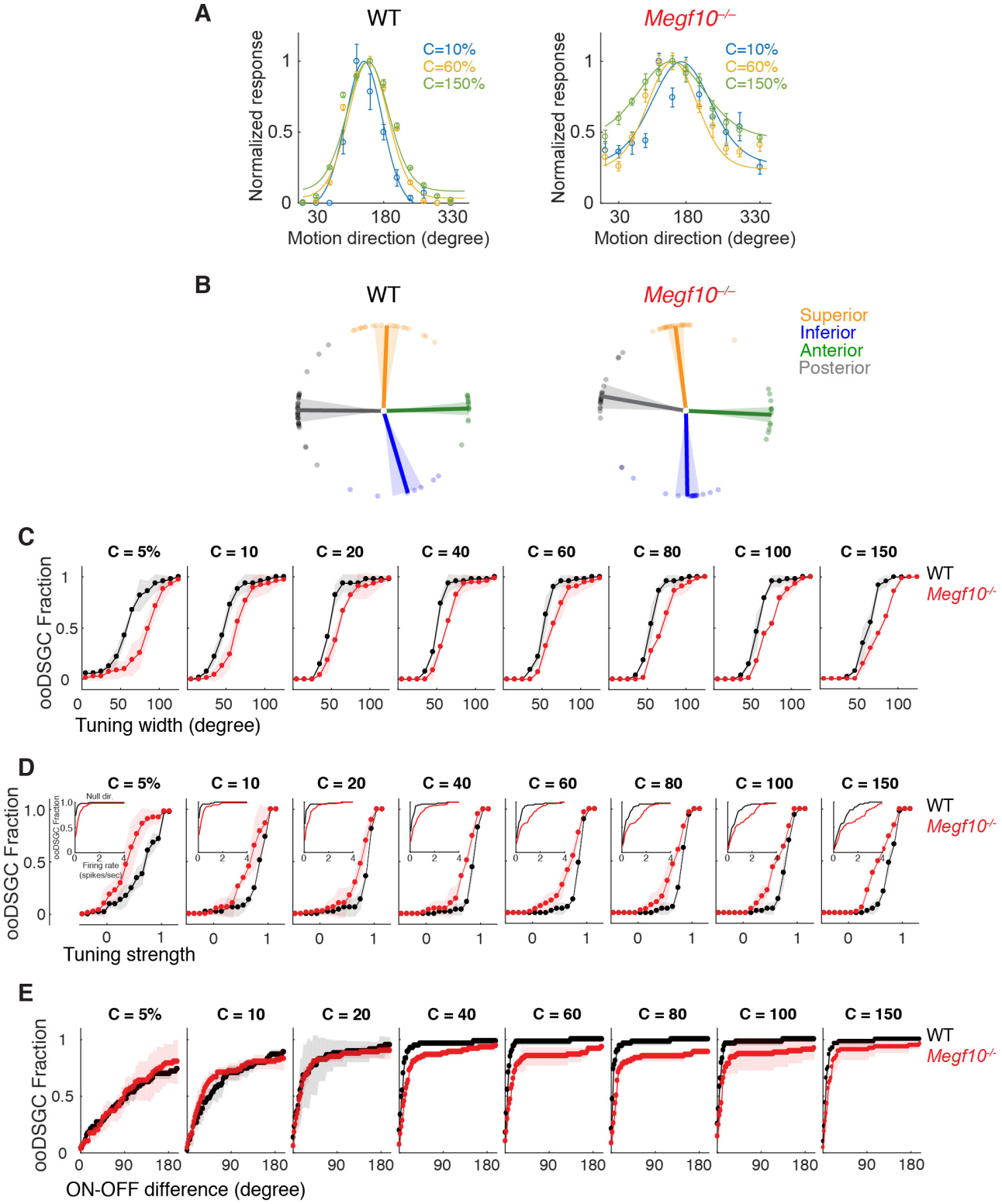

Figure 12-Supplement 1: Contrast-dependence of direction-tuning phenotypes in *Megf10*$^{-/-}$ ooDSGCs.

A: Tuning curves from representative wild-type (WT) and *Megf10* mutant ooDSGCs measured at 3 contrasts (10, 60 & 150% Weber contrast). Circles show responses, solid lines show von Mises fits. Mutant tuning curves are broader than controls at all three contrasts.

B: Preferred directions of WT ooDSGCs (left) align to the four cardinal ocular axes: superior, inferior, anterior and posterior (Oyster and Barlow, 1967). K-means clustering was used to separate the recorded ooDSGC

population into these four subtypes (see Methods). Population mean (solid line) and standard deviation (shaded region) of preferred directions for each subtype is plotted; circles denote preferred direction of individual ooDSGCs. Preferred directions of *Megf10*$^{-/-}$ ooDSGCs (right) were also aligned to the cardinal axes, and there was no appreciable change in the fraction of ooDSGCs populating each subtype.

C-E: Cumulative distributions of tuning width (quantified by circular standard deviation; C), tuning strength (D), and ON-OFF preferred direction difference (E), measured at different bar contrasts (identified at the top of each plot) for WT and *Megf10*$^{-/-}$ ooDSGC populations. Insets (D) show responses to null direction stimuli. The analyzed RGC populations were the same as for data shown in Fig. 10 (n = 80 WT and 74 mutant ooDSGCs, two retinas each genotype). The width and speed of the moving bar was 1200 µm and 550 µm/sec, respectively. Error bars/bands, S.E.M.